Phonon thermal transport and its tunability in GaN for near-junction thermal management of electronics: A review

Dao-Sheng Tang [a,b], Bing-Yang Cao [b,*]

[a] *School of Rail Transportation, Soochow University, Suzhou, Jiangsu, PR China*
[b] *Key Laboratory for Thermal Science and Power Engineering of Ministry of Education, Department of Engineering Mechanics, Tsinghua University, Beijing, PR China*

ARTICLE INFO

ABSTRACT

The heat dissipation issue has now become one of the most important bottlenecks for power electronics due to the rapid increase in power density and working frequency. Towards the wide bandgap semiconductor GaN high electron mobility transistors (HEMTs), near-junction thermal management is the breakthrough that mainly includes the accurate thermal modeling and effective thermal design for GaN and GaN HEMTs. In this review, we first offer a comprehensive understanding of phonon thermal transport in GaN and GaN HEMTs, including non-equilibrium transport of electrons and phonons in the heat generation process, phonon thermal conductivity, heat spreading, and interfacial thermal transport. Then, we review the current tuning mechanisms and methods for thermal transport in GaN and GaN HEMTs which are classified into three categories according to the particle nature, wave nature, and topological nature of phonons. At last, we conclude by providing our perspectives on challenges and opportunities in the research of phonon thermal transport and its tuning mechanisms in GaN HEMTs.

© 2022 Elsevier Ltd. All rights reserved.

1. Introduction

Power electronics are one of the most important kinds of electronics, mainly used for signal control, energy conversion, and energy transformation, in rail transportation, new energy vehicles, radio frequency systems (radar, communications, and electronic warfare), *etc.* [1]. Driven by the increased demands on electrical performance, power electronics are developed for higher power density and working frequency, which requires better electric properties for semiconductors and electronics [2–4]. One approach is to tap the potential of silicon as much as possible with advanced electrical design [5,6]. To now, with the structure of the insulator gated bipolar transistor (IGBT) [5], which combines the advantages of the metal-oxide-semiconductor field-effect transistor and bipolar junction transistor, silicon semiconductor has nearly reached its limitation in electric performance. The other approach is to discover and develop new semiconductor materials with better electric properties. Currently, wide bandgap semiconductors [4,7-12], including silicon carbide (SiC) and gallium nitride (GaN), have received much attention due to their excellent electric properties such as electron mobility, saturated electron density, and breakdown electric fields (Fig. 1). Since silicon has nearly reached its limit due to its intrin-

sic material properties, present and future high-power electronics are mainly developed based on GaN and SiC, as well as developing ultra-wide bandgap semiconductors [13].

Accompanied by the increase of power density, working frequency, and integrity in power electronics, heat flux density in electronics increases rapidly, leading to the heat dissipation issue becoming the bottleneck in the development of GaN-based electronics[15,16]. Under high bias voltage conditions, high power loss increases the temperature in chips due to the limited heat dissipation capacity, which depends on the thermal conductivities of the channel layer and substrate materials, as well as the interfacial thermal conductance. With the increase of the local temperature, electron-phonon scatterings are enhanced, reducing the carriers' mobility in the quantum well, *i.e.*, the interface region in AlGaN/GaN heterostructure, which further results in the attenuation of the static *I-V* characteristic of the electronics. This phenomenon in electronics is called the self-heating effect [17–20]. Besides, local high temperatures in devices will bring in uncontrollable stress fields and result in the reduction of device lifetime. As reported by the recent investigations, it is still difficult to fully realize the electric potential of GaN in experiments limited by the heat dissipation issue [1,21].

In the past several decades, thermal management for electronics has received more and more attention and has been developed with the progress in electronics. Various methods and tech-
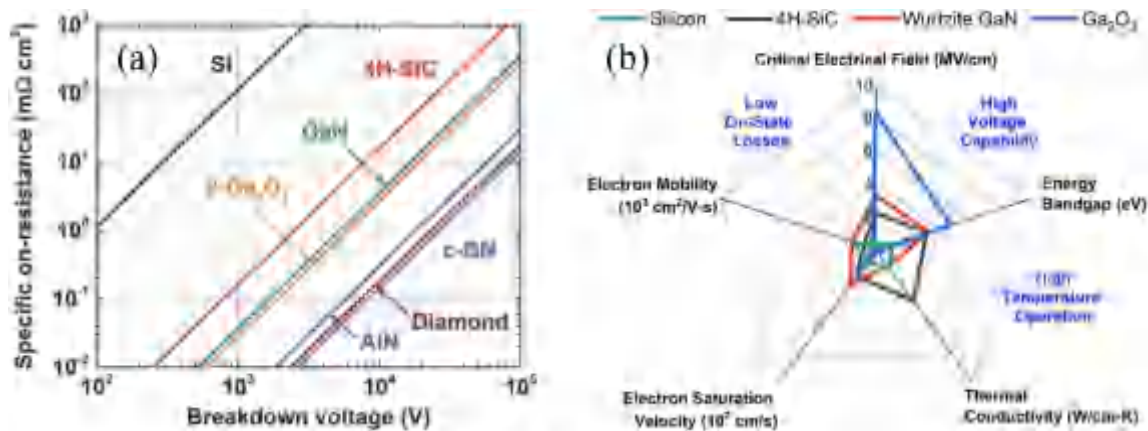
Fig. 1. Comparisons among representative semiconductors including silicon and GaN, *etc.* (a) Baliga figure of merit (BFOM) for typical semiconductors defined as the ratio of the square of breakdown voltage and specific on-resistance V_{BR}^2/R_{ON-SP}, the lower right region represents higher BFOM, hence higher performance, from ref. [4] (b) Critical material properties for four typical semiconductors, from [ref. 14].

niques are proposed for external thermal management, including heat pipes, air cooling, phase change materials cooling, thermoelectric cooling, *etc.* [15,22-31]. For external thermal management, heat convection is the dominant heat transfer mode, where the structure and processes optimization design are the main topics. To connect the external part and the internal part of electronics, thermal interface materials (TIMs) are important, which are generally sticky and insulating with relatively low thermal conductivity. To improve the thermal transport across TIMs, low-dimensional materials with high thermal conductivity such as graphene, nanotube, and metal nanoparticles are mixed into matrix materials [32]. As the external thermal management technology matures, thermal resistance distribution changes. Present thermal modeling on GaN high electron mobility transistors (HEMTs) shows that the internal thermal resistance, *i.e.*, the thermal resistance from TIMs and near-junction thermal resistance, is dominated, where the near-junction region is illustrated in Fig. 2(a) and (b). Consequently, thermal management, especially near-junction thermal management, for power and information electronics has become one of the most important parts of thermal management towards high technology, besides those for power batteries, LED, data centers, *etc.* In other words, the issue that the heat flux generated from hot spots cannot be effectively dissipated from the near-junction region mainly results from the high near-junction thermal resistance while improving external heat dissipation contributes little now. For near-junction thermal management investigations in kinds of electronics, the basic steps are similar, which include accurate thermal modeling and predictions, effective thermal design, and efficient heat dissipation. The detailed investigations are different since they are structure- and process-dependent. Here, it is concentrated on the heat conduction part, *i.e.*, phonon transport, in the near-junction thermal management for GaN-based electronics.

2. Phonon thermal transport in GaN and GaN HEMTs

2.1. Thermal transport picture and characteristics in GaN HEMTs

The typical power electronic device of GaN is the heterostructure field-effect transistor (HFET) and named the high electron mobility transistor (HEMT) due to its extraordinary characteristic, *i.e.*, high electron mobility. The core structure of GaN HEMT is the AlGaN/GaN heterostructure, *i.e.*, the near-junction region of GaN HEMT, which is shown in Fig. 2(b) with detailed interface structures in Fig. 2(c) and (d). In specific, the device is grown from the bottom up. Following the growth order (from the bottom layer to the top layer), the structure consists of the substrate layer, the GaN

channel layer, and the AlGaN barrier layer. The 2-dimensional electron gasses (2DEG) are formed in the AlGaN/GaN heterostructure to realize specific electric functions. As illustrated in Fig. 2(c) and (d), there are two critical interfaces in GaN HEMT, which are the AlGaN/GaN interface and the GaN/substrate interface. The interface structure consists of several thin layers besides the main layers. At AlGaN/GaN interface, additional GaN or AlN thin layers will be inserted for electric functions or purposes. At GaN/substrate interface, to decrease the lattice mismatch between GaN and foreign substrates, transition layers such as the AlN layer will be grown on the substrates. Here, it should be emphasized that these additional inserted layers can be neglected for thermal transport in some cases, while they may play important roles in some other cases, depending on the characteristics of the thermal transport processes.

2.1.1. Non-equilibrium thermal transport

In electronics, especially in the near-junction region, heat energy is generated in a nanoscale region and then transports in a multiscale region (nanoscale to macroscale) with interfaces. For these processes, non-equilibrium is a significant characteristic. On one hand, non-equilibrium exists in time scale among different carriers, including electrons, optical phonons, and acoustic phonons. In detail, the phonon emission from electrons is the source of heat dissipation where high-frequency phonons play the intermediate role as electron-phonon interaction mainly occurs for high-frequency phonons (high-frequency polar optical phonons in GaN), while low-frequency phonons including low-frequency optical phonons and acoustic phonons are responsible for the lattice thermal transport, as illustrated in Fig. 3. Therefore, besides the non-equilibrium between electrons and optical phonons, the non-equilibrium also exists in phonons, *i.e.* high-frequency optical phonons and low-frequency acoustic phonons. Actually, GaN hosts very strong electron-phonon coupling (EPC), especially the electron-polar optical phonons (known as the Fröhlich EPC) [33,34]. In hybrid heat generation and conduction process, EPC mainly affect the heat dissipation and induce the non-equilibium in both electron and phonon systems due to the different EPC for different phonon modes. The effects of EPC on lattice thermal conductivity will be discussed in Section 2.2. On the other hand, non-equilibrium occurs on a spatial scale due to the nanoscale constriction in near-junction regions. The characteristic sizes of the heat source and channel layer are around nanometers and micrometers, respectively, which are smaller than or comparable with the phonon mean free path (MFP) of GaN, implying the non-Fourier heat conduction, *i.e.*, phonon ballistic-diffusive trans-
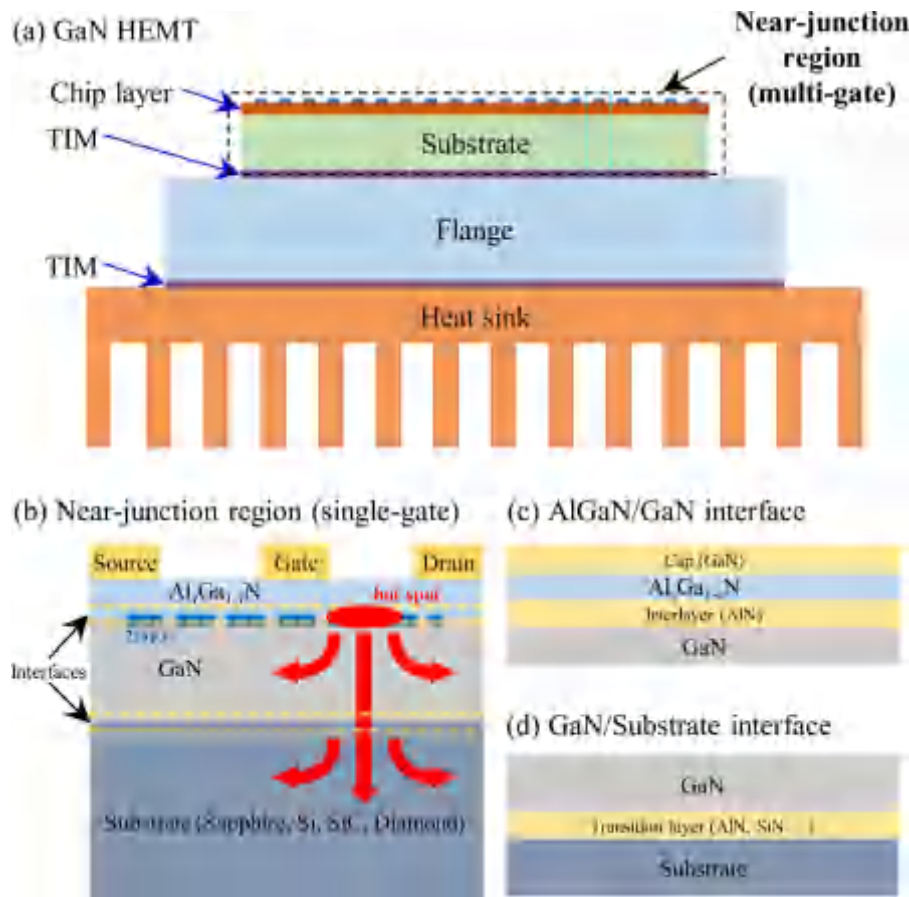
Fig. 2. Schematic of the GaN HEMT device and the near-junction region. (a) The overall structure of GaN HEMT (b) Near-junction region of GaN HEMT (single-gate) (c) Detailed structure of AlGaN/GaN interface and (d) GaN/substrate interface. The blue dot line represents the 2-dimensional electron gas (2DEG), the red circle represents the heat source, and the red arrows indicate the heat flux. (For interpretation of the references to colour in this figure legend, the reader is referred to the web version of this article.)
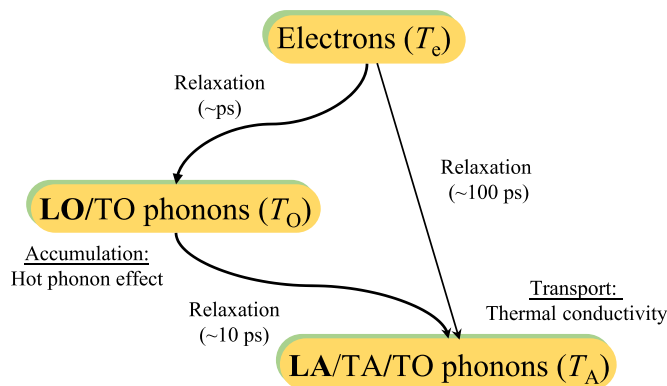
Fig. 3. Energy transfer from electrons to phonons in heterostructures. Energy is transferred from electrons to phonons by the electron-phonon interaction known as the Joule heat. Optical phonons receiving the most heat are then relaxed into the acoustic phonons, which contribute the most to lattice thermal transport. Three different temperatures are present during these processes, named as T_e for electrons, T_O for optical phonons, and T_A for acoustic phonons. (For interpretation of the references to colour in this figure legend, the reader is referred to the web version of this article.)

port. The non-equilibrium transport will mainly result in the deviation of actual thermal conductivity to the bulk thermal conductivity. For the two non-equilibrium processes, the former is relevant to the attendance of high-frequency optical phonons with low group velocity, and the latter is relevant to the size effect of heat

source and heat transport which decreases the effective thermal conductivity.

2.1.2. Thermal spreading

Thermal spreading is another characteristic of near-junction heat conduction, as illustrated by the heat flux in Fig. 2(b). In general thermal analyses, thermal resistance is a simple and intuitive physical quantity, suitable for evaluating the thermal performance of electronics, especially in practical applications. The initial and strict concept of thermal resistance is defined in one-dimensional heat conduction conditions. However, heat conduction in the near-junction region is more than simply one-dimensional, but is three-dimensional, where heat transports from a spot to a planar substrate. Since it is now clear that the thermal resistance is process-dependent, understanding this issue is quite essential. Illustrated by the simulation work, thermal spreading introduces many interesting results. Guo et al. [35] and Song et al. [36] both reported the non-monotonic change of the near-junction thermal resistance concerning the thickness of the GaN channel layer (Fig. 4). In Guo's work [35], this phenomenon occurs in the cases with a higher interfacial thermal resistance and is explained as that the ratios of heat transfer in different directions are affected by interfacial thermal resistance. In the two-dimensional thermal simulations by Song [36], this phenomenon is also explained as the similar reasons that a thinner GaN layer decreases the volume for heat transfer and then suppresses the heat spreading, where the size effect of thermal conductivity is also considered. Essentially, it is because the dominated thermal resistant regime of the heat conduc-
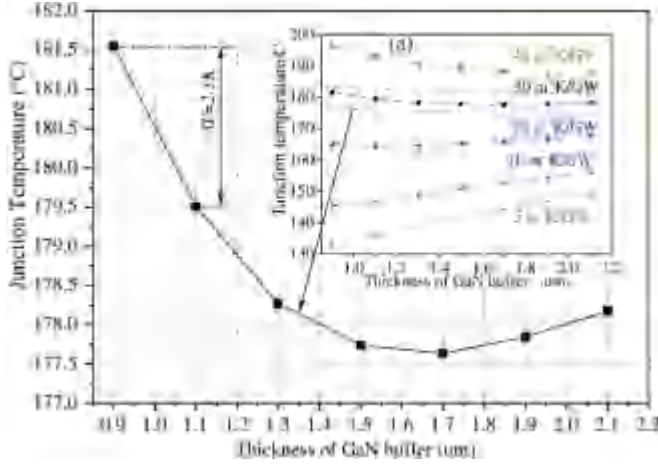
Fig. 4. Non-monotonic junction temperature changes concerning the thickness of the GaN layer, from [ref. 35].

Fig. 5. (a) Schematic of heat spreading in GaN layer, where the sizes of heat source and GaN layer are labeled (b) Dimensionless temperature distributions of GaN along the heat source plane calculated in different ways including finite element method (FEM) with GaN bulk thermal conductivity, FEM with effective thermal conductivity (proposed thermal conductivity model considering the ballistic effect), and phonon Monte Carlo simulations considering phonon dispersions of GaN. θ is a nondimensional temperature. From [Ref. 37].

tion process changes with the change of the GaN layer thickness. The spreading resistance is the major reason when the thickness is small while the intrinsic resistance ($R = t/Sk_0$, where t is the thickness, S is the area, and k_0 is the thermal conductivity) becomes dominant when the thickness increases.

In the near-junction region, the heat spreading and ballistic-diffusive phonon transport are present simultaneously. By considering the ballistic effects, Hua et al. [16] and Shen et al. [37] further investigated the thermal spreading in the ballistic-diffusive regime, and show the additional increase of thermal spreading resistance from the ballistic effects. With Monte Carlo (MC) simulations and theoretical analyses, Hua et al. [16] reported that the total thermal resistance consists of four parts including the intrinsic thermal resistance, spreading resistance, the thermal resistance from the cross-plane ballistic transport, and the thermal resistance from the size effect of the heat source. In specific, the non-dimensional total thermal resistance is defined as the ratio between the total thermal resistance R_t and intrinsic resistance (represented as R_{1d_0} here) of the GaN layer,

$$\frac{R_t}{R_{1d\_0}} = \frac{R_F}{R_{1d\_0}} \frac{R_{1d}}{R_{1d\_0}} \left[\frac{R_t}{R_{1d}} \left(\frac{R_F}{R_{1d\_0}} \right)^{-1} \right], \tag{1}$$

where

$$\frac{R_F}{R_{1d\_0}} = 1 + \left(\frac{w}{w_g} \right)^2 \left(\frac{w}{t} \right) \sum_1^\infty \frac{8\sin^2\left(\frac{w_g n\pi}{2w} \right)\cos^2\left(\frac{w_g n\pi}{2w} \right)}{(n\pi)^3 \coth\left(\frac{tn\pi}{2w} \right)}, \tag{2}$$

$$\frac{R_{1d}}{R_{1d\_0}} = 1 + \frac{2}{3}Kn_t, \tag{3}$$

$$\frac{R_t}{R_{1d}} \left(\frac{R_F}{R_{1d\_0}} \right)^{-1} = 1 + A_w(w_g/w, w/t)Kn_w, \tag{4}$$

The variables w, w_g, and t indicate the size of the GaN layer, as shown in Fig. 5(a), and two dimensionless parameters Kn_t and Kn_w are Knudsen numbers specifically for the layer thickness and heat source width defined as $Kn_t=l/t$ and $Kn_w=l/w_g$ (l is the phonon MFP). A_w is a fitting parameter extracted from MC simulations. The non-dimensional thermal resistance defined by Eqs. (2)–(4) correspond to the spreading resistance directly derived from the heat conduction equation, the resistances from the cross-plane ballistic transport and the size effect of the heat source modeled by Hua et al. [16].

While GaN hosts a relatively large MFP distribution, the gray approximation where a single phonon MFP is used fails in describing the ballistic-diffusive thermal transport accurately [38] and it is

essential to consider the phonon spectrum for the heat spreading modeling with ballistic effects. In the framework of Hua's model, the gray approximation is extended directly to the case considering the phonon spectrum, where modified phonon MFPs are used to provide an effective thermal conductivity described as

$$k_{eff} = \frac{1}{3} \sum_j \int_0^{\omega_j} \hbar\omega \frac{\partial f}{\partial T} \text{DOS}_j(\omega) v_{g,\omega,j} l_{m\_\omega,j} d\omega, \tag{5}$$

and

$$l_{m\_\omega,j} = \frac{l_{0\_\omega,j}}{\left(1 + A_w Kn_{w\_\omega,j} \right)\left(1 + \frac{2}{3}Kn_{t\_\omega,j} \right)}. \tag{6}$$

where l_0 is the intrinsic phonon MFP, and l_m is the modified MFP reflecting the ballistic effect. The subscript '_ω, j' denotes the frequency and branch dependence. The other letters $\hbar$, f, T, v are reduced Planck constant, phonon distribution function, temperature, and phonon group velocity, respectively. With the effective thermal conductivity, the total thermal resistance can be calculated with the heat spreading model, i.e. Eq. (2), where R_{1d_0} is replaced by R_{eff} defined with k_{eff}. However, the comparison between the results from this model and MC simulations considering the phonon spectrum shows that the simple direct extension of the gray model is insufficient to reflect the wide span of the phonon spectrum. To fix the deficiency of the current model, Shen et al. [37] proposed two thermal resistance ratios (correction factors) which are material-independent and addressed the thermal spreading process, ballistic effects, and the influence of phonon dispersion of different materials successfully. In the revised thermal resistance model, $l_{m\_\omega,j}$ is written as

$$l_{m\_\omega,j} = \frac{l_{0\_\omega,j}}{\left(1 + A_w Kn_{w\_\omega,j} \right)\left(1 + \frac{2}{3}Kn_{t\_\omega,j} \right)r_t r_{wg}}. \tag{7}$$

in which r_t and r_{wg} are the thermal resistance ratios

$$r_t = 0.15\ln(Kn_t) + 1.35, \tag{8}$$

$$r_{wg} = -0.17\ln(Kn_w - Kn_{w,0}). \tag{9}$$

(b) Phonon transport along the surface

(a) Phonon transport across the interface

(c) Phonon transport along the interface

Interface scattering

interface

〜➤ Bulk phonon mode   〜➤ Surface/interface phonon mode
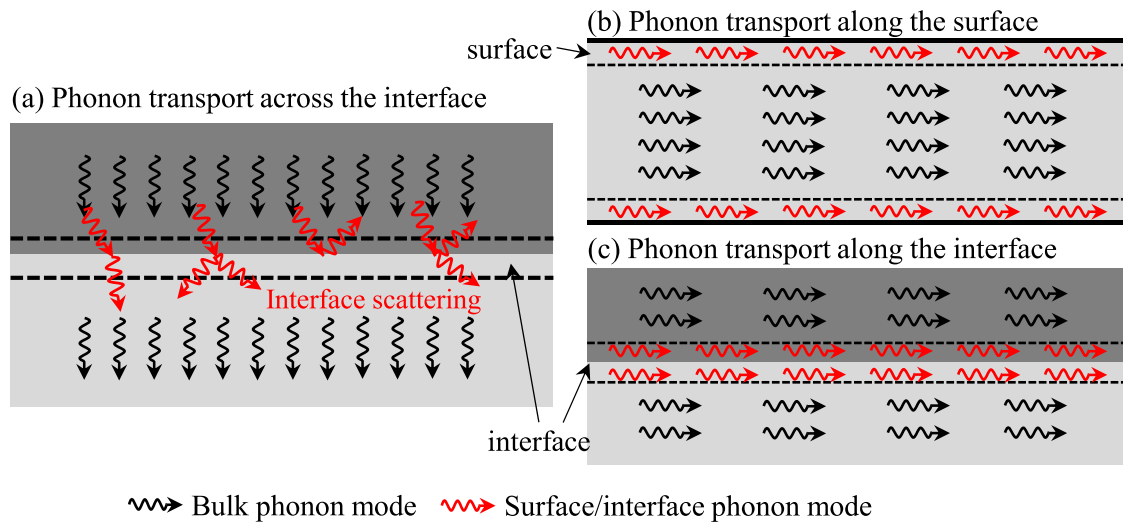
Fig. 6. Phonon transport across the (a) interface and (b)(c) along the interface (surface).

where $Kn_{w,0}$ is a threshold value defined in the revised model. These two ratios can well compensate for the insufficiency of the original model in describing the cross-plane ballistic effect and the size effect of the heat source size. From the Fig. 5(b), it can be found that the finite element method (FEM) based calculations with the model predicted effective thermal conductivity provides nearly the same dimensionless temperature distributions as the MC simulation, especially the peak temperature, while the FEM with bulk thermal conductivity significantly underestimated the peak temperature.

In the end, it is noted that an assumption is used in the derivation above that the thermal spreading effect has been completely described by Eq. (2) in the framework of Fourier's law. However, since the thermal transport in the GaN layer is a thermal transport from a line heat source to a plane heat sink, the actual ballistic transport is more appropriate to be modeled by a radial ballistic heat conduction picture, instead of the cross-plane ballistic heat conduction picture. The anisotropy of the thermal conductivity will be induced due to the different effects of cross-plane and in-plane ballistic transport, and the third part of the non-dimensional thermal resistance, *i.e.*, the thermal resistance from the size effect of the heat source width, may be partly explained as the effect of in-plane ballistic transport.

2.1.3. Interfacial thermal transport

The third characteristic of near-junction heat conduction is the presence of interfacial thermal transport. In GaN HEMTs, composite layered structures are very common, where the interface plays an important role in thermal transport. For example, the key structure in the GaN HEMT is AlGaN/GaN heterostructure, where heat is generated and then transported at this interface shown in Fig. 2(b) and Fig. 6. The GaN channel layer is normally grown on a heterogeneous substrate such as silicon and silicon carbide, which brings an interface. Besides, additional interfaces can be introduced since layers such as the transition layer may be inserted to improve the material quality and maintain electric properties. Currently, understanding of interfacial thermal transport is still limited compared to that of bulk crystal materials since the interface breaks the periodicity of lattice and introduces the atomic disorder and bounded interfacial states. Interfacial thermal transport refers to the thermal transport across the interface qualified by the interfacial thermal resistance or conduction, where the heat flux is perpendicular to the interface with the image of phonon transmission and reflection. With the deepening of the understanding of interfa-

cial phonon properties, the thermal transport at the interface can further contain the phonon thermal transport along the interface mainly referring to the transport of the interfacial phonon modes, *e.g.*, the bounded topology-protected interfacial phonon modes. Interfacial thermal transport is well-known to the science community and has received much attention, which will be reviewed in Section 2.2.3. Since heat spreading resistance is important in layered electronic structures, phonon thermal transport along the interface promises to be important, especially at the hetero-interface between AlGaN and GaN, which requires further investigation and will be discussed in Section 3.2.3.

2.2. Phonon and phonon transport in GaN and GaN HEMTs

2.2.1. Heat generation and near-junction heat conduction

In thermal management for electronics, two critical parameters are the local temperature of the hot spot, and the total near-junction thermal resistance, which is directly determined by the heat generation strength and spatial distribution (affecting the specific heat conduction process). Also, the near-junction heat conduction, *i.e.*, phonon transport, is coupled with heat generation. Considering these characteristics, two important problems are to be solved in near-junction thermal management, including (1) prediction and modeling of heat generation strength and heat generation spatial distribution and (2) near-junction heat conduction modeling considering the non-equilibrium in EPC and phonon transport.

As mentioned in Section 2.1.1, heat generation is a hot electron relaxation process at the hetero-interface. For these issues, comprehensive MC simulations of electron and phonon transport are powerful methods in numerical investigations which is equivalent to solving the hybrid electron and phonon transport equations, while modeling work is more appropriate for engineering applications. Here, progress in these two aspects is introduced and discussed.

i Monte Carlo simulations

In MC simulations for particle transport (Fig. 7(a)), the most important part is the particle properties including scattering properties and drift properties. While the heat conduction is coupled with heat generation in the near-junction region, the equations to be solved by the MC simulation consist of electron and phonon Boltzmann transport equations and their coupling [39–42]. Given the electron and phonon band information, as well as interatomic force constants (IFCs) and coupling matrices at the hetero-
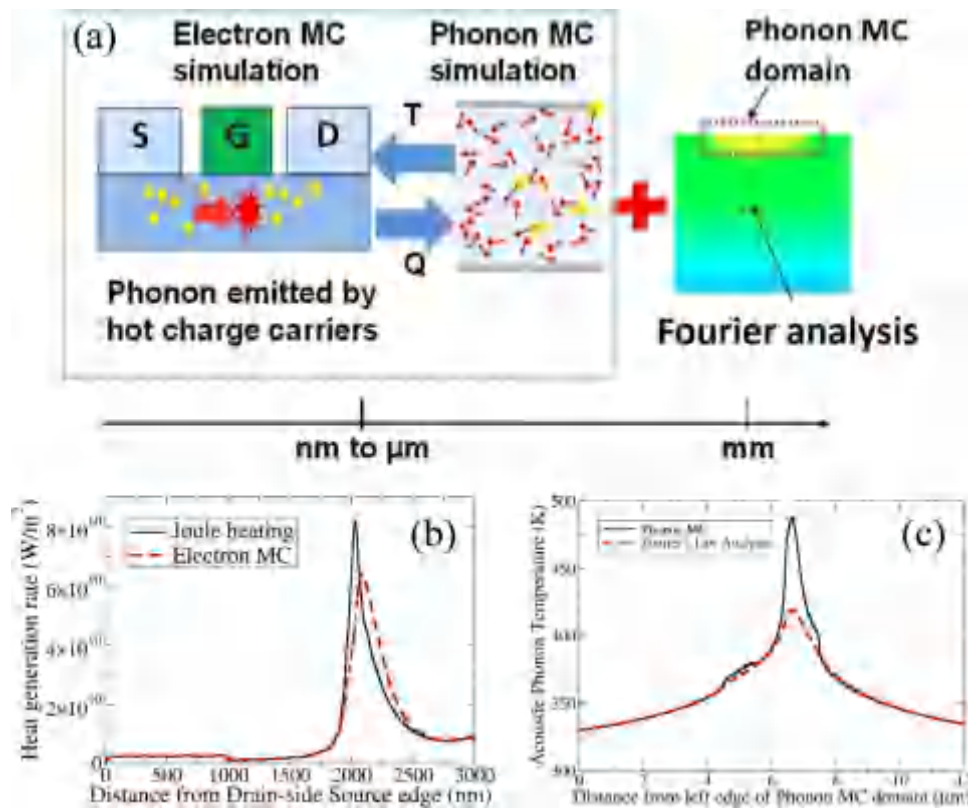
Fig. 7. (a) Hybrid electron-phonon Monte Carlo simulations and Fourier's law based calculations for heat generation and heat conduction in the near-junction region. (b)(c) calculated results from the Monte Carlo simulations for heat generation rate and acoustic phonon temperature. From [Ref. 40].

interface, phonon-electron and phonon-phonon scatterings can be modeled with the Fermi golden rule. Accurate information for electrons and phonons at the interface is difficult to be calculated directly from the first principles so far including harmonic and anharmonic phonon properties since much more phonon modes are present at the interface compared with those in the bulk material. A practical way in simulations is to model electron and phonon bands and electron-phonon scatterings, as well as phonon-phonon scatterings using relaxation approximation [39,40,43–46]. For electron bands, Kane's model [47] is usually used with the form $E_i(1 + \alpha_i E_i) = \hbar^2 k^2 / 2m_{0,i}^*$, where E is the kinetic energy of electrons, m_0^* is the electron effective mass at the band edge, and i is the index for the three conduction band valleys. By solving the Schrodinger-Poisson equation at AlGaN/GaN heterostructure, sub-band energy can be obtained [39,40]. For phonons, properties in bulk materials are used and modeling on dispersion relations will be further adopted, e.g., sine-shaped dispersion $\omega(k) = \omega_{max} sin(\pi k / 2k_0)$ [48,49]. Theoretically, electron-phonon scatterings consist of several types, including polar optical phonon scattering, acoustic deformation potential scattering, intervalley optical phonon scattering, etc., which can be modeled in simulations for a reasonable computational load and will be introduced in the following section. With a more detailed treatment in MC simulations, i.e., considering different temperatures for electrons, optical phonons, and acoustic phonons for the non-equilibrium states, the heat generation, temperature distribution, and hot spot in the heterostructure can be predicted. In practical investigations, the heat conduction problem at the device level is multiscale where both mesoscopic and macroscopic methods are required to catch the ballistic effects and decrease the computational load simultaneously [40,50]. As illustrated in Fig. 7(b) and (c), the predicted heat generation rate and acoustic phonon temperature deviate from those from the calculations based on the classical laws. In specific,

the results show that the heat generation rate from the electron MC simulations is lower than the classical Joule heating rate due to the electron ballistic transport. The acoustic phonon temperature from the MC simulations is higher than that of the calculations based on Fourier's law due to the decrease of the heat conduction capacity from the size effect. However, a critical question still exists on how to evaluate the accuracy of simulation results compared to the real heat generation and transport processes as many models and approximations are used in the simulations at the microscopic level, which mainly include the accuracy for heat generation prediction and thermal transport prediction. Experiments can provide validation for the simulations, which are however limited since only surface temperature fields can be obtained at the device level. In general, errors in simulations will result from approximations for electron bands, phonon bands, EPC, phonon relaxation times, and phonon scattering and transmission at the interface.

i Theoretical modeling

Digging out the specific roles from different parts in simulations separately is still an open question. Theoretical modeling on heat generation and thermal transport can provide different perspectives and benefit the understanding of the physical picture. At the interface, phonon modes may differ from those in bulk materials, known as the interfacial modes. Generally, both bulk phonon modes and interfacial phonon modes exist at the interface. For this picture, the dielectric continuum model and three-dimensional phonon model can be adopted [51–53]. Both half-space modes and interfacial modes are taken into consideration in the former model, where the half-space modes indicate phonons with positive momentum components perpendicular to the interface, while only high-frequency polar longitudinal optical phonons are considered in the latter model. The interfacial modes exist at a very thin layer near the interface and will penetrate exponentially concerning the

distance from the interface. There are two types of penetration layers, *i.e.*, real interfacial regions, one of which is the penetration layer for phonons and the other is that for electrons called the quantum well. The role of the interfacial phonon modes in interfacial EPC is then determined by the relative thickness of the phonon quantum well.

Based on the theoretical modeling for phonons and electrons at the interface, the heat generation at the heterostructure interface can be then calculated accompanied by the electron-phonon interaction Hamiltonian. There are several EPC types in GaN classified according to the phonon branches. For the coupling between electrons and long-wavelength acoustic phonons, the interaction mainly comes from the perturbation induced by the deformation potential of acoustic phonons, with the Hamiltonian [54]

$$H_{e-LA} = a_{nk}(\mathbf{q} \cdot \delta_{\mathbf{R}}), \tag{10}$$

where a_{nk} is the volumetric deformation potential, $\mathbf{q}$ is the phonon wave vector, and $\delta_{\mathbf{R}}$ is the atomic displacement. For wurtzite crystal with non-centrosymmetric, like GaN, the deformation potential will also induce macroscale polarization, with the Hamiltonian [54]

$$H_{pe} = -|e|\phi_{pe}, \tag{11}$$

where ϕ_{pe} is the scalar piezoelectric potential and e is the electric charge. The interaction among electrons and optical phonons is similar to electron-acoustic phonon interaction, described using the deformation potential with the Hamiltonian [54]

$$H_{e-OP} = D_{nk}(u/a_0), \tag{12}$$

which is a short-range interaction, where D_{nk} is the optical phonon deformation potential u is the atomic displacement of optical phonons. For polar crystals like GaN, there is strong interaction among electrons and polar optical phonons induced by the macroscopic electric fields from the polar long-wavelength optical phonons, called the Fröhlich interaction, with the Hamiltonian [54]

$$H_{Fr} = (ieF/q)u_{LO}, \tag{13}$$

where F is the polar coefficient. For phonon with large wave vectors, the EPI is short-range, corresponding to the intervalley scatterings of electrons, with the Hamiltonian [54]

$$H_{iv} = \mathbf{e}_{b\mathbf{q}} \cdot \frac{\partial H_e}{\partial \mathbf{R}} u. \tag{14}$$

where $\mathbf{e}$, u, $\mathbf{q}$, and b represent, respectively, the phonon polarization vector, amplitude, wave vector, and branch number. The parameters and coefficients present above can be calculated from the first principles or by the tight-binding method [54]. With the information above, the energy dissipation rate of the electron system and phonon generation rates can be derived with the aid of the energy conservation equations, which can be further used to calculate the local temperature changes based on the lumped parameter approximation and numerical methods.

2.2.2. Phonon properties from first-principles

Following heat generation, thermal transport in the channel layer and across the interfaces is another very important part of thermal modeling in GaN HEMTs. Phonon properties are critical for thermal transport analyses and thermal conductivity calculations. At present, first-principles calculations can provide detailed microscopic heat conduction information combined with lattice dynamics theory, Boltzmann transport theory, Green's function method, *etc.*, and have become the most powerful numerical methods for investigations of thermal transport properties. The general framework of first-principles calculations for phonon thermal transport investigations is illustrated in Fig. 8. The primary phonon

properties include harmonic phonon properties (phonon dispersion, the density of states, *etc.*), an-harmonic phonon properties (scattering rates, Grüneisen parameter, *etc.*), and phonon properties at surface/interface (phonon-surface/interface scatterings, surface/interface modes, *etc.*).

i Phonon dispersion

For atoms in the lattice, the equation of motion is written as

$$\sum_{j'\beta} D_{\alpha\beta}(jj', \mathbf{q}) e_\beta(j', \mathbf{q}\upsilon) = m_j[\omega(\mathbf{q}\upsilon)]^2 e_\alpha(j, \mathbf{q}\upsilon), \tag{15}$$

where D is the dynamical matrix, $\mathbf{q}$ is the wave vector, υ is the band index or phonon branch index, m is the atomic mass, j and j' denote the indices of atoms in a unit-cell, and e is the eigenvector. The dynamical matrix D is obtained from the transformation of force constants Φ which can be calculated from the first principles based on density-functional perturbation theory or the finite displacement method [56–58]. For phonon dispersion calculations in wurtzite GaN, non-analytical term correction should be considered to describe the long-range interaction of macroscopic electric field induced by the polarization of collective ionic motions near the Γ-point [59].

Phonon dispersion relations of GaN are shown in Fig. 9, where the wurtzite lattice structure of GaN is particularly present in Fig. 9(a). The dispersions from the first principles are consistent with those from experiments [55]. There are 12 phonon branches, consisting of 3 acoustic branches and 9 optical branches. A large gap is present at the frequency 10–15 THz, dividing the phonon branches into high-frequency parts and low-frequency parts, which suppresses the scattering channels from high-frequency optical phonons to low-frequency acoustic phonons and becomes one of the reasons for the high thermal conductivity of GaN. This characteristic is also shown by the phonon density of states in Fig. 9(c). Besides, for the high-frequency part, the dispersions are relatively flat, indicating the small group velocities, while the group velocities for phonons with lower frequencies are large, which is directly confirmed by the group velocity data in Fig. 9(d) and reflected by the thermal conductivity calculations that the phonons with lower frequencies contribute the most to the thermal conductivity (more than 99%).

i Intrinsic phonon scatterings

Intrinsic phonon scatterings include phonon-phonon scattering and phonon-electron scattering, which will be discussed successively in this section. Grüneisen parameter and scattering rate are two important quantities in an-harmonic phonon properties. The former combined with the weighted phase space derived from the phonon dispersions decides the scattering rates. The latter one, *i.e.*, the phonon-phonon scatterings rate, is the most important factor to determine the lattice thermal conductivity, which is calculated according to the perturbation theory [60],

$$\frac{1}{\tau_0} = \frac{1}{N} \left(\sum_{\lambda'\lambda''}^{+} \Gamma^+_{\lambda\lambda'\lambda''} + \sum_{\lambda'\lambda'}^{-} \frac{1}{2} \Gamma^-_{\lambda\lambda'\lambda''} + \sum_{\lambda'} \Gamma_{\lambda\lambda'} \right), \tag{16}$$

where N is the discretized $\mathbf{q}$ points in the Brillouin zone, λ denotes the phonon mode, and $\Gamma^\pm$ are three-phonon scattering rates, which can be calculated based on perturbation theory from the scattering matrices, and Γ denotes the phonon scattering from isotopic disorder. The scattering rate in Eq. (16) is used as the initial value in the iterative solvent for the phonon Boltzmann transport equation. As illustrated in Fig. 10, high-frequency optical phonons have the largest Grüneisen parameter, as well as the largest scattering rates. The isotopic scattering is promising to provide a significant effect on thermal conductivity of GaN, around a 30% decrease, based on the first-principles calculations and Tamura's
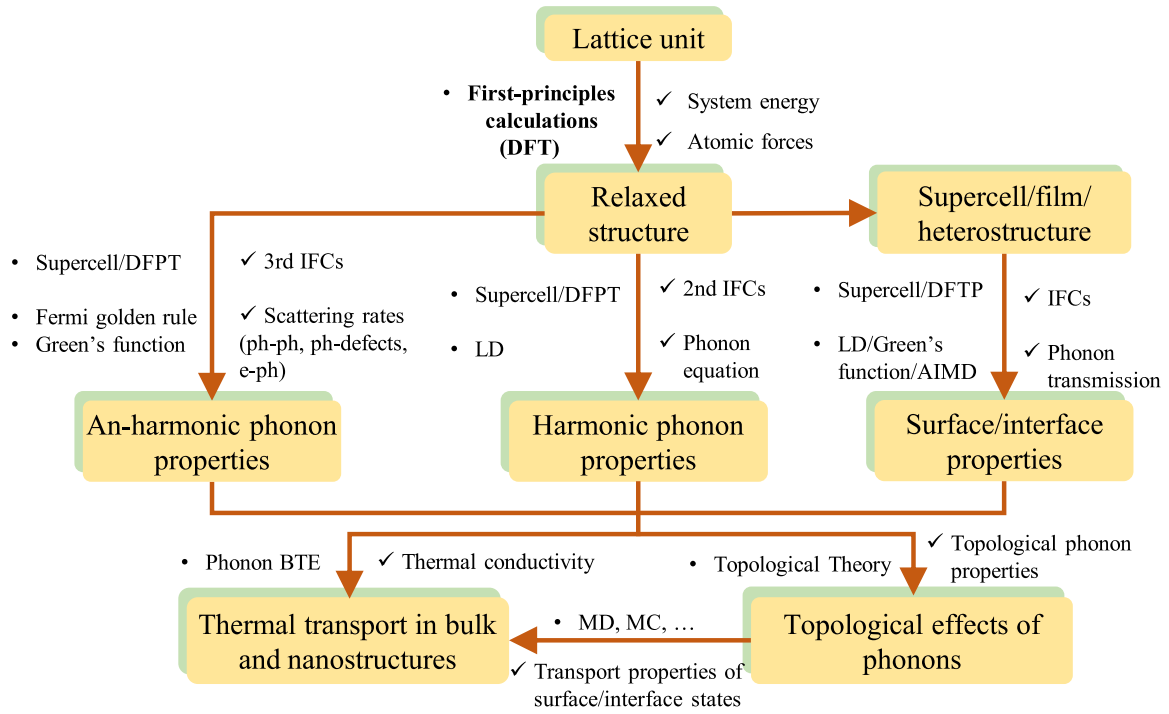
Fig. 8. The schematic diagram for first-principles-calculations-based methods for phonon transport.
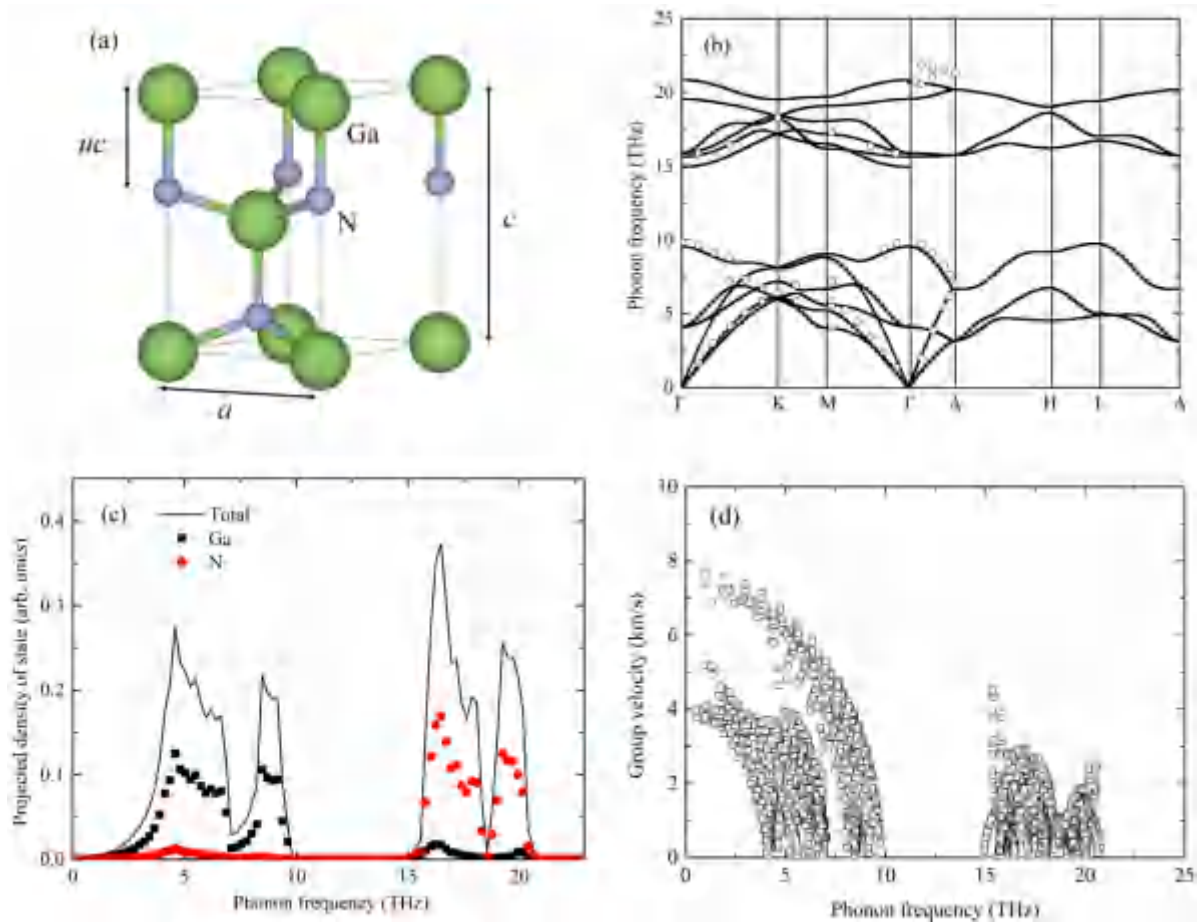
Fig. 9. GaN structure and harmonic phonon properties: (a) wurtzite structure of GaN (b) phonon dispersion relation where the dot indicates the experimental data from ref. [55] (c) phonon density of states (d) phonon group velocity, from [ref. 34].
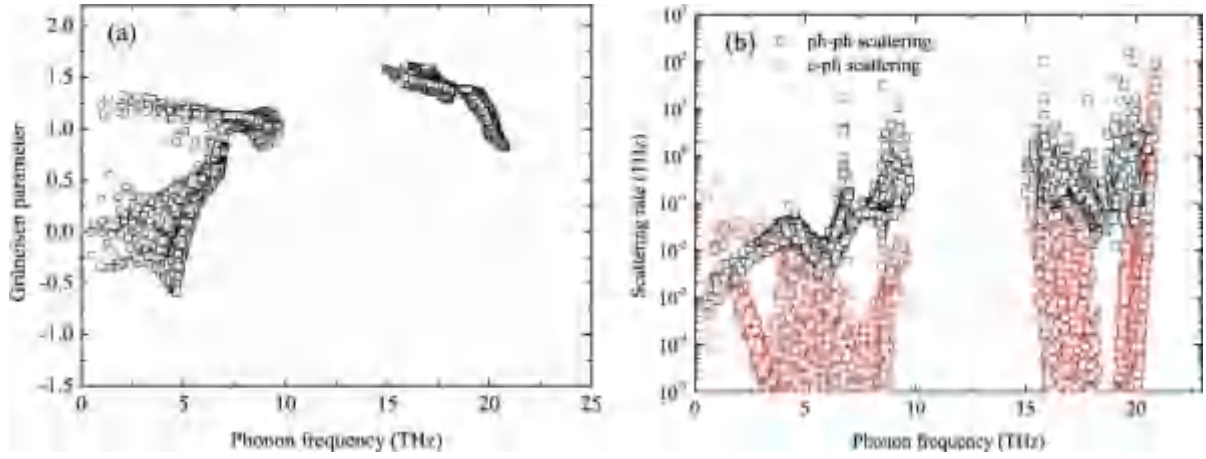
Fig. 10. An-harmonic phonon properties in GaN: (a) Grüneisen parameter (b) phonon-phonon scattering rates and electron-phonon scattering rates, from [ref. 34].

mass variation approximation model for isotopic scattering, as reported by Lindsay *et al.* [61] and confirmed by other researchers [33,34,62]. However, experimental measurements [63] only show a decrease of less than 20%, which implies that the first-principles calculations and Tamura's mass variation approximation may overestimate the role of isotopic disorder in GaN [64].

The electron-phonon scattering results from the electron-phonon interaction, which is confirmed to be significant in both wurtzite GaN [33,34,65] and zincblende GaN [66]. In specific, the electron density distribution around the nucleus determines the atomic interactions, which are then determined by the lattice vibration indirectly. In turn, during the propagation of lattice waves, local atomic distance changes, resulting in changes in electron density distribution and electron energy. This is the general picture for EPC. For ionic or polar crystals, such as GaN, the longitudinal optical phonons with long wavelengths arouse a built-in macroscopic electric field, inducing strong EPC. Theoretically, the former EPC is modeled as deformation potential since it results from the lattice deformation, and the lattice one is modeled as Fröhlich EPC. Currently, the phonon scattering rate from EPC can be calculated from the first principles with a general form [67,68],

$$\frac{1}{\tau_{\mathbf{q}\upsilon}(\omega, T)} = 2\Pi''_{\mathbf{q}\upsilon}(\omega, T)/\hbar, \tag{17}$$

$$\Pi''_{\mathbf{q}\upsilon}(\omega, T) = 2\pi \sum_{mn} \int_{\mathrm{BZ}} \frac{d\mathbf{k}}{\Omega_{\mathrm{BZ}}} |g_{mn,\upsilon}(\mathbf{k}, \mathbf{q})|^2$$
$$\times \left[f_{n\mathbf{k}}(T) - f_{m\mathbf{k}+\mathbf{q}}(T) \right] \delta \left(\varepsilon_{m\mathbf{k}+\mathbf{q}} - \varepsilon_{n\mathbf{k}} - \hbar\omega \right), \tag{18}$$

$$g_{mn,\upsilon}(\mathbf{k}, \mathbf{q}) = \frac{1}{\sqrt{2\omega_{\mathbf{q}\upsilon}}} \langle \psi_{m\mathbf{k}+\mathbf{q}} | \partial_{\mathbf{q}\upsilon} V | \psi_{n\mathbf{k}} \rangle. \tag{19}$$

where $\mathbf{q}\upsilon$ is used to represent phonon mode (wave vector and branch), $\Pi''_{\mathbf{q}\upsilon}$ is the imaginary part of phonon self-energy, g is the electron-phonon matrix, f is the phonon distribution function, ε is the electron energy, ψ is the electron wave function, and $\partial_{\mathbf{q}\upsilon} V$ is the derivative of the self-consistent potential associated with a phonon (mode $\mathbf{q}\upsilon$). The detailed calculation methods are now implemented in an open-source software EPW [67,68]. In Fig. 10(b), the phonon scattering rate from EPC is compared with that from phonon-phonon interaction, which shows that the phonon scattering rate from EPC cannot be ignored for GaN, especially at high frequency [33,34].

i Extrinsic phonon scatterings

Besides intrinsic phonon scatterings, interface, defects, and dislocations can introduce additional phonon scatterings, raising significant effects on thermal transport in GaN. Experimental measurements provided rich raw data of GaN thermal conductivity, considering conditions with different interfacial types, defects density, and dislocation densities. However, it is still a big challenge to dig out microscopic details, such as interfacial modes, phonon-interface scattering, phonon-defect scattering, and phonon-dislocation scattering. In the past decades, semi-empirical analytical models from perturbation theory are the main tools to investigate the phonon-defects and phonon-dislocation scatterings[69,70], where their scattering rates are modeled as

Defects : $\tau_P^{-1} = \dfrac{V_0 \omega^4}{4\pi \bar{v}^3}(\Gamma_M + \Gamma_R),$

$\Gamma_M = \sum_i f_i \left(1 - \dfrac{M_i}{\bar{M}}\right)^2,$

$\Gamma_R = \sum_i 2f_i \left\{ 6.4\gamma \left(1 - \dfrac{R_i}{\bar{R}}\right) \right\}^2. \tag{20}$

Dislocations : $\tau_D^{-1} = \tau_{\mathrm{core}}^{-1} + \tau_{\mathrm{screw}}^{-1} + \tau_{\mathrm{edge}}^{-1},$

$\tau_{\mathrm{core}}^{-1} = \eta N_D \dfrac{V_0^{\frac{4}{3}}}{\bar{v}^2} \omega^3,$

$\tau_{\mathrm{screw}}^{-1} = 0.06 N_D^s b_S^2 \gamma^2 \omega,$

$\tau_{\mathrm{edge}}^{-1} = 0.06 N_D^e b_E^2 \gamma^2 \omega. \tag{21}$

where $V_0 = |a_1 \cdot (a_2 \times a_3)|/4 = a^2 c\sqrt{3}/8$ is the mean volume for each atom in wurtzite GaN, Γ_M and Γ_R are scattering strength from mass difference and defects-induced strain fields. In the equations above, $\bar{v}$ is the mean acoustic velocity, f_i is the concentration of atoms i, M_i is the atomic mass, $\bar{M}$ is the mean atomic mass, R_i is the ionic radius, $\bar{R}$ is the mena radius, γ is the Grüneisen parameter, N_D is the density of the dislocation line, $b_S = c$, $b_E = \sqrt{2}a/3$, η is the weight factor (around 0.55 in general). Here, dislocations can be divided into the dislocation core, screw dislocation, and edge dislocation and are modeled respectively. For the GaN layer in HEMT, edge dislocation is the one with the largest density. In literature, there are also some other modeling types for defects and dislocations [64]. The phonon interface scattering will be discussed in Section 2.2.3.

The scattering rate models above are often used to analyze and explain thermal conductivity results. However, as the variance of thermal conductivities of GaN films is the collective effect of many factors including film thickness, defect type and density, dislocation type and density, stress, and experimental errors, it is still difficult to deduce the scattering properties with analytical models and experimental results [71,72]. Therefore, performing direct cal-
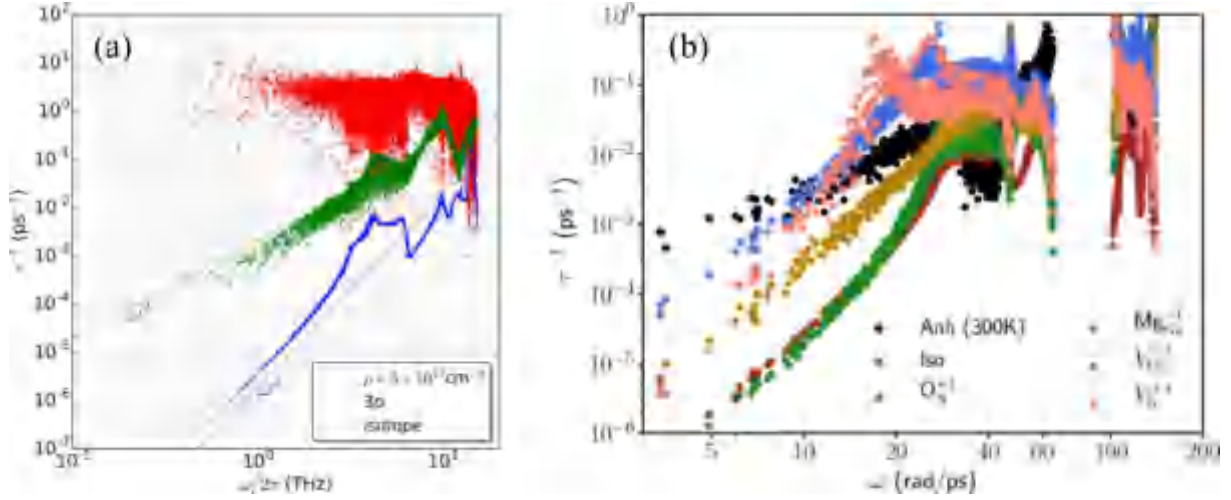
Fig. 11. Phonon scattering rates from (a) dislocations and (b) point defects, from [refs. 208] [72] and [74].

culations for phonon scatterings is highly required and meaningful for basic understanding. Recently progress in first-principles calculations and Green's function-based T-matrix method promoted the calculation of phonon-defect and phonon-dislocation scatterings [72–74]. Specifically, the defect and dislocation models are built within the supercell, then the force constants can be calculated from first principles using the finite-displacement method, with which scattering rates from defects and dislocations can be extracted using the Green's function-based T-matrix method. For dislocations, phonon scattering is approximated as elastic type and the scattering rate is written as [72,73]

$$\frac{1}{\tau_{\lambda,q_1}} = \frac{S}{\omega_{\lambda,q_1}} \sum_{\lambda',q_1'} \left| \langle \phi_{\lambda'}(q_1') | T^+(q_1,\omega^2) | \phi_\lambda(q_1) \rangle \right| \delta(\omega'^2 - \omega^2) \tag{22}$$

where ϕ is the phonon state indexed by a new basis vector q_1 and the compound index λ defined in a mixed-space basis of states. T^+ is the T-matrix consisting of the Green's function and perturbation from dislocations, and S is the ratio of the normalization area of the eigenvector and the scatter's section. For defects such as point defects and vacancies, the phonon scattering rate is in the form of [74]

$$\frac{1}{\tau_{j\mathbf{q}}} = -\chi \frac{\Omega}{V} \frac{1}{\omega_{j\mathbf{q}}} \mathrm{Im} \left\{ \langle j\mathbf{q} | (\mathbf{I} - \mathbf{V}g^+)^{-1} \mathbf{V} | j\mathbf{q} \rangle \right\}, \tag{23}$$

where $j\mathbf{q}$ denotes the phonon branch and wave vector, χ is the number fraction of defects, V is the volume of a defect, Ω is the volume for normalizing phonon state $j\mathbf{q}$, $\mathbf{I}$ is the identity matrix, $\mathbf{V}$ is the perturbation matrix of defect, and g^+ is the Green's function. This process for calculating phonon-defect scattering rates from the T-matrix method has been implemented in open-source software the AlmaBTE [75]. Fig. 11 illustrates the phonon scattering rates from dislocations and point defects calculated from the first principles. The phonon scattering rates from dislocations with a density of 5×10^{13} cm^{-2} are relatively large compared to the phonon-phonon scatterings. For phonon-defect scattering, the scattering rates are also very large with a large defect concentration, and they are different significantly for different defect types. Generally, the supercell approach for building the defect and dislocation models is available for cases with high density, while a small density will result in a large supercell model accompanied by increased computational consumption.

For more detailed phonon scattering properties with defects and dislocations, the molecular dynamic (MD) simulation is

promising to be a powerful tool. Based on a series of molecular dynamics techniques in dealing with lattice dynamics, including normal mode decomposition, heat current decomposition [76], modal temperature calculation [77], modal thermal conductivity calculation [78], inter-mode energy exchange calculation [79], *etc.*, phonon properties in different types of solids can be derived in the modal level, providing a very comprehensive picture for phonon transport. At present, investigations of GaN thermal transport with defects and dislocations using the molecular dynamic method are still much required. Sun et al. [80] performed molecular dynamic simulations on thermal transport in PbTe with dislocations and confirmed the large deviation of dislocation scattering to Matthiessen's rule. While the molecular dynamic method shows great advantages in heat conduction simulations, it is also limited due to its apparent deficiencies. The molecular dynamic method is a classical method, not appropriate for conditions below the Debye temperature and conditions where quantum phenomena are significant. Besides, for many solids systems, especially emerging new material systems, effective potential functions for molecular dynamic simulations are still not available. In modeling lattice thermal transport, molecular dynamic simulation results depend on many calculation details and settings, including heat baths and boundary settings in non-equilibrium molecular dynamic (NEMD) and convergence of auto-correlation function in equilibrium MD (EMD). Fortunately, recent progresses in first-principles calculations and machine-learning method [81–84] have enabled the potential function modeling with very high accuracy, opening the opportunities for many kinds of researches which are not possible before. And also, with comprehensive analyses of molecular dynamic simulations and BTE-based calculations, a unified understanding of them was proposed, clarifying the effects of heat baths and boundary settings on molecular dynamic simulation results [85]. Therefore, the molecular dynamic method is promising to be a very useful way to study the thermal transport in GaN and GaN-based nanostructure.

2.2.3. Thermal conductivity and interfacial thermal resistance
i Thermal conductivity

For engineering-level simulations, macroscopic thermal physical quantities are essential, which mainly include thermal conductivity and interfacial thermal resistance. In experiments, various methods are used, such as the 3ω method [86–92] and time-domain thermoreflectance (TDTR) [93–96]. The 3ω method is an effective electrical method for thermal conductivity and interfacial thermal

Table 1
Thermal conductivity of GaN from literature.

Data sources	Maximum values (W/mK)	Methods
Asnin et al. [97]	180	Scanning thermal microscope
Florescu et al. [98]	210	
Jezowski et al. [99]	269	Axial stationary heat flow method
Slack et al. [100]	220	
Jezowski et al. [101]	230	
Jagannadham et al. [102]	280	3ω
Churiukova et al. [91]	280	
Luo et al. [103]	155	
Paskov et al. [104]	243	
Rounds et al. [105]	224	
Mion et al. [106]	230	
Kamano et al. [107]	145	TTR (Transient Thermo-reflection)
Beechem et al. [108]	180	TDTR (Time-Domain Thermo-reflection)
Zheng et al. [63]	249	
Li et al. [71]	220	
Shibata et al. [109]	253	Laser flash
Lindsay et al. [61]	400	First principle-based phonon Boltzmann transport equation (BTE)
Garg et al. [62]	390	
Yang et al. [33]	420	
Yuan et al. [110]	330	
Tang et al.[34].	263	
Togo et al. [111]	270	

resistance measurement, which is firstly proposed by Cahill [90], and then developed by many other researchers. The basic principle of the 3ω method is to use the frequency-domain characteristics of the surface temperature. In the experiment, a metal line is deposited on the sample surface as a heater and sensor simultaneously. A harmonic electric current is applied to this heater, reducing a 2ω Joule heating and the corresponding 2ω temperature oscillation. The voltage in the sensor then contains 1ω and 3ω components, where the magnitude of the latter one is much smaller than the former. The 3ω component gives the 2ω temperature signals, which can be used to derive the thermal physical properties including thermal conductivity, interfacial thermal resistance, *etc*., based on specific thermal modeling and multiple different experimental measurements. In the development process of the 3ω method, the basic principle "1ω current to 3ω voltage" remains the same, while the electrode (heater and sensor) design in experiments can vary to improve the measurement efficiency, which requires different thermal modeling. The TDTR method is another powerful thermal conductivity measurement method for bulk and film materials. As the name indicates, time-domain characteristics are adopted in this method. Before the experimental measurements, a metal film should be also deposited on the sample which is used as a heater and thermometry sensor. A pump laser with high energy heats the film surface, and then a probe laser with low energy and a continuous-time delay is used to detect the temperature changes of the sensor under the pulse heating, based on the linear relation between the reflection coefficient and temperature of the metal film. Like the 3ω method, the direct measured physical quantity is surface temperature, and further thermal physical properties are derived based on thermal modeling. Since the pulse width of an ultrafast laser is very short, around a picosecond, a very high time resolution and spatial resolution can be obtained for both thin-film measurement and microscale particle process investigations.

Table 1 shows the representative experimental thermal conductivity data from the literature. At present, a relatively large distribution is observed from these data, which is mainly attributed to the difference in the quality of GaN samples. Up to now, the most popular sample-grown method for GaN is heteroepitaxy with the metal-organic chemical vapor deposition method, and the large-

scale GaN-grown technique is still under development. The experimental data show that the largest thermal conductivity of GaN is around 280 W/mK. A more comprehensive experimental thermal conductivity data can refer to [ref. 64].

Simulation work on the thermal conductivity of GaN is mainly performed by the first-principles calculation method [33,34,61,62,110,111]. Under the framework of particle nature, phonon transport is formulated by the phonon Boltzmann transport equation (BTE) [112],

$$\frac{\partial f}{\partial t} + v_g \cdot \nabla f = \frac{\partial f}{\partial t}|_{\text{collision}} \tag{24}$$

where f is the phonon distribution function, t is time, v_g is the phonon group velocity. The three parts represent the changes in phonon distribution function concerning time, drift motion, and scatterings among phonons. By solving the phonon BTE, lattice thermal conductivity can be obtained as [60]

$$\kappa_{\alpha\beta} = \frac{1}{k_B T^2 \Omega N} \sum_{k,s} f_0(f_0 + 1)(\hbar\omega_{k,s})^2 v_{k,s}^\alpha v_{k,s}^\beta \tau_{k,s} \tag{25}$$

where k_B, T, Ω, N are Boltzmann constant, temperature, the volume of the unit cell, and the number of wave vectors, respectively. The alphabet α, β denotes the direction (x, y, z in cartesian coordinates), f_0 is the phonon distribution function at equilibrium state, *i.e.*, Bose-Einstein distribution, and $\hbar$, ω, v, F are reduced Planck constant, phonon angular frequency, group velocity, and effective MFP. Phonon mode is expressed using wave vector q and branch υ. Though few empirical choices exist in these calculations, there are still differences among different data. The total errors can be divided into physical errors, *i.e.*, exchange-correlation functional and pseudopotential, and mathematical errors, *i.e.*, mesh sampling for momentum space, convergence criterion for electronic and atomic calculations, and the size of the supercell. The differences in results mainly include the difference in lattice parameters, magnitudes of phonon dispersions and scattering rates, and thermal conductivity values. With the recommended functional (PBE) and pseudopotential (considering the electrons in 4d orbits), large supercell, and momentum meshes (with convergence test), the thermal conductivity of pure GaN is 263 and 271 W/mK for the in-plane and out-of-plane conditions [34]. Fig. 12(a) and (b) depict the GaN thermal conductivity data concerning the temperature from the first-principles calculations. The data from directly solving the phonon BTE and relaxation time approximation (RTA) are compared. The results show that RTA only introduces a relatively small deviation of less than 10%, indicating the weakness of normal phonon scatterings in GaN. Under the framework of the phonon Boltzmann transport theory, the thermal conductivity of GaN concerning the point defects, dislocations, isotopes, electrons, and the interface can be calculated from the first principles using Green's function method and theoretical models. For example, the EPC can be calculated from the first principles, and the extra scattering rates from the EPC can be added to the original total scattering rates simply using the Matthiessen rule.

Dimensionless cumulative thermal conductivity results concerning phonon frequency and free path are shown in Fig. 12(c) and (d), providing a quantitative description of the distribution of thermal conductivity with phonon frequency and free path. The contribution from phonons with a frequency less than 10 THz (acoustic phonons and low-frequency optical phonons) is more than 98% while the contribution from high-frequency optical phonons can be neglected. Specifically, more than 90% of thermal conductivity is attributed to phonons with a frequency less than 6.4 THz. The phonon free path is up to 2.1 μm when dimensionless cumulative thermal conductivity reaches 90% and mainly ranges from 100 to 2000 nm under the free state, which is quite large and supposed to bring about a strong size effect in thin GaN film.
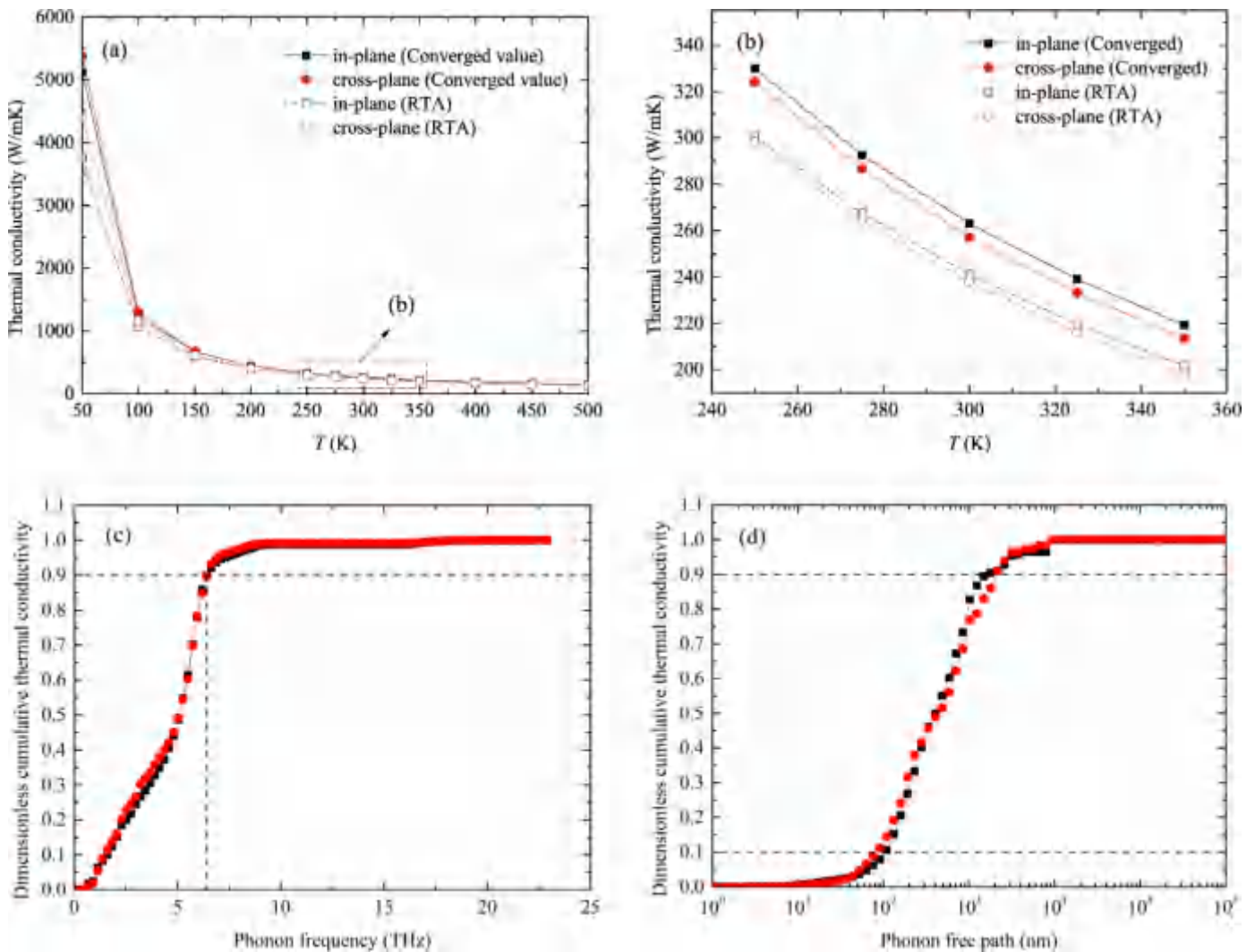
Fig. 12. GaN thermal conductivity concerning the temperature, frequency, and free path, from [ref. 34].
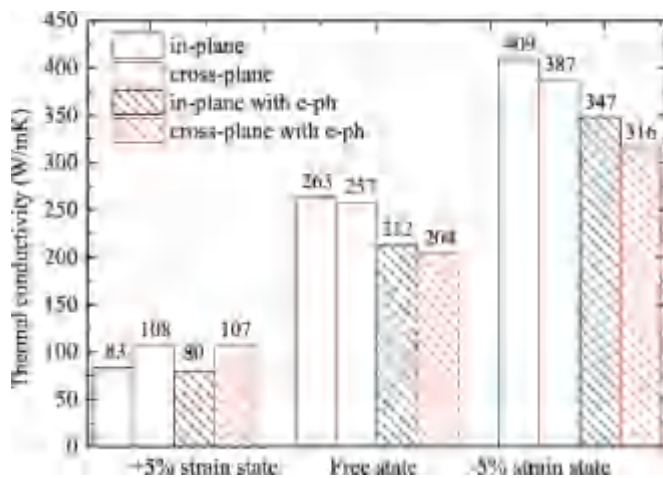
Fig. 13. Effect of EPC on thermal conductivity of GaN at different strain states, from [ref. 34].

Since EPC is proved to be very strong in wurtzite GaN, its effect on thermal conductivity was also investigated using the Matthiessen rule. The results in Fig. 13 show that the EPC indeed decreases the lattice thermal conductivity significantly, around 20%

[33,34,65]. Combined with the spectral thermal conductivity analyses [34], it is deduced that the decrease of the thermal conductivity by EPC results from the strong EPC for phonons of all frequencies, instead of EPC for high-frequency LO phonons only, since the contribution of the high-frequency phonons (the highest six branches) to the lattice thermal conductivity is small (around 1%), and increase in scattering rates for this part of phonons (decrease of the relaxation time) will not significantly decrease the lattice thermal conductivity. The decrease of thermal conductivity of wurtzite GaN by EPC is also reported by Anish and Cao's simulation work recently [44]. An electron-phonon MC simulation was performed in GaN structures, where both the EPC from deformation potential and the Fröhlich EPC are modeled in the simulations. Matthiessen's rule and the relaxation time approximation are adopted for U, N, and impurity phonon scatterings while phonon-electron scattering is modeled using the emission and absorption processes. 16%−22% reduction of lattice thermal conductivity was found for samples of varying thicknesses, consistent with the results by first-principles calculations combined with phonon Boltzmann transport equations.

In practical applications, a thermal conductivity model with reasonable accuracy will be desired. The thermal conductivity of GaN is mainly affected by the point defects, dislocations, film thickness, isotopes, and temperature. Combining the thermal conductivity data from the first-principles calculations and the classi-

cal Callaway thermal conductivity framework [69],

$$\kappa = \left(\frac{k_B}{\hbar}\right)^3 \frac{k_B}{2\pi^2 \bar{v}} T^3 \int_0^{\Theta_D/T} \frac{\tau_T x^4 e^x}{(e^x - 1)^2} dx \qquad (26)$$

where $\bar{v}$ is the average speed velocity and Θ_D is the Debye temperature, the authors proposed a thermal conductivity model for GaN thin films considering the anisotropy from the size effect in different directions, *i.e.* in-plane and cross-plane [64]. The total relaxation time τ_T is calculated by summarizing the different relaxation times using the Matthiessen rule, where the relaxation times for different conditions (Umklapp scattering, isotopic scattering, point defect scattering, and dislocation scattering) are obtained from the first principles (the former two scattering types) and the semi-empirical models (the latter two types). The boundary scattering is not simply added to the total scatterings but treated using a suppression function derived from the Boltzmann transport equation to describe the different size effects in-plane and cross-plane conditions. The parameters/coefficients in this model for Umklapp and isotopic conditions can be obtained by fitting the results from the first-principles calculations [64].

Currently, comprehensively understanding the thermal conductivity of GaN is still challenging due to the following reasons. First, the empirical part in first-principles calculations makes that final thermal conductivity results differ for the different exchange-correlation functional selections [34], as mentioned above. In experimental research, systematical information for the quality of GaN crystals is essentially required while it is currently still difficult to grow GaN crystals of large scale and high quality. As a result, a standard value of thermal conductivity for pure GaN crystal as the verification used in theoretical studies, especially in first-principles calculations, is still lacking and the consistent conclusion for thermal conductivity of GaN cannot be reached [64]. Consequently, characterizing systematically the crystal quality, as well as the state of the crystals, generally including the defects (vacancies, doping, impurities) concentration, dislocation density, degree of isotopes, and strain field, in experimental measurements is quite essential at present. Also, limited by the finite size used in first-principles calculations, the effects of defects and dislocations present in real GaN samples on thermal conductivity are still not clear, making it more difficult to explain the experimental results with theoretical modeling [72]. Digging out the influence of each factor requires more experimental and molecular simulation studies in the future.

As another important wide bandgap semiconductor, silicon carbide (SiC) has also received lots of attention for its electric and thermal transport properties [113–118]. SiC has many polytypes including the cubic phase (3C-SiC), hexagonal phase (2H, 4H, 6H SiC), and rhombohedral phase, and all of them host large thermal conductivity [63,115,116,119]. The most popular three types are the cubic one (3C-SiC) with zincblende structure, the 4H-SiC, and 6H-SiC where H means the hexagonal lattice and the number means the stack layers of the Si-C atom pairs. Wurtzite structure (2H) is the most unstable configuration compared with the cubic, 4H, and 6H-SiC where the 4H type hosts the lowest energy [118]. Among all polytypes, hexagonal polytype SiC possesses similar lattice structures as well as the same space groups with the wurtzite GaN discussed in this work and is also popularly used as the substrates in GaN HEMT due to the small lattice mismatch. For 4H-SiC, it shows a high absolute value and significant anisotropy in the lattice thermal conductivity. In first-principle calculations, in-plane and out-of-plane thermal conductivities of 4H-SiC at room temperature are around 475 and 325 W/mK respectively [115], which are consistent with the later experimental results by Qian et al. [116], where in-plane and out-of-plane thermal conductivities of unintentionally doped semi-insulating 4H-SiC are 471 and 324 W/mK, respectively.

Both the anisotropy and the absolute value of thermal conductivity are much larger than those of wurtzite GaN. The experimental measurement work by Zheng et al. [63] showed that the thermal conductivity of 4H SiC is 60–70% larger than that of GaN at all temperatures (150–850 K). Illustrated by experimental results of the accumulated thermal conductivity concerning the phonon MFP [119], the largest phonon MFP in 4H-SiC is as long as 10 μm, and the phonons with MFP larger than 4.2 μm contribute 50% of the bulk thermal conductivity at room temperature, while the corresponding phonon MFP is 1 μm in wurtzite GaN. Though atom Si and C are both non-metal atoms, SiC shows noticeable ionicity compared with the elemental crystals, *e.g.*, silicon and diamond. In ref. [120], the large thermal conductivity of 3C-SiC is attributed partly to the light atomic masses and stiff atomic bonds which induce large acoustic phonon velocities and high phonon frequency scale, and a relatively large mass ratio between Si and C resulting in the large phonon frequency gap. This is also applicable for *n*H-SiC theoretically. However, the question "why is the thermal conductivity of SiC much larger than that of GaN?" is still not well addressed to now and more depth investigations are essential in the future.

i Interfacial thermal resistance

Since it has been mentioned above that for HEMT-like layer structures, interfacial thermal transport plays an important role in near-junction heat conduction. Due to the lattice mismatch between GaN and substrates, and the complex energy transfer process, interfacial thermal transport is affected by many factors. Interfacial thermal resistance (ITR), or thermal boundary resistance (TBR), is an important topic in thermal transport studies [121,122]. Basically, for an atomic level contacted interface, ITR mainly results from the intrinsic properties of materials at each side, matching degree of phonons on two sides, the boundary properties of each layer, the detailed structures of the interfacial zone, and the contact strength, *i.e.*, interatomic forces between the two sides. From an ideal scenery, a sharp interface will induce additional phonon scatterings including elastic and inelastic ones besides the internal phonon scatterings. The breaking of periodicity can generate new phonon modes called interfacial modes localized within nanometers from the interface [123–127], part of which can provide a bridge for mismatched phonons with enhanced inelastic scatterings. Instead of a purely geometrical dividing interface, the real interface is a transition region with measurable thickness in practice. In this region, the lattice structure may change significantly compared with that in bulk materials, and changes from single-crystal to polycrystal, nanocrystal, and amorphous can happen, where atoms on each side may be mixed.

Currently, ITRs of GaN/Sapphire, GaN/Si, GaN/SiC, and GaN/diamond in GaN HEMTs have been both calculated and measured systematically. The ITR in GaN structures can be measured using the above two experimental methods for thermal conductivity measurements. Basically, for both electrical and optical methods, the measurements contain two parts including the temperature measurement and the derivation of the thermal physical properties based on the thermal modeling. Hua et al. [92] provided a systematical discussion on the four typical methods for ITR, including the TDTR, Raman spectroscopy, steady-state electrical method, and 3ω method. While a very high frequency can be reached in TDTR and frequency-domain thermoreflectance (FDTR), a frequency-domain version of the transient thermoreflectance (TTR) method, and guarantee a small heat penetration length, this type of method shows relatively high sensitivity to the ITR. However, complex thermal modeling in the data analyses is unavoidable since the basic structures in experiments are stable, which may introduce relatively complicated errors. The Raman spectroscopy method mainly suffers from the temperature

Table 2
Interfacial thermal resistance data from experiments in the literature.

Interface	ITR (m²K/GW)	Temperature (K)	Transition layer	Methods	Sources
GaN/Sapphire	120	300	AlN	Raman	Ref. [128]
	125–333	300	–	TTR	Ref. [129]
GaN/Si	33	573	AlN	Raman	Ref. [128]
	7 − 10	300–550	AlN	TDTR	Ref. [130]
	7.8	300	AlN	TDTR	Ref. [130]
	5.3–7.0	300	AlN	TDTR	Ref. [131]
GaN/SiC	8 − 60	330–520	AlN	Raman	Ref. [132]
	14.9–50	300	AlN	Raman	Ref. [132]
	15–50	300	AlN	Raman	Ref. [132]
	4 − 5	300–550	AlN	TDTR	Ref. [133]
	3.9–4.9	300	–	FDTR	Ref. [134]
	5.3	300	AlN	TDTR	Ref. [130]
	4.4–5.6	300	AlN	TDTR	Ref. [135]
	28–38	300	AlN	Raman	Ref. [128]
	33	300	AlN	Raman	Ref. [128]
	5.9	300	–	TDTR	Ref. [136]
	4.4	300	–	TDTR	Ref. [136]
GaN/Diamond	<10	300	–	Raman	Ref. [137]
	36–47	300	AlN	TDTR	Ref. [138]
	40	>970	adhesion layer	TDTR	Ref. [138]
	27.0	–	dielectric	Raman	Ref. [139]
	35.7	–	dielectric	Raman	Ref. [139]
	17.8	>870	dielectric	Raman	Ref. [135]
	28.5	–	SiNx	TDTR	Ref. [135]
	12.0	–	SiNx	TTR	Ref. [140]
	17.2	>970	SiNx	TDTR	Ref. [141]
	10	–	SiNx	TDTR	Ref. [142]
	6.6	–	SiNx	TTR	Ref. [143]
	18.8	300	Si	TDTR	Ref. [93]
	10.8	300	Si	TDTR	Ref. [93]

measurement accuracy issue though the signal is sensitive to the ITR. Electrical methods generally do not process very high time and spatial resolution compared with optical methods, but they are easily operable and hold a relatively large space for specific electrode design. This advantage is very important for the further development of this method. By performing electrode design and measurement processes, Hua et al. [92] proposed an improved 3ω method, called the two-sensor 3ω–2ω method to effectively measure the thermal conductivity and ITR simultaneously with smaller errors compared to the conventional 3ω method. In the practical experiment, two sensors (a wide one and a narrow one) are firstly deposited on the sample surface, then three steps are required to derive the thermal conductivity of the sample film, the thermal conductivity of the substrate, and the ITR, respectively. The advantage of the electrical method, *i.e.* large design space, is fully utilized in this improved method, of which the feasibility is also guaranteed with the aid of the inverse heat transfer problem method.

Table 2 shows the interfacial thermal resistance data from experiments in the literature. As mentioned above, the transition layer (TL) is usually adopted to release the strain and lattice mismatch during the GaN growth, of which the thickness varies from ten to a hundred nanometers. Therefore, the ITR in structures with transition layers are effective ITRs consisting of the GaN/TL ITR, TL thermal resistance, and TL/substrate ITR. In experiments, ITR data have a large distribution since the ITR depends on many practical factors, while the magnitudes are consistent. Generally, it can be deduced from Table 2 that ITRs of GaN/SiC are the lowest compared with the other three types, which is reasonable that SiC has the smallest lattice mismatch with GaN.

Calculating the ITR in practical cases accurately and distinguishing the contributions from each influence factor are still challenging. Generally, ITR can be modeled using the acoustic mismatch model, diffusive mismatch model, and their modifications [122], and discovered in detail with the simulation method including

the wave packet method, molecular dynamics simulations, non-equilibrium Green's function method, *etc*. Though reproducing the ITR data in simulations is not easy (simulation data can be one to two magnitudes larger than the experimental data), the simulation methods are still powerful in theoretical studies for digging out microscopic physics. The wave packet method can be adopted to analyze the phonon transmission and reflection at the interface for specific modes. The non-equilibrium Green's function method can provide interface states and transmission spectrum accurately with the interatomic force constants from the first-principles calculations. In the non-equilibrium Green's function method, a typical system consisting of a heat zone, cold zone, and center scattering zone is built. And the essential input is the Hamiltonians of each part and their interactions, *i.e.* the interatomic force constants. Green's functions are then derived from this system, which is used to calculate phonon conductance based on the Landauer formula. Currently, the harmonic approximation is mostly adopted and only second force constants are used for the generation of the Green's function, which is available for ballistic transport without scatterings. To now, researchers have performed investigations on the GaN/substrate interface thermal transport using the first-principles calculations based on the non-equilibrium Green's function method, including the GaN/AlN graded and abrupt interface [144,145], and GaN/ZnO interface [146]. In the work by Carlos et al. [144], the uncertainty benchmark work for calculating ITR using the first-principles-calculations-based Green's function method was performed. The graded interface, *e.g.*, GaN/AlN superlattice graded interface, can benefit the dislocation condition in the GaN layer during the heteroepitaxial growth process. However, it also introduces additional thermal resistance at the interface. Ambroise et al. performed the investigations on different GaN/AlN graded interfaces using the ab initio Green's function method and found suggested that an optimized zone exists for the thickness of the graded interface and dislocation density [145]. The phonon-interface scatterings including elastic and inelastic ones require

the implementation of Green's function method with anharmonicity, *i.e.*, higher-order force constants. Recently, an-harmonic modeling for the non-equilibrium Green's function method has been reported, which is promising to obtain more detailed information about phonon-interface scattering and its contribution to interfacial thermal transport [147].

To model and calculate the ITR, approximations have to be adopted in the methods above. However, these approximations may be too simple for practical cases, which can be thrown away in MD simulations [148]. First, the phonon-interface scattering can be divided into elastic and inelastic scattering. The former mainly refers to the two-phonon scattering process, while the latter refers to three-phonon scattering processes as well as other high-order phonon scattering processes [123,124], for both bulk and interfacial phonons. The existence of interfacial phonon mode implies the dynamics characteristic of the interface, requiring a simulation at finite temperature or a phonon scattering analysis considering anharmonicity at the interface. Besides, the real interface is a dynamic and rough interface, which is difficult to model in first-principles calculations and the non-equilibrium Green's function method calculations. Therefore, the molecular dynamics simulation with the aid of machine learning potential functions can provide a more depth understanding of phonon-interface interaction, interfacial phonon modes, and interfacial thermal transport [81–84]. In MD simulations, all phonon properties at the interface such as interfacial modes, and elastic and inelastic phonon scatterings at the interface can be extracted. With the MD technique, the ITRs in GaN composite layers have been performed in the past years, though based on empirical potentials. The results may not agree well with the experimental measurements due to the interface modeling and errors from potential functions, but there are still valuable conclusions from the simulations. It is found that GaN/SiC and GaN/AlN interfacial thermal conductance can be enhanced by introducing intermediate layers, two-dimensional materials (graphene, *etc.*), interfacial morphology engineering, interfacial lattice structure tuning, and increasing pre-phonon scattering using the isotopes [149–157].

3. Tuning mechanisms for thermal transport in GaN and GaN HEMTs

The final goal in thermal management for electronics is to decrease the local temperature of hot spots by bringing out the generated heat flux effectively. Consequently, decreasing the total thermal resistance is the direct objective, which includes increasing the thermal conductivity of each functional layer and decreasing the ITR between layers as much as possible. Based on the thermal resistance analyses in electronics, the thermal resistance consists of an intrinsic part and a process-dependent part. The latter one, *i.e.*, thermal spreading resistance in GaN HEMTs, contributes the most to the total thermal resistance. Therefore, besides decreasing the intrinsic thermal resistance, manipulating heat flow is also another important tuning objective to decrease the spreading resistance.

Compared to the understanding of phonon transport in GaN, exploring the methods to effectively cool the GaN HEMTs based on the present understanding and knowledge is a more difficult job. The typical methods for near-junction thermal management in GaN HEMTs at present are mainly focused on the usage of materials with high thermal conductivity [2,158-164]. In GaN HEMTs, four different types of substrates can be selected, including sapphire, silicon, silicon carbide, and diamond. The diamond holds a very high thermal conductivity, which can decrease the total near-junction thermal resistance and junction temperature. However, it is expensive and not available for widespread commercial applications. Another method to increase the heat dissipation capacity of the substrate is to design microchannels in the substrate region

and regions next to the channel layer, known as the embedded microchannel method [26,27]. Besides advancing the substrate, the passivation layer can be also replaced with the material of higher thermal conductivity (*e.g.*, polycrystalline diamond) while this layer normally consists of SiN with low thermal conductivity and is approximated as a thermal insulation layer. As mentioned before, thermal simulations confirmed that the thermal spreading resistance dominates in the near-junction region and the channel layer is the part contributing the most resistance, just simply inserting high thermal conductive materials may not receive the expected income, and the tuning method to enhance the thermal transport in GaN and along with the AlGaN/GaN interface becomes more critical. Herein, thermal transport tuning work for semiconductors will be discussed in detail, mainly concentrated on how to increase the thermal transport in GaN, as well as in GaN nanostructures since the thickness of the GaN layer in HEMT is around 1 μm and the phonon MFP is long enough to stimulate the ballistic-diffusive thermal transport.

3.1. An overview of phonon transport tuning

Tuning phonon transport has been a long-term goal in heat conduction research, which is essential for practical applications and theoretical progress. In principle, developing tuning methods relies on the understanding of phonon and phonon transport, as illustrated in Fig. 14. Phonon physics uncovered now can be classified into three categories based on the different nature, including particle nature, wave nature, and topological nature. The tuning theories, such as phonon transport in the ballistic-diffusive regime, are developed based on the understanding of phonon physics, which is then used to guide the explorations of tuning methods.

At the macroscale, heat flow manipulation is performed under the basis of Fourier's law and coordinate translations, with which thermal metamaterial with various functions can be created [165]. Since the start of microscale heat transfer research in the last 90 s, the understanding of microscale heat transfer physics has been promoted significantly, which also benefits a lot to the phonon transport tuning. Generally, the phonon is a quantized particle of lattice vibration, with particle nature and wave nature, which is much like electron and photon, especially in transport phenomena. When the characteristic propagation length of phonons (phonon MFPs) is much larger than their characteristic wavelength (coherence length), phonons can be treated as particles. Then, phonon transport can be described as phonons' drift motion and phonon scatterings including phonon-phonon scatterings, phonon-boundary scatterings, phonon-defect scatterings, phonon-dislocation scatterings, *etc.* Detailed phonon transport phenomena differ for conditions when different phonon scattering mechanisms dominate. When resistive phonon scatterings dominate, phonon transport is in the diffusive regime, formulated by Fourier's law. If phonon-boundary scatterings dominate, phonon transport would be in the ballistic-diffusive regime, showing a non-Fourier heat conduction phenomenon. The other kind of non-Fourier heat conduction phenomena, *i.e.*, phonon hydrodynamics transport, would occur when phonon normal scatterings dominate. When the characteristic propagation length of phonons is comparable to or even less than the characteristic phonon wavelength, the particle-based description fails and phonons should be treated as waves where wave interference and diffraction, *etc.*, are important [112]. Besides the particle and wave nature, recent research reported the topological nature of phonons [166,167]. The research on the topological effects of phonons, which is regarded as the frontier progress in phonon physics, will be discussed systematically towards the applications in tuning phonon transport of GaN and GaN nanostructures in Section 3.2.3. As a brief introduction, phonon physics is expressed in Fig. 15, where three main pictures
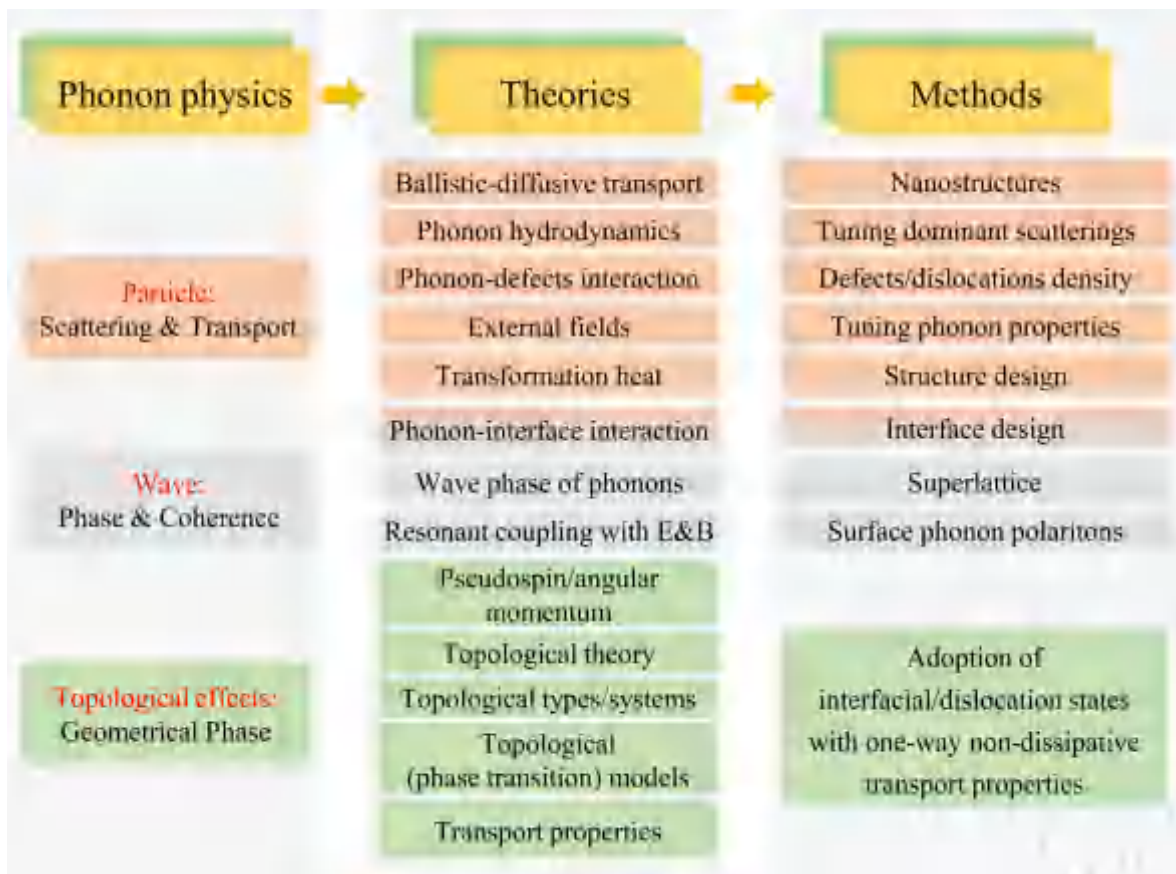
Fig. 14. Phonon physics and corresponding tuning mechanisms and methods.
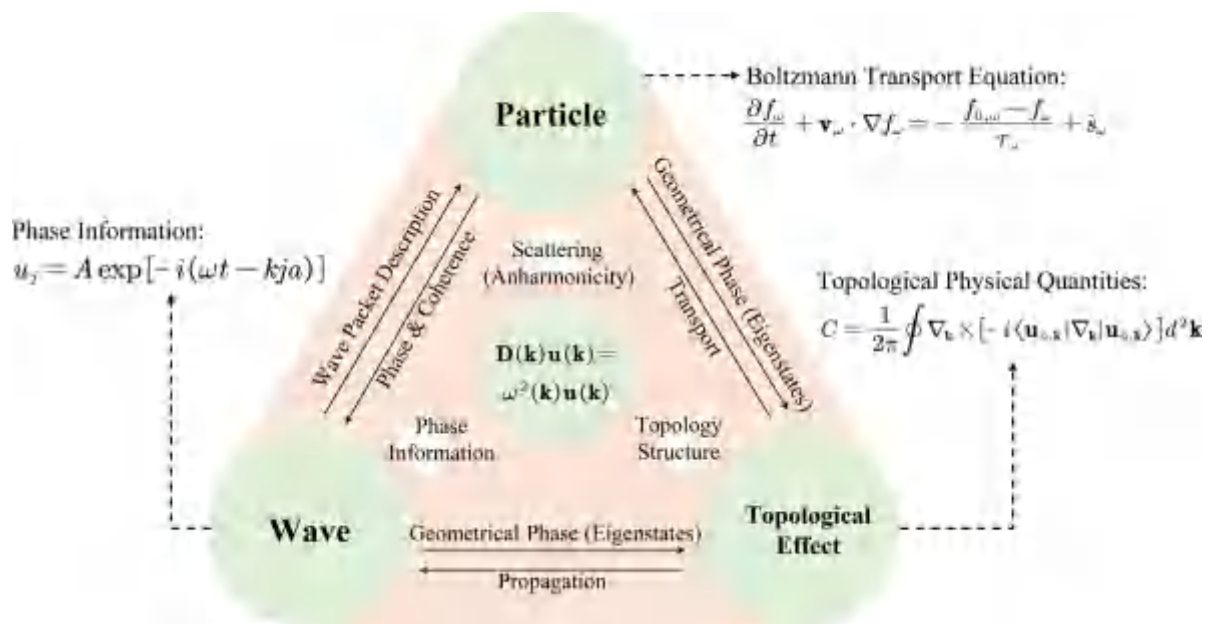
Fig. 15. Phonon physics pictures and their relations.

of phonons are separately illustrated and connected. With the understanding of phonon and phonon transport properties, various tuning methods can be proposed. Typical methods are listed in Fig. 14 and Fig. 16 and discussed in detail respectively according to their theoretical basis, as well as their applicability for GaN and GaN nanostructures in the following sections.

3.2. Tuning mechanisms and methods

3.2.1. Particle nature of phonons

Based on the thermal conductivity formula Eq. (25), tuning phonon transport can be divided into tuning phonon frequency (dispersion), phonon group velocity, and phonon scattering rate
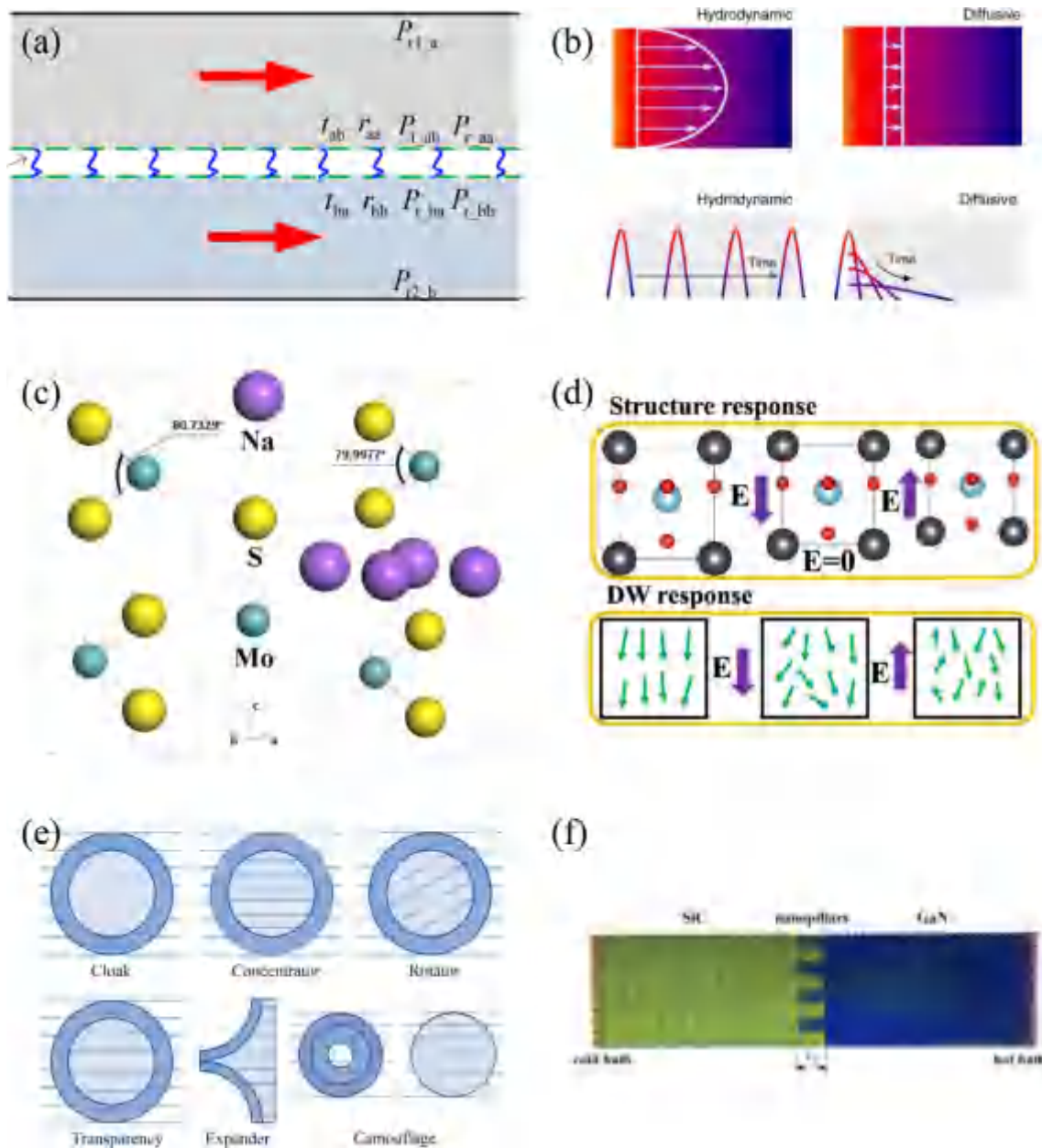
Fig. 16. Typical tuning methods based on the particle nature of phonons (a) interface tuning for in-plane thermal transport (b) ballistic-diffusive/hydrodynamic regime tuning (c) doping/inserting atoms (d) external electric field (e) thermal transformation (f) interface engineering for ITR, from [refs. 157,165,169,171,177,178].

(relaxation time). Introducing boundary scattering with nanopore and interface is the common method for nanomaterials. With nanopores or nano-meshes, lattice thermal conductivity can be tuned continuously [168]. The interface can affect phonon transmission and reflection with boundary scatterings, and conduct two-way tuning of thermal conductivity [169]. The phonon normal scattering process conserves the phonon quasi-momentum, which is generally regarded as a kind of special scattering and does not occur in real materials at ordinary temperatures. However, the phonon transport where phonon normal processes dominate has been realized in graphite with different vacancy concentrations and other three-dimensional materials at a temperature above 100 K [170–176]. Therefore, changing the heat conduction characteristic by tuning the relative strength of phonon normal scatterings becomes a possible method. Defects, including point defects and dislocation in general, can also effectively influence the phonon scatterings, which can be realized by inserting new atoms and doping [177].

Applying external fields is another kind of common method, which can comprehensively tune phonon properties, including phonon dispersion and scatterings. Stress fields, temperature fields, electric fields, and magnetic fields are several typical external fields. However, different from electrons with charges and spin, phonons cannot respond to the electric and magnetic fields directly. Specifically, external fields affect phonon properties by changing the interatomic force constants, resulting in changes in anharmonicity, lattice symmetry, and structure phase. For example, electric fields can tune phonon transport two-way by manipulating the domain wall in ferroelectric materials which can effectively control the phonon-domain wall scatterings, much similar to the directional manipulation of graphene in liquid with external electric fields [178].

Though phonon transport is in the diffusive or ballistic-diffusive regimes in most crystal materials, phonon flow can also be guided like fluids using effective structure design [165]. For example, by designing networked nano-constrictions in graphene, heat flow can be effectively manipulated, and the thermal conductivity of graphene can then vary in a large range [179]. To enhance the thermal transport in GaN and GaN HEMTs, it is required to decrease the phonon scatterings and increase the normal scatterings as much as possible. The former requires GaN materials with high crystal quality and application of external fields on GaN, while the latter requirement is still hard to be satisfied in GaN-related materials.

To now, available methods to increase the thermal transport significantly in GaN and GaN nanostructures are still rare in the framework of phonon particle nature. The phonon hydrodynamic transport regime dominated by the normal scatterings can effectively decrease the thermal resistance though, it is now only found at ultra-low or low temperatures for three-dimensional materials [170,176,180], at high temperature ($\sim$200 K) for two-dimensional materials and layered materials [171-173,175,181], *e.g.*, graphite [173,175,182], and at room temperature for one-dimensional materials [183,184]. Theoretically, specific phonon modes (*e.g.*, bending phonon modes) and a temperature window are required for hydrodynamic phonon transport in three-dimensional materials. While a simple relationship is difficult to be built between hydrodynamic phonon transport characteristics and lattice structures, searching for three-dimensional materials with hydrodynamic phonon transport at room temperature is still a big challenge. Recently, the machine learning method is adopted in this research field to search the lattice structures with phonon hydrodynamic characteristics and suggests the possible candidates diamond and BAs and their allotropes [185] which have been known the materials with ultra-high thermal conductivities and can be used as ideal substrates for GaN HEMT from heat dissipation perspective.

Currently available methods mainly refer to the tuning way by the external fields and interfacial engineering. Here, the effects of external fields (stress field and electric field) on the thermal transport in GaN are discussed, as well as the interface structure design method which is a typical method to decrease the GaN ITR. For GaN, investigations on thermal conductivity changes at stress and electric fields have been carried out recently [34,186]. The strain is applied by changing lattice constants of structure. The structure is then relaxed with the lattice constant being settled. The biaxial strain is expressed by the relative variation of the lattice constant $\sigma_a = (a - a_0)/a_0$, where the lattice constants can be referred to in Fig. 9(a). With biaxial strain, at a range of -5% to $+5\%$, changes in the lattice structure and crystal symmetry are not detected under strain states, *i.e.* GaN is still in wurtzite structure with space group P6$_3$mc. The lattice thermal conductivity changes monotonously and remarkably under strain states (Fig. 17). In specific, it decreases under the tensile strain state and increases under the compressive strain state, which is mostly attributed to the changes in phonon relaxation time based on the detailed phonon analyses. The anisotropy of lattice thermal conductivity is weak under the free state while it becomes larger under strain states. Under tensile strain state, cross-plane lattice thermal conductivity is larger than cross-plane thermal conductivity while it is opposite under compressive strain state. This difference in anisotropy, shown by different changes of squared in-plane and cross-plane group velocity, is a consequence of the weakening effect from strain-induced polarization, which screens the strain effects partially. The dimensionless cumulative thermal conductivity concerning phonon frequency in Fig. 17(d) shows that phonon frequency decreases to 6.2 THz when dimensionless cumulative thermal conductivity reaches 90% under tensile strain state, while it increases to 7.1 THz under compressive strain state. The size effect will become stronger under a compressive strain state while it weakens under a tensile strain state. In detail, the phonon free path is 3.7 μm when dimensionless cumulative thermal conductivity reaches 90% and mainly ranges from 150 to 4000 nm under a compressive strain state. Under the tensile strain state, phonon free path decreases to 1.2 μm for 90% dimensionless cumulative thermal conductivity and mainly ranges from 40 to 1500 nm.

Compared to the calculations under strain fields, calculating the responses of three-dimensional periodic lattice structures to finite electric fields from first principles is not easy work. The main difficulty is that the scalar potential "**-E·r**" (**E** is the electric field and r is the position vector) is nonperiodic and unbounded from below [187]. Under the framework of the modern theory of polarization, Souza et al. proposed an appropriate variance method based on the minimization of electric enthalpy functional [187]. Then, methods for calculating the total energy of periodic solids as well as forces and stress, Born effective charges, dielectric function, and phonon properties from first principles were proposed and implemented in first-principles calculation software. Recently, the authors performed an investigation on phonon and phonon transport properties of wurtzite GaN in the finite electric field from the perspectives of symmetry-breaking and lattice deformation using first-principles calculations [186]. The electric fields are applied along the polar axis of the GaN lattice and the lattice symmetry is conserved under this kind of electric field, while the calculations are not stable for the condition where the electric field is perpendicular to the polar axis. Lattice thermal conductivity decreases significantly at both positive and negative electric fields, with increasing anisotropy of thermal conductivity (Fig. 18). Changes in the distribution of mode phonon properties are responsible for the decrease of thermal conductivity at electric fields since no significant difference is found in phonon properties. Further quantitative analyses confirm that the change in relaxation time is the main reason for the changes in lattice thermal conductivity at electric fields, which results from the increase of the anharmonicity of interatomic interactions. Fig. 18(c) and (d) show the normalized cumulative thermal conductivity concerning phonon MFP and frequency. Maximum MFPs at free state, *i.e.*, at zero electric fields, are around 10 μm. Corresponding to the variances of lattice thermal conductivity at finite electric fields, changes in maximum phonon MFPs are, however, not large. Maximum phonon MFPs nearly keep constant for the out-of-plane condition while a slight increase occurs for the in-plane condition. Since electric fields do not significantly shift or reduce low-frequency phonon branches, maximum cut-off frequencies are nearly kept constant at electric fields. For wurtzite GaN, Quan et al. [188] also performed a systematical first-principles study on the electric field effect on thermal conductivity. While the phonon dispersion under the electric field is nearly kept constant, the thermal conductivity changes significantly. The thermal conductivity parallels to the electric field increases, with a more than 12% increase at 200 K and 8% at a higher temperature, while the thermal conductivity perpendicular to the electric field decreases by 7%, attributed to the different changes in the Ga-N bond stiffness and ionicity, and scattering rates of phonon traveling along with different directions. In their work, the condition where the electric field along the in-plane direction is also investigated, where the lattice structure is not stable and all crystal symmetries are lost, and the thermal conductivity decreases due to the accompanying increase of phonon-phonon scatterings.

Tuning the ITR is another important aspect to enhance thermal transport in near-junction electronic thermal management. Based on the current understanding of ITR as discussed above, kinds of tuning methods have been proposed to reduce the ITR. To reduce the mismatch of phonon density of states, an interlayer can be inserted as a bridge to link the two main layers, as shown in Fig. 2(c). Though thermal resistances, *i.e.*, the thermal resistances of
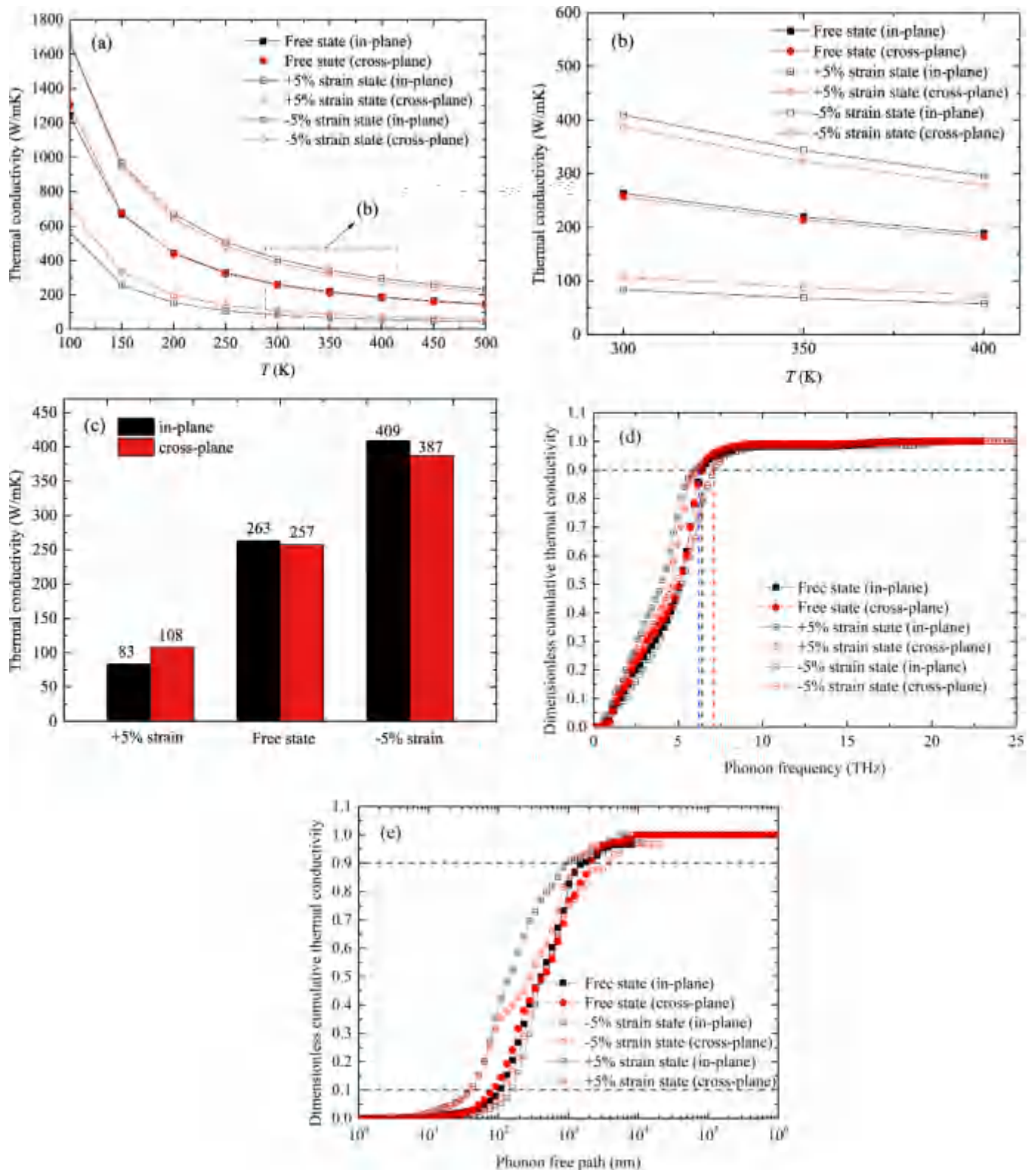
Fig. 17. Thermal conductivity of GaN concerning (a)(b)(c) temperature, (d) frequency, and (e) free path under different strain states. From [ref. 34].

interlayer and additional interface, are introduced, the total thermal resistance can decrease due to the decrease of the phonon mismatch and accompanied crystal quality improvement during grown processes, especially for layers with a large mismatch [148]. A similar method is creating a graded interface [145,189], which can effectively increase the phonon match. Chemical modification

is another effective method to weak the phonon mismatch by generating or enhancing phonon modes with a high transmission ratio [190]. Besides decreasing the phonon mismatch, enhancing the interfacial atomic interactions is another important perspective. The annealing process, as well as the self-assembly monolayers, can benefit the covalent bonding among interfacial atoms, resulting in
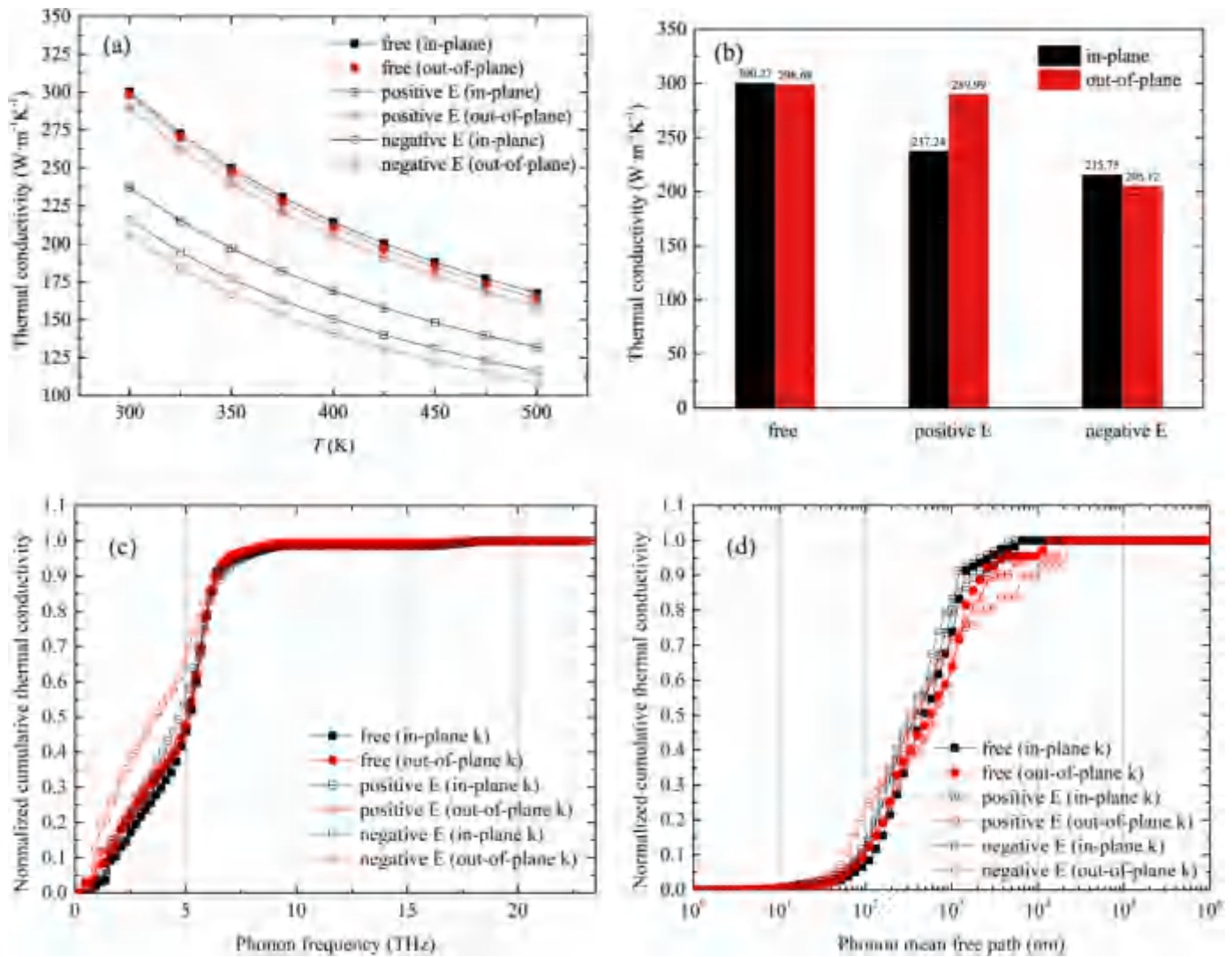
Fig. 18. Thermal conductivity of GaN concerning (a)(b) temperature, (c) frequency, and (d) free path at electric fields, from [ref. 186].

better interfacial thermal transport. Performing interface structure design could benefit the interfacial thermal conductance with the same microscopic interface morphology, *e.g.*, creating nanostructures at the interface can increase the contact region and facilitate thermal transport for smooth interface conditions [157,191]. It is noted here that the interface discussed above and in most literature is mainly referred to as the interface between channel layer GaN and substrate. For thin GaN layer conditions, treatments on the interface may cause changes in stress fields in HEMTs and further the electronic properties, which should be evaluated in advance. Theoretically, the influence factors related to the interface are intrinsic properties, while the ITR may also show size dependence at the nanoscale due to the phonon ballistic transport. An optimized thickness for both total thermal resistance from layers and interfaces is essential.

3.2.2. Wave nature of phonons

In both classical and quantum mechanical frameworks, phonons have distinct wave characteristics, *i.e.*, lattice vibrations or harmonic oscillator models. The wave nature of phonons is mainly reflected by the coupling among waves with different modes. When the characteristic wavelength of phonons is larger than the phonon MFP, the phase information of phonons cannot be ignored, and typical phenomena such as interference and diffraction can hap-

pen in phonon transport. Besides, in complex crystals such as harmonic glasses, mutual coherence among different phonon modes have to be considered where the difference between the phonon frequencies is smaller than the corresponding phonon linewidths and the velocity operator has non-negligible off-diagonal elements [192–195]. On this basis of wave nature, various tuning methods for phonon thermal transport can be put forward.

To design a superlattice structure [196–205] in which the characteristic length is comparable to the characteristic wavelength of phonons and their relation satisfies Bragg's law, interference can occur, resulting in the modification of phonon dispersions (Fig. 19(a)), *e.g.*, phonon bandgap tuning [206–208]. To impede the phonon transport effectively, alloy, doping, defects, and dislocations are usually used to increase the phonon scatterings, however, they mainly induce phonon scatterings for high-frequency phonons, while low-frequency phonons are difficult to block due to the long wavelength. Using the wave nature of phonons, resonant structures (Fig. 19(b)) in nanofilms, nanowires, nanosheets, and related structures, can be realized and effectively reduces the low-frequency phonon transport by increasing the weight phase space and providing more scattering channels for low-frequency phonons [209–211].

The methods under the bases of wave nature mentioned above are mainly used to suppress the thermal transport, and there-
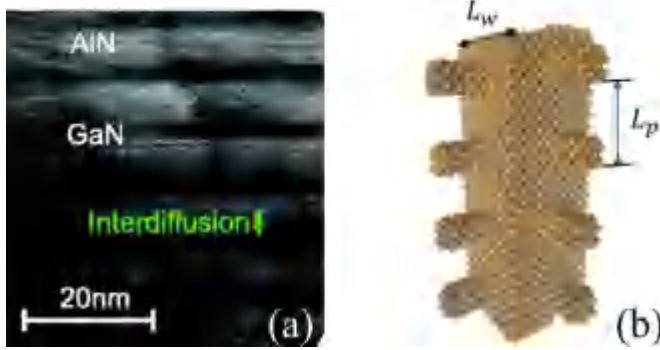
Fig. 19. Typical tuning methods for thermal transport based on the wave nature (a) superlattice from ref. [200] (b) resonance structures from [ref. 212].

fore more suitable for thermoelectric applications, instead of high-efficient thermal management. In polar materials, surface transverse optical phonons can resonate with electromagnetic waves (photons) and form the new elementary excitation, *i.e.*, the surface phonon polaritons (SPhPs)[30,215-225], which is also a reflection of wave characteristics, described by the Maxwell equation and Huangkun's equation. At this resonance, optical phonons host the frequencies and wave vectors in a similar magnitude to those of photons respectively. Typically, the SPhP has a long phonon MFP [226,227] and is promising to enhance thermal transport in systems with a large surface-to-volume ratio such as amorphous nanofilms with low thermal conductivities. When it comes to phonon transport tuning for near-junction thermal management in HEMTs, the SPhP seems to be a potential method since enhancing the surface phonon transport can be beneficial for the heat spreading in GaN HEMTs. At present, SPhP has been reported in GaN, AlN, and AlGaN thin films [214,215,217,220,222-224,228-231], as shown in Fig. 20. However, detailed thermal transport analyses for GaN with SPhP are still not reported. Special attention should be paid that external electromagnetic fields may interfere with the electron properties such as the transport of 2D electron gasses.

3.2.3. Topological nature of phonons

Stimulated by the analogy among phonon, electron, and photon, understanding of phonon transport has advanced significantly [112]. However, it is still difficult to tune phonon transport due to the lack of degree of freedom in phonon systems. Current tuning work is mainly performed based on the phonon particle nature and wave nature, as discussed above. Deepening the understanding of phonon physics and developing the new phonon degree of freedom are essential for both theoretical study on heat conduction and heat conduction tuning applications.

In this section, the topological nature of phonons is introduced and discussed, as an important part of phonon physics, side by side with the particle nature and wave nature of phonons. Topological matter theory is firstly developed in electron systems in the last century and promoted in the recent twenty years, which also shed light on photon and phonon transport tuning work. Topology is a geometrical concept, implying the invariance of a geometrical matter during continuous changes, which is a global property. In Fig. 21, the topology of a matter is described using the genus or Euler number. The band topology, *i.e.*, the topological properties of phonon/electron bands, is used to describe the geometrical characteristics of eigenstates, which include the Berry phase, Berry curvature, Chern number, *etc*. In the following six sections, topological phonon theory, topological phonon and phase transition models, phonon pseudospin, Weyl phonons in GaN, transport properties of topological states, and topological phonons beyond bulk-boundary correspondence will be discussed respectively.

i Topological phonon theory

The topological effects of phonons, as the representative for advanced phonon understanding, start from the revisit of the phonon eigenstates. With the harmonic approximation and a lattice wave solution, phonons can be described by an eigenstate problem,

$$\mathbf{D}\mathbf{u}(\mathbf{k}) = \omega^2 \mathbf{u}(\mathbf{k}) \tag{27}$$

where $\mathbf{D}$ is the dynamic matrix from the Fourier transformation of IFCs, $\mathbf{u}$ denotes the phonon eigenstate, and ω is the square root of the eigenvalue, *i.e.*, phonon frequency. Fig. 22(a) shows the phonon dispersion relations of GaN along the high symmetry paths, and Fig. 22(b) shows the atomic displacements of Ga and N atoms corresponding to four typical phonon modes at the Γ point. The displacements are represented by coordinates in three-dimensional real space and relate to eigenstates in momentum space with the Fourier transformation. In general, especially in thermal transport investigations, the phonon frequency or dispersion receives more attention since thermal transport properties will be extracted from them. Phonon eigenstates contain more information, *e.g.*, participation ratio can be deduced from them, and phonon dispersions can also be derived from them based on Green's function method. While it is well-known that topology is a geometrical quantity, *e.g.*, the object with different holes, the topology for phonons is the geometrical structure of phonon eigenstates in momentum space. Zhang et al. [166] and Liu et al. [167] independently proposed the definitions of basic topological quantities, *e.g.*, berry phase, and Chern number, and built the fundamental framework for topological phonon research, respectively. The Berry connection is defined based on the phonon eigenstates which can be easily calculated from first principles,

$$\mathbf{A}_{n,\mathbf{k}} = -i\langle \mathbf{u}_{n,\mathbf{k}} | \nabla_{\mathbf{k}} | \mathbf{u}_{n,\mathbf{k}} \rangle \tag{28}$$

The Berry curvature is defined as the curl of the Berry connection $\mathbf{\Omega}_{n,\mathbf{k}} = \nabla_{\mathbf{k}} \times \mathbf{A}_{n,\mathbf{k}}$, where n is the band index. The Berry phase can be obtained by integrating along a specific path or loop

$$\gamma_n = \int_L \mathbf{A}_{n,\mathbf{k}} \cdot d\mathbf{k} \tag{29}$$

For the Weyl phonons in a three-dimensional lattice, the topological invariant is the Chern number, which is defined in the closed surface containing the nontrivial Weyl point in momentum space,

$$C = \frac{1}{2\pi} \oint \Omega_{n,\mathbf{k}} d^2\mathbf{k}. \tag{30}$$

Now, with the analogy between phonon and electron, diverse topological phonon states have been predicted and found in lattice models and real materials, including phonon topological insulator state [232,233], phonon (gapless) semi-metal states (Dirac, Weyl, nodal line, nexus) [234–242], phonon valley states [158,243-246], high-order topological phonon states [247–251], and topological phonon states in quasi-crystal, amorphous solids, and crystals with topological defects [211,251-253]. Phenomenologically, a nontrivial topological state implies a pair or more anomalous band sequence reflected by the compatibility between two different momentums. At the surface (a general interface between material and vacuum) and the interface between trivial and nontrivial materials, phonon bands will change from a nontrivial sequence to a trivial one, which results in the representative character of the topological phonon state, *i.e.*, bulk-boundary correspondence. For example, at the boundary of a 2D lattice with a phonon topological insulator state, there are non-dissipative boundary states with pseudospin-momentum binding. In determining the topology of phonon bands, lattice symmetry and interatomic force constants play an important role. In classical phonon transport studies, lattice symmetry
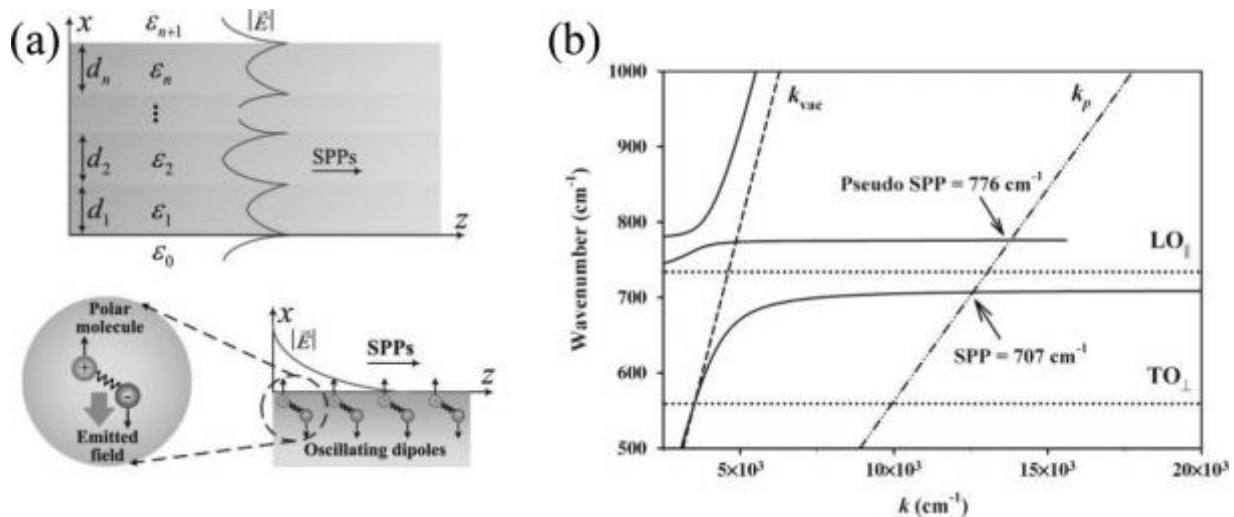
Fig. 20. Schematic of (a) surface phonon polariton from ref. [213] and (b) its dispersion relations in GaN from [ref. 214].
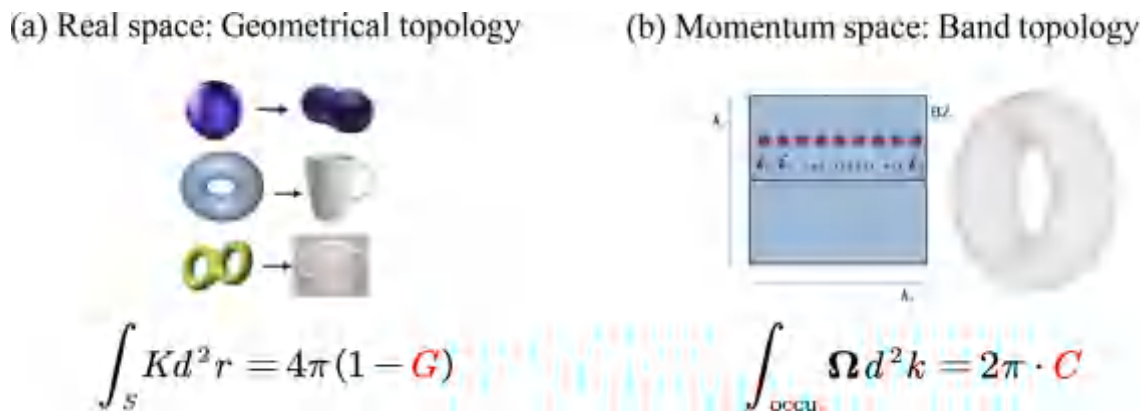
Fig. 21. Schematics of the topology and topological physics. (a) Geometrical topology is expressed as genus (G) and defined by the Gauss curvature (K). (b) Band topology is expressed as the Chern number (C) and defined by the Berry curvature (Ω) in the Brillouin zone.
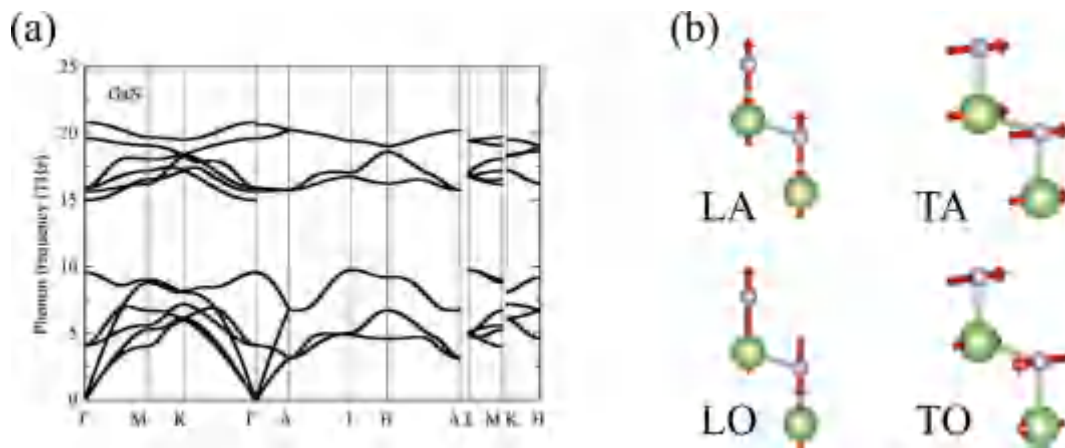
Fig. 22. (a) Phonon dispersion relations (eigenvalues) and (b) atomic displacements (eigenstates) concerning different phonon modes at Γ point for wurtzite GaN.

is used to analyze the phonon scattering channel and simplify the IFCs calculations, while it is mainly used to determine the phonon degeneracy and classify the phonon branch in the perspective of topological phonons. The pseudospin can be created by adopting the lattice symmetry while no intrinsic spin exists in the phonon system, called chirality of phonons [243,254], which will be introduced in detail later. IFC is the other important factor as it determines the phonon band details according to the dynamic matrix

in the phonon eigenstate equation. Besides the topological phonon theory, finding real materials with nontrivial topological phonon states is another central issue. Currently, many topological semimetal phonon states have been uncovered in different real crystals [234–241,249,255–257], such as graphene and silicon [242,257]. A phonon database especially for the Weyl point and the nodal point has been built to now [256].

i Models for the topological phonon and phonon phase transition
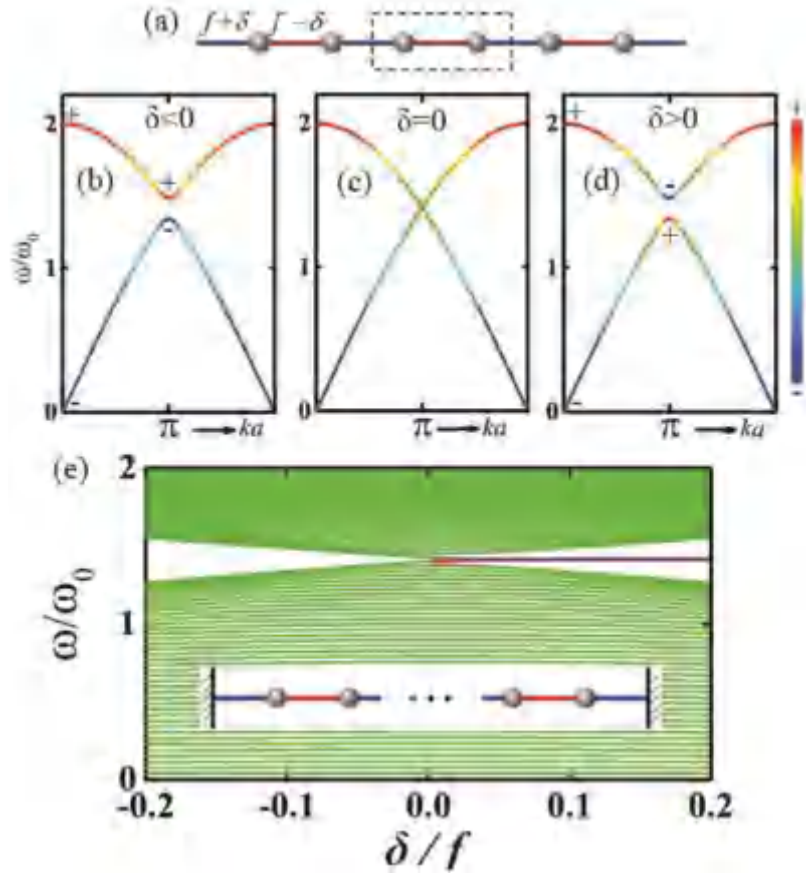
Fig. 23. (a) A one-dimensional diatomic chain model, (b-d) phonon dispersions in cases with different force constants, and (e) phonon dispersion of finite atomic chain with fixed boundaries from [ref. 258].

Since the topology of the phonon band defines the topological trivial and nontrivial phonon band, which cannot turn into each other with adiabatic change (the order of phonon bands doesn't change during this kind of process), the topological phonon phase transition should exist. The topological phonon and topological phonon phase transition can be described simply by a one-dimensional diatomic chain model, as shown in Fig. 23. The primitive unit cell in this atomic chain consists of two atoms with mass m_1 and m_2. The harmonic approximation is adopted for interatomic interaction and only nearest-neighbor interaction is considered. The intracell force constant is $k_1=f-\delta$, and the intercell one is $k_2=f+\delta$. Then, the lattice wave solution can be derived, and the frequency results are shown in Fig. 23(b-d). When γ is equal to zero, there is no bandgap in phonon dispersions, while the bandgap exists in cases $\gamma=-0.2$ and 0.2 (γ is defined as $\gamma=(k_1-k_2)/(k_1+k_2)$). The bandgaps in both cases are the same, however, they host different topological phonon properties. The topological quantity defined in this system is Berry/Zak's phase

$$\theta = \frac{1}{2}\text{Im}\int_{-\pi/a}^{\pi/a}\frac{\partial_q z}{z}dq, \tag{31}$$

which is equal to π when $\gamma>0$ and equal to 0 when $\gamma<0$ [258]. In Eq. (31), z is defined as $z = k_1+k_2\exp(iqa)$ based on wave vector q and lattice constant a. For the case $\gamma>0$, the phonon bands are topological non-trivial, and the corresponding finite atomic chain hosts the nontrivial edge phonon states, as shown in Fig. 23(e). Liu et al. [233] generalized this model to three-dimensional triangular/tetragonal/hexagonal simple lattice systems and proposed the topological phase transition of topological phonon insulator states based on the effective Hamiltonian modeling.

At present, several kinds of topological phonon states have been reported based on theoretical modeling and calculations, *e.g.*, topological insulator phonon state, Dirac phonon state, Weyl phonon state, nodal line (ring) phonon state, and topological triple-point phonon state. In general, these topological phonon states are proposed based on the analogy with the topological states in electron systems including topological insulator sand semi-metal states. The significant characteristic of the topological states is bulk-boundary correspondence, *i.e.*, a bulk system with nontrivial topological properties corresponding to a nontrivial topological surface state. To identify topological phonon states in a specific lattice system, we can first calculate the topological relevant quantities of the bulk system, *i.e.* Berry phase, Berry curvature, Chern number, and Wannier charge evolutions. Then surface states and projections of the isofrequency plane on surfaces can be further calculated to confirm the topological properties at points with nontrivial topological relevant quantities. Detailed characteristics differ for different topological phonon states. For the topological phonon states mentioned above, topological insulator phonon states require a couple of double-degenerate phonon bands at a specific point in the Brillouin zone, and band inversion between the phonon bands (band inversion can be checked based on symmetry analyses at different high symmetry points). This kind of state is difficult to realize in real three-dimensional materials as symmetry requirements for both bulk systems and surface systems are strict. Dirac phonon can be regarded as the transition state from a trivial insulator phonon state to a topological insulator phonon state. For the topological insulator phonon state, an obvious bandgap exists at this point while it is gapless in the surface Brillouin zone, very similar to that in electron systems. Topological insulator phonon states in
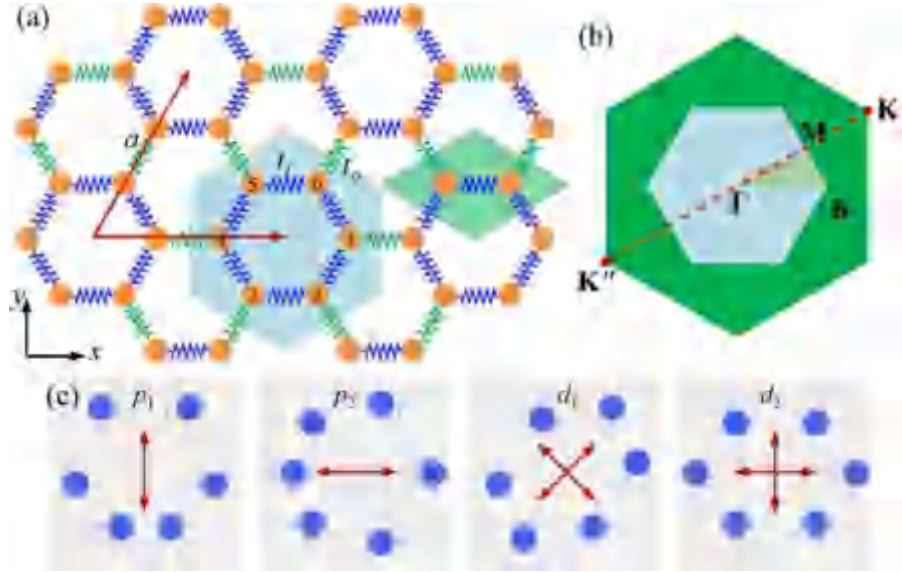
Fig. 24. Schematics of pseudospin in two-dimensional hexagon lattice (a) Supercell composed of 6 atoms; (b) the Brillouin zone; (c) The *p* and *d* states at Γ; Solid blue circle denotes the location of maximal vibration; the hollow circle indicates equilibrium position. From [Ref. 260]. (For interpretation of the references to colour in this figure legend, the reader is referred to the web version of this article.)

three-dimensional lattices are complex as topological invariants to distinguish topological states are hard to define. Thus, band inversion analyses and surface state calculations are common to identify topological insulator phonon states. For the Weyl phonon state, it is a nontrivial double degenerate phonon band crossing point with a non-zero Chern number. The projection of the isofrequency plane at this point on the surface is an open arc. Nodal line states are nontrivial double degenerate phonon bands, which can be identified by calculating the Berry phase (0 for trivial and $n\pi$ for nontrivial, in which *n* is an integer). Topological effects of phonons affect phonon transport by inducing topological surface phonon states with novel transport characteristics that are robust and protected by the topological properties of the bulk system. Since Weyl phonon surface states are present in the gaps of trivial surface states, which can be regarded as isolated and bound states, and only half of the nontrivial states exist on opposite surfaces (arc states), scatterings of topological surface phonon states promise to be reduced significantly, especially backscattering.

i Phonon pseudospin and angular momentum

Most of the phonon topological theories and models are developed from analogy analyses of phonons and electrons. In the phonon-electron analogy, phonon does not host the similar characteristic spin 1/2, and thus the theory for the quantum spin Hall effect cannot be directly applied in phonon systems. However, the development of the topological crystalline insulator inspired the application of crystal lattice symmetry in the topological phase. For phonon systems, in the lattice, double degeneracy and multiple degeneracies can be realized due to the existence of the lattice symmetry, which forms the basis to create pseudospin. An example of a two-dimensional hexagonal lattice is shown here to illustrate the picture of phonon pseudospin. In this lattice (Fig. 24), only two-dimensional motion is considered. Each unit cell consists of six atoms. The unit cell degenerates into the primitive unit cell consisting of two atoms when the interatomic force constants are the same. In this case, double degenerate Dirac type phonon dispersions are present in K and K′ momentums in reciprocal space. By performing band folding, the Dirac points in K and K′ can be folded into Γ points, and the double Dirac points can be then created (Fig. 25). The double degenerate Dirac points consist of the

band 5 to 8, which are p_1, p_2, d_1, and d_2 states. The *p* states are anti-inverse symmetric, while the *d* states are inverse symmetric, very similar to the *p* and *d* orbitals in electron bands. These two types of bands are both linearly polarized. The degeneracy of these bands is protected by the six rotational symmetry (C6v). For these degenerate eigenstates, the pseudospin and corresponding operators can be created,

$$T' = i\sigma_z K, \quad p^{\pm} = \frac{p_1 + ip_2}{\sqrt{2}}, \quad d^{\pm} = \frac{d_1 + id_2}{\sqrt{2}}. \tag{32}$$

where +/- indicates the pseudospin up and down. Although *p* and *d* states are linearly polarized, the created pseudospins, which can be understood as the mixed states, are circular polarized. With the operation above, the bases to realize the phonon version of quantum spin Hall effect has been built, where the physical quantity for this spin system is spin Chern number, like that in electron systems.

From classical perspectives, phonon branches are usually divided into LA, LO, TO, and TA branches. However, these branches can be divided distinctly only at specific points, such as the Brillouin center and some high symmetry paths, while they are mixed states at other points. The phonon branches hosting the distinct polarizations are known to be linearly polarized without circular polarization. Zhang et al. [166] defined the phonon angular momentum and phonon circular polarization firstly and explained the picture of phonon circular polarization strength, *i.e.*, the phonon angular momentum. Derivations show that the phonon circular polarization has a similar expression with the phonon angular momentum, confirming that it can be interpreted as the phonon angular momentum. The phonon angular momentum is defined as the cross product of atom displacement and its velocity [259],

$$\mathbf{J}_{ph} = \sum_{l\alpha} \mathbf{u}_{l\alpha} \times \dot{\mathbf{u}}_{l\alpha}, \tag{33}$$

where *l* and α are the indexes for unit-cell and atoms, much similar to the angular momentum definition of the rigid body. At equilibrium states, the phonon angular momentum along the *z*-
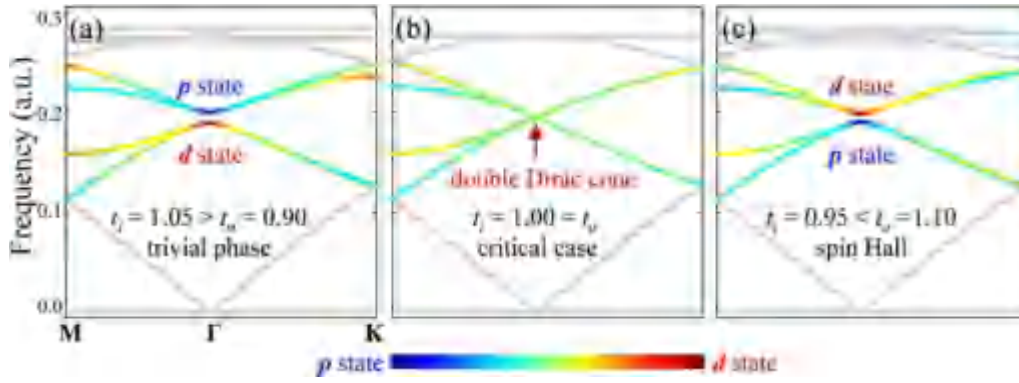
Fig. 25. Schematics of the quantum spin Hall-like phase transition: (a-c) Band structures for trivial insulator, critical case, and spin Hall insulator, respectively; Rainbow color indicates hybridization of the states. From [Ref. 260].

direction for each phonon mode is

$$
l^z_{\mathbf{k},\sigma} = \left(\mathcal{E}^\dagger_{\mathbf{k},\sigma} M \mathcal{E}_{\mathbf{k},\sigma} \right) \hbar,
$$
$$
M = \begin{pmatrix} 0 & -i \\ i & 0 \end{pmatrix} \otimes I_{n \times n}. \tag{34}
$$

where $\mathbf{k}$ and σ represent the phonon wave vector and branch, respectively, and ε is the corresponding displacement polarization vector. Following the expression methods for photon polarization, phonon circular polarization (*e.g.*, along the z-direction) can also be defined, which is [243,245]

$$
S^z_{ph} = \mathcal{E}^\dagger \hat{S}^z \mathcal{E} \hbar,
$$
$$
\hat{S}^z = \sum_{j=1}^n \left(\left| R_j R_j \right| - \left| L_j L_j \right| \right) = \begin{pmatrix} 0 & -i \\ i & 0 \end{pmatrix} \otimes I_{n \times n} \tag{35}
$$

where n denotes the atom number in each unit cell. $|R_j\rangle$ and $|L_j\rangle$ are the basis vectors representing the right and left rotations of the lattice along the z-direction. In principle, phonon circular polarization is the same concept as phonon angular momentum.

i Weyl phonon and phase transition in GaN systems

When we plan to perform phonon transport tuning, a critical question is raised that how we use the topological effects of phonons in GaN HEMTs thermal design. With thermal analyses in the GaN HEMT, it is known that thermal spreading from the hot spot to the planary GaN layer dominates the near-junction heat conduction process, and then decreasing the thermal resistance becomes the tuning object. Since topological nontrivial phonon systems hold the surface and interfacial phonon modes with extraordinary topology-protected transport properties, such as non-dissipative one-way transport and one-way transport without backscattering immune to defects and disorders. The thermal spreading resistance would significantly decrease if a non-dissipated one-way phonon transport can be realized at the Al-GaN/GaN interface. Current reports on non-dissipative one-way transport and transport without backscattering are mainly about photon and phononic crystals, phonon systems in two-dimensional materials, and simple lattice models. For near-junction thermal management in GaN HEMTs, the important problem to be solved is how to realize topological phonon phase transition in real materials, especially GaN, if GaN is a trivial phonon system. In this section, the Weyl phonon and its topological phase transition in the AlGaN system are introduced in detail. Besides its extraordinary transport properties, an apparent advantage for topological effects of phonons in tuning phonon transport is that it is intrinsic properties that are expected no negative impact on electron properties.

Recently, the authors performed systematical analyses on the topological effects of phonons in wurtzite GaN with the aid of first-

principle calculations and topological phonon theory by concentrating on Weyl point states and discussing the topological phonon phase transition in generalized GaN systems by introducing Al atoms, including AlN and AlGaN [241]. It is found that wurtzite GaN is a trivial topological phonon system where no topological insulator phonon state and Weyl phonon state are found. However, by introducing Al atoms, Weyl phonon states are found in AlN and AlGaN of different structures, and they can be regarded as a topological phonon phase transition in AlGaN systems. By calculating topological charges, Wannier charge center evolutions, Berry curvature distributions, the projection of isofrequency plane on the surface, and surface local density of states, two kinds of single Weyl phonon states in AlN, two kinds of single Weyl phonon states in $AlGaN_2$ with space group P3m1, and one single Weyl phonon state in cubic Al_3GaN_4 are confirmed. Here, in Fig. 26 and Fig. 27, the surface states of Weyl phonons in wurtzite AlN and $AlGaN_2$ are present, where the surface arcs illustrate the characteristics of Weyl phonons. As typical materials in AlGaN/GaN heterostructures, wurtzite AlN and $AlGaN_2$ with space group P3m1 promise to host topological surface states without backscattering as they are confirmed to be topological phonon nontrivial systems with open Weyl surface arcs. Future research could directly examine these surface/interface states and the scattering characteristics between topological surface phonon states and trivial surface phonon states by molecular dynamic simulations. While AlN's thermal conductivity is relatively high, the contribution from topological surface phonon states may be insignificant. However, as mentioned in the first section of this work, interfacial thermal transport parallel to the AlGaN/GaN interface is critical for the spreading of heat generated from the near junction region. Hence, through effective design, the excellent transport properties of Weyl phonon states promise to improve thermal management in information and power electronics.

In practical applications for GaN HEMT, the basic structures are AlGaN/GaN heterostructure and GaN on the substrate. Consequently, interfacial phonon states beyond surface phonon states should be further studied, where the lattice mismatch and the topological phonon properties in each layer are both important. As discussed above, though topological insulator phonon states are still not reported in real materials, topological non-metal phonon states including Dirac phonon, Weyl phonon, triple degenerate phonon, nodal-line (ring) phonon, and new topological phonon beyond simple electron correspondence have been reported successively [232,237,241,242,245,246,256-258,261], providing rich research systems for the thermal transport in GaN structures. It is noted that a very recent calculation work has reported the planar nodal chain phonons in wurtzite GaN protected by the mirror symmetry (for constitution of the nodal rings), as well as the combi-
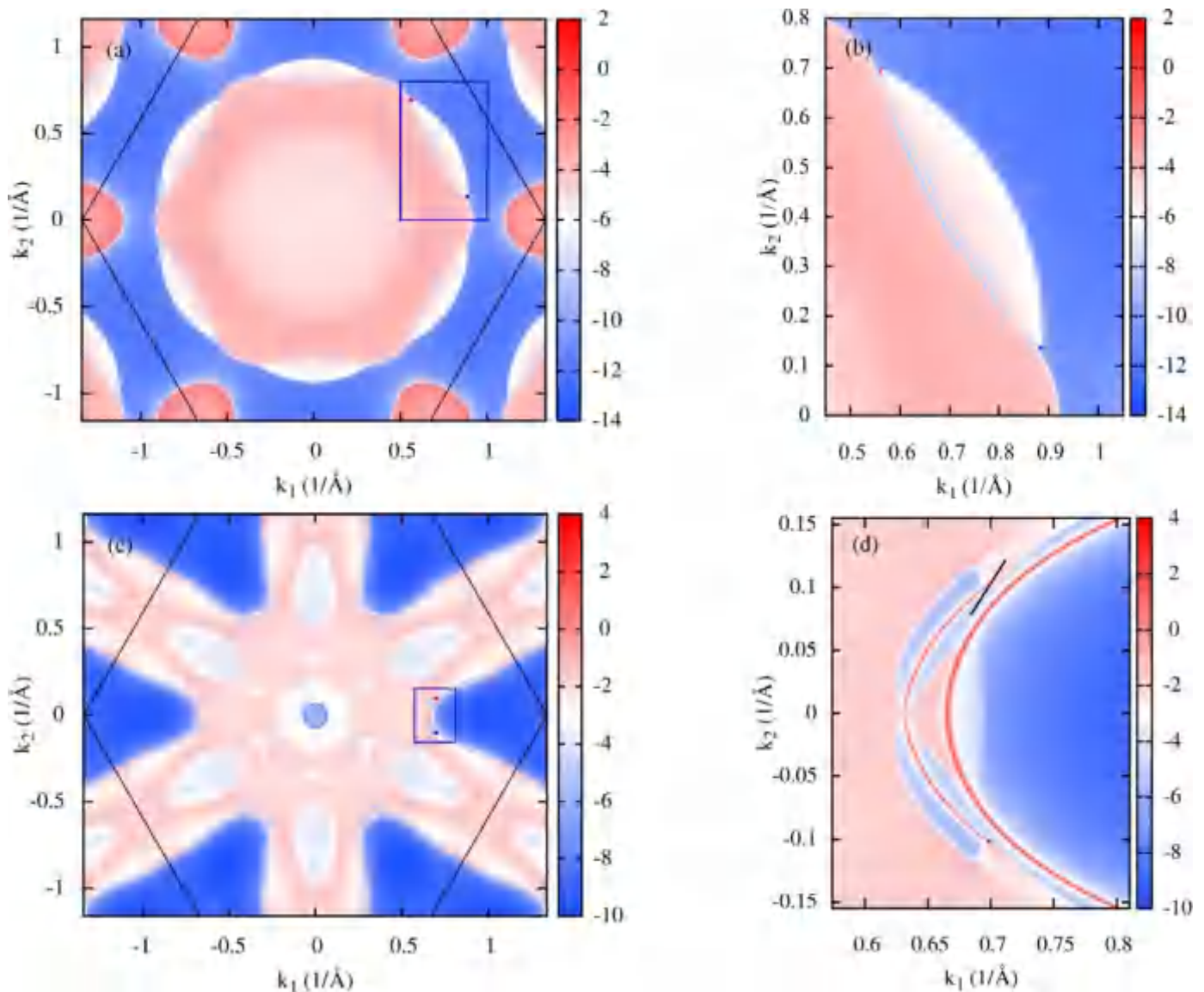
Fig. 26. Weyl surface arcs in AlN. The projection of the isofrequency plane of surface states on the (0001) surface Brillouin zone at a frequency equal to (a) 12.23 THz and (b)19.57 THz. The red and blue dots represent Weyl points with positive chirality 1 and negative chirality −1, respectively, which are linked by phonon surface arcs. The black hexagon indicates the surface Brillouin zone of the (0001) surface in wurtzite AlN. (b) and (d) are enlarged views of the zones encircled by blue rectangles in (a) and (c), respectively. From [ref. 241]. (For interpretation of the references to colour in this figure legend, the reader is referred to the web version of this article.)

nation of time reversal and non-symmorphic two-fold screw symmetry (for the intersection between nodal rings), which provides more possibility in phonon transport tuning in GaN systems [262].

i Transport properties of topological phonons

The topological non-trivial lattice systems with open boundaries (atom chains, nanoribbons, nanofilms, *etc.*) hold topology-protected boundary states with unique transport properties, *i.e.*, bulk-boundary correspondence, which is the attractive part of topological physics concerning practical applications. Fig. 28 show this extraordinary low-dissipative transport property in acoustic topological insulators and topological nontrivial BN/NB lattices with phonon valley Hall effect. The boundary is the transition area that links the topological trivial part and the non-trivial part. Consequently, the boundary state is in the transition phase. Under the framework of topological band theory, changes in topological properties are mainly reflected by the relation changes among bands, *i.e.*, the close and opening of the bandgap. For example, the bandgap closes at the boundary while the corresponding bulk

bandgap is finite in topological insulators. Due to the topological protection, the boundary states are robust, immune to the perturbation from atomic defects, vacancies, and disorders, depending on the topological types, particle properties, and system dimensions, *etc.*, specifically.

The well-known topological boundary state is the boundary state in the quantum Hall effect (Chern insulator) holding a one-way non-dissipative transport property [264,265]. In specific, the electrons with positive and negative group velocities are divided due to the strong magnetic field (time-reversal symmetry breaking in general). Therefore, the scatterings of boundary states are forbidden, leading to non-dissipative transport. For the quantum spin Hall effect where time-reversal symmetry is conserved without a strong magnetic field, the boundary states can also hold one-way non-dissipative transport properties, though these boundary states are spin-polarized instead of the net one-way transport, protected by the quantum interference rule[266]. In photonic and phononic crystals, similar quantum Hall states can be realized by introducing external mechanisms of action to break the time-
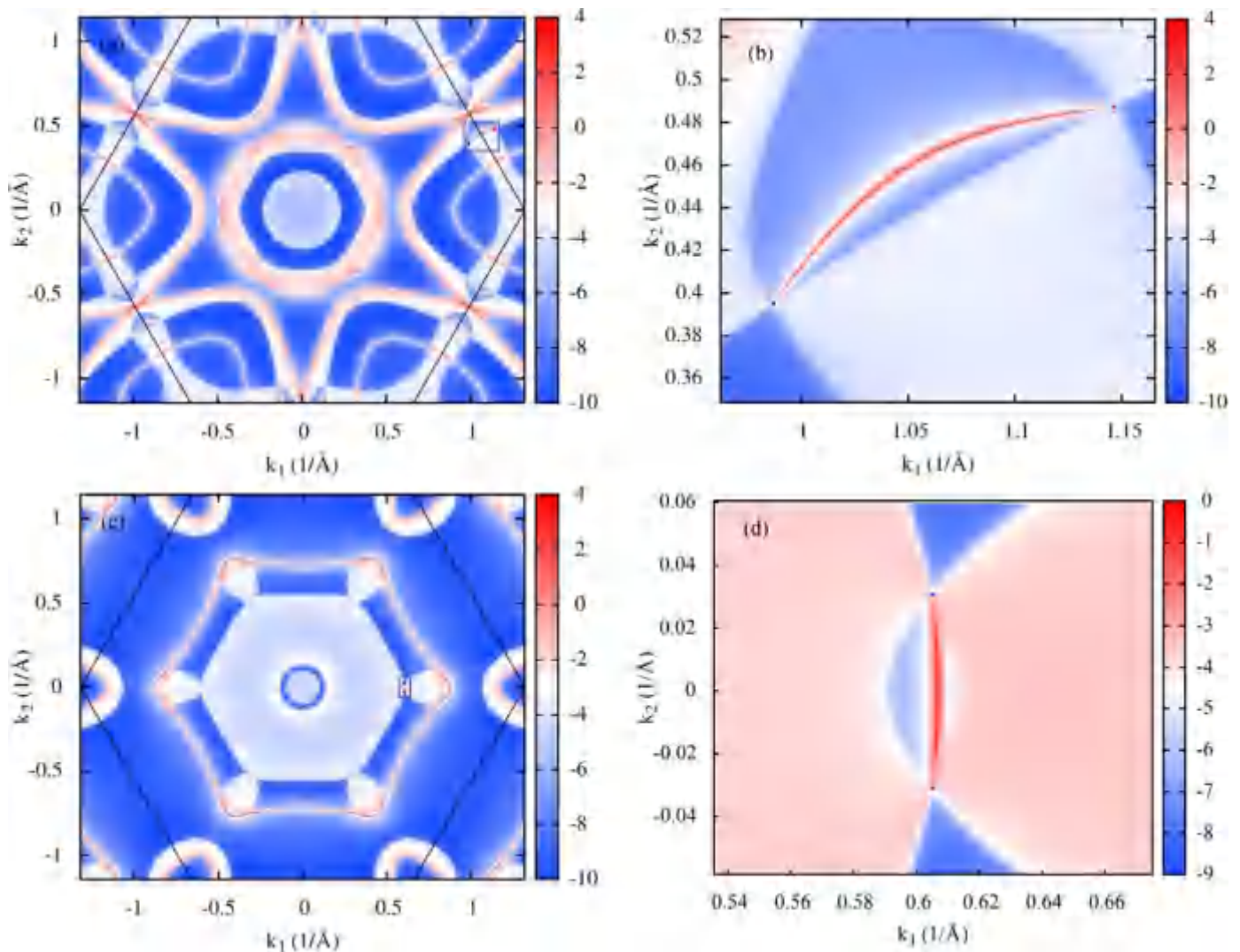
Fig. 27. Weyl surface arcs in AlGaN$_2$. The projection of the isofrequency plane of surface states on the (0001) surface at the frequency (a) 17.41 THz and (b) 18.79 THz. The red and blue dots represent Weyl points with positive chirality 1 and negative chirality −1, respectively, which are connected by a phonon surface arc. The black hexagon indicates the surface Brillouin zone of the (0001) surface in wurtzite AlGaN$_2$. (b) and (d) are enlarged views of the zones encircled by blue rectangles in (a) and (c), respectively. From [ref. 241]. (For interpretation of the references to colour in this figure legend, the reader is referred to the web version of this article.)

reversal symmetry, such as Gyro inertial effect[267,268]. Besides, similar quantum spin Hall states are created with the aid of pseudospin physics in systems with time-reversal symmetry, leading to pseudospin-momentum locked one-way non-dissipative transport boundary states. Currently, valley Hall states, semi-metal states have been reported from theoretical analyses and confirmed by the experiments. The one-way non-dissipative transport properties are illustrated by the group velocity results from both calculations and experiments[240,246,263,268].

In phonon systems, phonon interfacial transport is a longstanding topic of concern. However, researchers mainly focus on the phonon transport across the interface, instead of the transport along with the interface, while the latter is the characteristic of topological phonon boundary states. At present, the understanding of transport properties of topological phonon boundary states is mainly from the analogy between phonons and other particles (electrons and photons). For phonon systems with nontrivial topological properties, the corresponding surface states are topology-protected bounded states, immune to the surface atomic disorder and defects. For two-dimensional topological phonon insulators, the boundary states host one-way non-dissipative transport prop-

erty, while their transport is backscattering forbidden for three-dimensional topological phonon insulators and Weyl phonons. However, the analogy analyses are not enough to provide a comprehensive picture of the transport of topological phonon boundary states, e.g., the one-way group velocity results only cannot confirm the one-way transport of topological boundary states in Weyl phonon systems. In phonon systems, a very important factor that will significantly influence phonon transport is the phonon anharmonicity or phonon scattering processes. To the best of our knowledge, research on topological phonon transport is rare. In ref. [246], the authors simulated the valley Hall phonon transport in the 2D BN lattice, where they confirmed the low-dissipative transport properties of the valley Hall boundary states using the wave packet and molecular dynamics simulations. This work mentioned that the topological nontrivial boundary states are isolated from the other phonon mode and therefore host a low scattering rate. However, a systematic analysis and physical picture of the unique transport properties are still required. For 3d semiconductors, the surface and interface are 2d, and possess much more phonon modes compared to the 1d boundaries, leading to more possible phonon scattering space. The most important is the
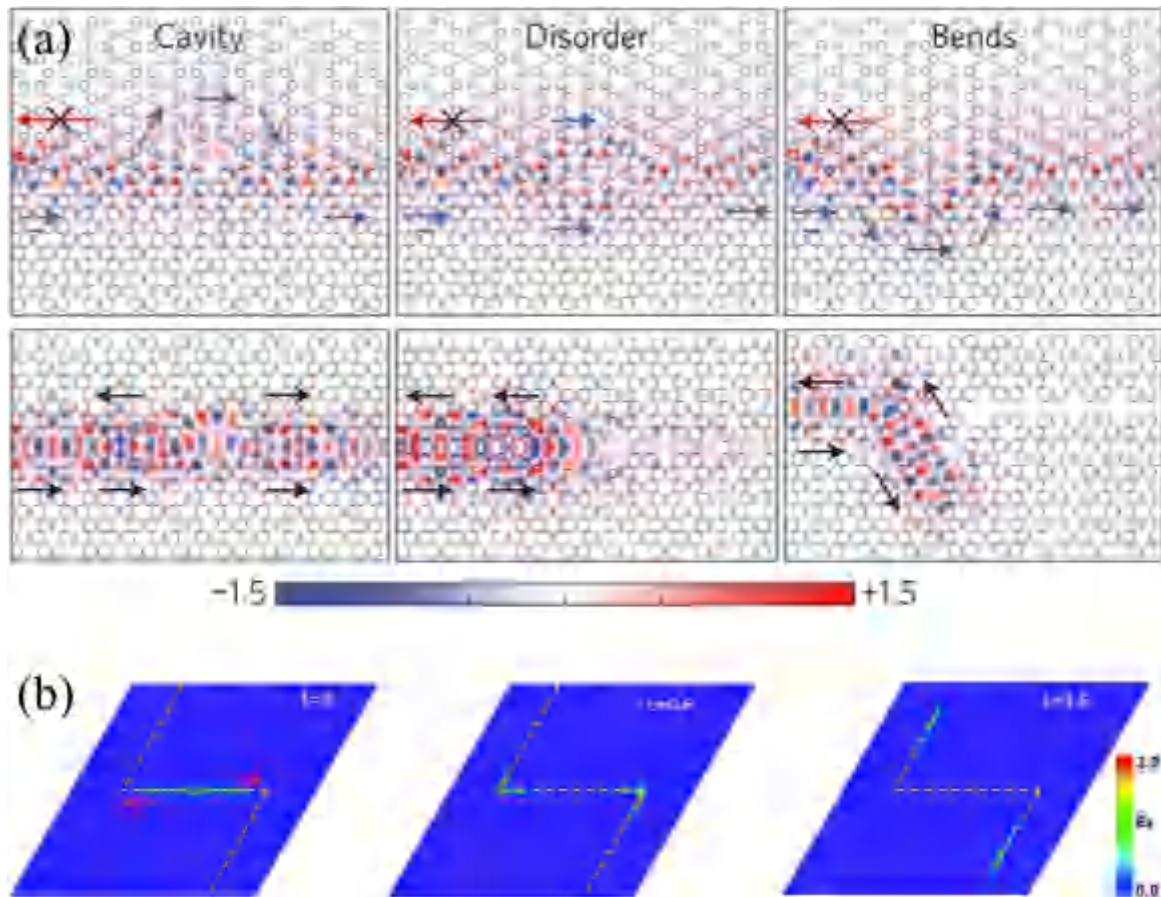
Fig. 28. Schematics of the one-way non-dissipative transport of topology-protected boundary states in (a) topological acoustic insulators and (b) topological nontrivial BN/BN lattice with valley Hall phonon states. The topological boundary states are robust and immune to the cavity, local disorder, and bends. From [refs. 263] and [246].
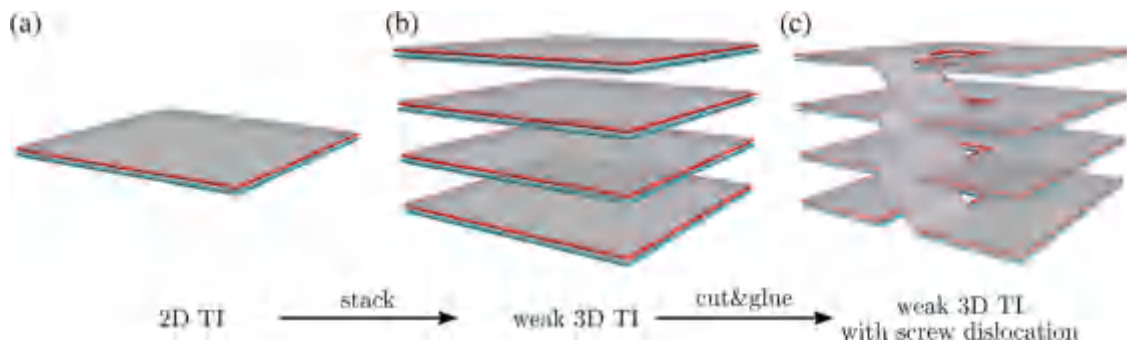
Fig. 29. Schematic of screw dislocation induced helical modes in a 3D weak acoustics topological insulator, from ref. [211].

physical relation between the phonon transport and bulk phonon topology considering the phonon anharmonicity. Besides, at the interface in AlGaN/GaN heterostructures, not only phonon transport but also the electron dissipation process plays a significant role in thermal transport. Phonons can be scattered by electrons including the absorbing and emitting processes. Hence, the EPC property of topology-protected boundary phonon states is promising to affect the electron-phonon coupled transport.

i Topological phonons beyond bulk-boundary correspondence

While topological matter physics is currently known for its bulk-boundary correspondence, recent investigations expanded this understanding, *i.e.*, the bulk-dislocation correspondence was proposed in topological insulators and acoustic topological insulators [211,252,269,270]. Thus, the one-way non-dissipative transport is promising to occur not only at the interface but also along the dislocation lines (Fig. 29). The topological invariant for dislocation-induced topological states is defined based on the Burger vector of the dislocation and the reciprocal vector for topological insulator $B \cdot G_\nu / 2\pi$, where the G_ν is defined as the multiple of weak topological indices and primitive reciprocal vector [211]. Due to the lattice mismatch between layers during the material growth, dislocations widely exist in GaN films as one of the most important factors suppressing the thermal transport in GaN. Therefore, it will be of significance for tuning phonon transport if the bulk-dislocation correspondence can be created in GaN systems. Actually, with the development of band topology, the research on relations between band topology and lattice defects [261,271-274] as well as local disorders [251,275-278] and domain walls has become the new interest, which brings more opportunities for phonon thermal trans-

port physics study and thermal transport tuning in semiconductors.

4. Conclusions and perspectives

Phonon transport property and its tuning mechanisms is a topic of long-term concern in heat conduction research. Towards the background of heat dissipation issues in wide bandgap semiconductor GaN power electronics, the purposes of systematical heat conduction analyses are straightforward, *i.e.*, predicting and optimizing the heat conduction processes in the near-junction region. While the former mainly depends on the progress of the calculation methods, the latter raises a higher requirement for an understanding of phonon physics. In this review, problems and progresses in phonon thermal transport in GaN and GaN HEMT structures are systematically reviewed, following the heat flow path, from heat generation at the interface to heat conduction across the channel layers and interfaces. Phonon transport tuning methods are discussed and classified into three categories corresponding to particle nature, wave nature, and topological nature, respectively. Here, some promising contents worth further investigation are highlighted:

1) While the phonon transport properties of pure GaN crystal have been studied comprehensively from first principles, those in GaN nanostructures with defects and interfaces are still not fully understood, which requires more investigations by simulations and experimental measurements. However, a large simulation system is needed to model GaN nanostructures and GaN lattices with dislocations and defects, making it difficult to perform first-principles calculations directly. Currently, though Green's function method based on the first-principles calculations provides the possibility to dig out details of phonon scatterings by dislocations, defects, and interface, many theoretical approximations must be adopted due to the limitation in calculations. As a bridge between the first-principles calculations and mesoscopic simulations, the molecular dynamics simulation method is promising to play a more important role in comprehensively understanding the phonon transport in GaN nanostructures with dislocations and defects, especially that the development of machine-learning-based potential functions makes up one of the biggest shortcomings of the MD method. For experimental studies, more effective experimental thermal conductivity data of GaN crystals and films are required, where the "effective" mainly refers to that the GaN samples used in measurements should be systematically characterized, including the thickness, dislocation density, defects types/density, crystal orientation, surface morphology, strain states, *etc.* At present, the lack of key information about GaN samples hinders the analyses of thermal conductivity data.

2) Understanding and modeling the phonon transport at the interface in AlGaN/GaN heterostructure are important for near-junction thermal management, which is however very complex as discussed in Section 2. The heat conduction process is not just showing nonequilibrium in phonon systems but is also coupled to the heat generation process where electron transport and scatterings must be solved. Hybrid electron and phonon transport simulations provide the possible solution to fully analyze these coupled processes. Since band model and scattering models for electrons and phonons will be used in simulations, the accuracy should be further examined by the experimental measurements, where the quantity to be measured for AlGaN/GaN heterostructure is the surface temperature distribution. Besides, the transient processes including heat generation and phonon transport require more studies to understand the electrothermal responses at time-varying work

conditions. To sum up, the phonon transport at the interface should be investigated by combining the multiscale thermal simulations and the experimental measurements, where the simulation results guide the experimental design and measurement results are used to invert the phonon properties in simulations.

3) There is still no satisfactory method to enhance the phonon thermal transport in GaN or GaN nanostructure in HEMTs till now. Exploring the new phonon physics is promising to be a valuable research topic for the generation of new tuning methods. The topological effects of phonons represent the recently advanced understanding of phonon physics, which inspires many new tuning methods in phonon transport. Also, the topological phonon effects can be found in topological defect lines (*e.g.*, dislocation lines) and amorphous solids, which provides more opportunities for GaN and GaN-related crystals and alloys. Specifically, as the Weyl phonons have been reported in GaN systems (AlN and AlGaN), the topological phonon phase transition in GaN and other important wide bandgap semiconductors is critical for the further applications of topological effects in thermal transport. While the effective Hamiltonian model can be built with the aid of the $k \cdot p$ perturbation method and the group theory, an effective model for the interatomic interaction model of GaN is essentially required to establish the relationship between the interatomic interaction and the topological phonon properties, which is the key to explain and realize the topological phonon phase transition. Investigation of thermal transport properties of topological phonon surface and interface states is the most important part of applications. Since interatomic force constants in real crystal lattices are not as simple as the model with the only quadratic term, the cubic term, *i.e.* the an-harmonic interactions, will also play an important role in transport by inducing scatterings, making the phonon transport near the surface and interface more complex than classical wave propagation and photon transport.

Declaration of Competing Interest

The authors declare that they have no known competing financial interests or personal relationships that could have appeared to influence the work reported in this paper.

Data availability

No data was used for the research described in the article.

Acknowledgments

References

[1] H. Amano, Y. Baines, E. Beam, et al., The 2018 GaN power electronics roadmap, J. Phys. D: Appl. Phys. 51 (16) (2018) 163001.

[2] S.V. Garimella, T. Persoons, J.A. Weibel, et al., Electronics thermal management in information and communications technologies: Challenges and future directions, IEEE Trans. Compon. Packag. Manuf. Technol. 7 (8) (2017) 1191–1205.

[3] A.K. Morya, M.C. Gardner, B. Anvari, et al., Wide Bandgap Devices in AC Electric Drives: Opportunities and Challenges, IEEE Trans. Transp. Electrif. 5 (1) (2019) 3–20.

[4] J.Y. Tsao, S. Chowdhury, M.A. Hollis, et al., Ultrawide-Bandgap Semiconductors: Research Opportunities and Challenges, Adv. Electron. Mater. 4 (1) (2017) 1600501.

[5] J. Vobecký, M. Rahimo, A. Kopta, et al., Exploring the silicon design limits of thin wafer IGBT technology: The controlled punch through (CPT) IGBT, in: Proceedings of the 20th International Symposium on Power Semiconductor Devices & IC's, Oralando, FL, 2008.

[6] Akio Nakagawa, Yusuke Kawaguchi, K. Nakamura, Achieving material limit characteristics in silicon power devices, International Workshop on Physics of Semiconductor Devices (2007).

[7] A. Bindra, Wide-Bandgap-Based Power Devices: Reshaping the power electronics landscape, IEEE Power Electron. Mag. 2 (1) (2015) 42–47.

[8] S. Fujita, Wide-bandgap semiconductor materials: For their full bloom, Jpn. J. Appl. Phys. 54 (3) (2015) 030101.

[9] H.A. Mantooth, M.D. Glover, P. Shepherd, Wide Bandgap Technologies and Their Implications on Miniaturizing Power Electronic Systems, IEEE J. Emerging Sel. Top. Power Electron. 2 (3) (2014) 374–385.

[10] J. Millan, P. Godignon, X. Perpina, et al., A survey of wide bandgap power semiconductor devices, IEEE Trans. Power Electron. 29 (5) (2014) 2155–2163.

[11] H. Okumura, A roadmap for future wide bandgap semiconductor power electronics, MRS Bull 40 (5) (2015) 439–444.

[12] M.N. Yoder, Wide Bandgap Semiconductor Materials and Devices, IEEE Trans. Electron Devices 43 (1996) 1633.

[13] K. Takahashi, A. Yoshikawa, A. Sandhu, Wide Bandgap Semiconductors, Springer, 2007.

[14] S.J. Pearton, F. Ren, M. Tadjer, et al., Perspective: Ga2O3for ultra-high power rectifiers and MOSFETS, J. Appl. Phys. 124 (22) (2018) 220901.

[15] M. Yang, M.-T. Li, Y.-C. Hua, et al., Experimental study on single-phase hybrid microchannel cooling using HFE-7100 for liquid-cooled chips, Int. J. Heat Mass Transfer 160 (2020) 120230.

[16] Y.C. Hua, H.L. Li, B.Y. Cao, Thermal spreading resistance in ballistic-diffusive regime for GaN HEMTs, IEEE Trans. Electron Devices 66 (8) (2019) 3296–3301.

[17] O. Semenov, A. Vassighi, M. Sachdev, Impact of self-heating effect on long-term reliability and performance degradation in CMOS circuits, IEEE Trans. Device Mater. Reliab. 6 (1) (2006) 17–27.

[18] Y. Zhao, Y. Qu, Impact of self-heating effect on transistor characterization and reliability issues in sub-10 nm technology nodes, IEEE J. Electron Devices Soc. 7 (2019) 829–836.

[19] R. Wang, J. Zhuge, R. Huang, et al., Investigation on self-heating effect in gate-all-around silicon nanowire MOSFETs from top-down approach, IEEE Electron Device Lett 30 (5) (2009) 559–561.

[20] X.D. Wang, W.D. Hu, X.S. Chen, et al., The Study of Self-Heating and Hot–Electron Effects for AlGaN/GaN Double-Channel HEMTs, IEEE Trans. Electron Devices 59 (5) (2012) 1393–1401.

[21] Avram Bar-Cohen, Joseph J. Maurer, A. Sivananthan, Near-junction microfluidic thermal management of RF power amplifiers, in: IEEE International Coriference on Microwaves, Communications, Antennas and Electronic Systems, 2015.

[22] Y. Li, L. Gong, B. Ding, et al., Thermal management of power electronics with liquid cooled metal foam heat sink, Int. J. Therm. Sci. 163 (2021) 106796.

[23] C. Zhang, J.W. Palko, M.T. Barako, et al., Design and optimization of well-ordered microporous copper structure for high heat flux cooling applications, Int. J. Heat Mass Transfer 173 (2021) 121241.

[24] Y. Peng, W. Li, B. Liu, et al., Integrated cooling (i-Cool) textile of heat conduction and sweat transportation for personal perspiration management, Nat. Commun. 12 (1) (2021) 6122.

[25] A. Bar-Cohen, M. Asheghi, T.J. Chainer, et al., The ICECool fundamentals effort on evaporative cooling of microelectronics, IEEE Trans. Compon. Packag. Manuf. Technol. 11 (10) (2021) 1546–1564.

[26] R. van Erp, R. Soleimanzadeh, L. Nela, et al., Co-designing electronics with microfluidics for more sustainable cooling, Nature 585 (7824) (2020) 211–216.

[27] A. Bar-Cohen, J.J. Maurer, D.H. Altman, Embedded cooling for wide bandgap power amplifiers: A review, J. Electron. Packag. 141 (4) (2019) 040803.

[28] M. Tawk, Y. Avenas, A. Kedous-Lebouc, et al., Numerical and experimental investigations of the thermal management of power electronics with liquid metal mini-channel coolers, IEEE Trans. Ind. Appl. 49 (3) (2013) 1421–1429.

[29] Z. Zuo, L.R. Hoover, A.L. Phillips, Advanced thermal architecture for cooling of high power electronics, IEEE Trans. Compon. Packag. Technol. 25 (4) (2002) 629–634.

[30] L. Tranchant, S. Hamamura, J. Ordonez-Miranda, et al., Two-Dimensional Phonon Polariton Heat Transport, Nano Lett 19 (10) (2019) 6924–6930.

[31] Y. Won, J. Cho, D. Agonafer, et al., Cooling limits for GaN HEMT technology, in: 2013 IEEE Compound Semiconductor Integrated Circuit Symposium, 2013.

[32] J.S. Lewis, T. Perrier, Z. Barani, et al., Thermal interface materials with graphene fillers: review of the state of the art and outlook for future applications, Nanotechnology 32 (14) (2021) 142003.

[33] J.Y. Yang, G. Qin, M. Hu, Nontrivial contribution of Fröhlich electron-phonon interaction to lattice thermal conductivity of wurtzite GaN, Appl. Phys. Lett. 109 (24) (2016) 242103.

[34] D.S. Tang, G.Z. Qin, M. Hu, et al., Thermal transport properties of GaN with biaxial strain and electron-phonon coupling, J. Appl. Phys. 127 (3) (2020) 035102.

[35] H. Guo, Y. Kong, T. Chen, Thermal simulation of high power GaN-on-diamond substrates for HEMT applications, Diamond Relat. Mater. 73 (2017) 260–266.

[36] C. Song, J. Kim, J. Cho, The effect of GaN epilayer thickness on the near-junction thermal resistance of GaN-on-diamond devices, Int. J. Heat Mass Transfer 158 (2020) 119992.

[37] Y. Shen, Y.C. Hua, H.L. Li, et al., Spectral Thermal Spreading Resistance of Wide-Bandgap Semiconductors in Ballistic-Diffusive Regime, IEEE Trans. Electron Devices 69 (6) (2022) 3047–3054.

[38] H.L. Li, J. Shiomi, B.Y. Cao, Ballistic-Diffusive Heat Conduction in Thin Films by Phonon Monte Carlo Method: Gray Medium Approximation Versus Phonon Dispersion, J. Heat Transfer 142 (11) (2020) 112502.

[39] Q. Hao, H. Zhao, Y. Xiao, et al., Hybrid electrothermal simulation of a 3-D fin-shaped field-effect transistor based on GaN nanowires, IEEE Trans. Electron Devices 65 (3) (2018) 921–927.

[40] Q. Hao, H. Zhao, Y. Xiao, A hybrid simulation technique for electrothermal studies of two-dimensional GaN-on-SiC high electron mobility transistors, J. Appl. Phys. 121 (20) (2017) 204501.

[41] Q. Li, X.Y. Zhu, Y.M. Xuan, Modeling heat generation in high power density nanometer scale GaAs/InGaAs/AlGaAs PHEMT, Int. J. Heat Mass Transfer 81 (2015) 130–136.

[42] A. Ashok, D. Vasileska, O.L. Hartin, et al., Electrothermal Monte Carlo Simulation of GaN HEMTs Including Electron–Electron Interactions, IEEE Trans. Electron Devices 57 (2010) 562–570.

[43] A.M. Joseph, B.Y. Cao, Electron heat source driven heat transport in GaN at nanoscale: electron-phonon Monte Carlo simulations and a two-temperature model, Materials 15 (2022) 1651.

[44] A.M. Joseph, B.Y. Cao, An electron-phonon Monte Carlo study on thermal transport in GaN, Int. J. Therm. Sci. 181 (2022) 107742.

[45] E.P. Pokatilov, D.L. Nika, A.A. Balandin, Confined electron-confined phonon scattering rates in wurtzite AlN/GaN/AlN heterostructures, J. Appl. Phys. 95 (2004) 5626.

[46] J.J. Shi, X.L. Chu, E.M. Goldys, Propagating optical-phonon modes and their electron-phonon interactions in wurtzite GaN/AlxGa1-xN quantum wells, Phys. Rev. B 70 (2004) 115318.

[47] E.O. Kane, Band structure of Indium Antimonide, J. Phys. Chem. Solids 1 (1957) 249–261.

[48] Q. Hao, G. Chen, M.-S. Jeng, Frequency-dependent Monte Carlo simulations of phonon transport in two-dimensional porous silicon with aligned pores, J. Appl. Phys. 106 (11) (2009) 114321.

[49] Q. Hao, Influence of structure disorder on the lattice thermal conductivity of polycrystals: A frequency-dependent phonon-transport study, J. Appl. Phys. 111 (1) (2012) 014309.

[50] H.L. Li, Y. Shen, Y.C. Hua, et al., Hybrid Monte Carlo-Diffusion Studies of Modeling Self-Heating in Ballistic-Diffusive Regime for GaN HEMTs, J. Electron. Packag. 145 (2023) 011203.

[51] J.Z. Zhang, A. Dyson, B.K. Ridley, Rapid hot-electron energy relaxation in lattice-matched InAlN/AlN/GaN heterostructures, Appl. Phys. Lett. 102 (6) (2013) 062104.

[52] J.Z. Zhang, A. Dyson, B.K. Ridley, Hot electron energy relaxation in lattice-matched InAlN/AlN/GaN heterostructures: The sum rules for electron-phonon interactions and hot-phonon effect, J. Appl. Phys. 117 (2) (2015) 025701.

[53] J.Z. Zhang, Energy relaxation of hot electrons in Si-doped GaN, J. Appl. Phys. 115 (20) (2014) 203704.

[54] P.Y. Yu, M. Cardona, Fundamentals of Semiconductors: Physics and Materials Properties, Springer, Berlin, 2005.

[55] T. Ruf, J. Serrano, M. Cardona, et al., Phonon dispersion curves in wurtzite-structure GaN determined by inelastic x-ray scattering, Phys. Rev. Lett. 86 (5) (2001) 906–909.

[56] K. Parlinski, Z.Q. Li, Y. Kawazoe, First-Principles Determination of the Soft Mode in Cubic ZrO2, Phys. Rev. Lett. 78 (1997) 4063–4066.

[57] L. Chaput, A. Togo, I. Tanaka, et al., Phonon-phonon interactions in transition metals, Phys. Rev. B 84 (2011) 094302.

[58] X. Gonze, C. Lee, Dynamical matrices, Born effective charges, dielectric permittivity tensors, and interatomic force constants from density-functional perturbation theory, Phys. Rev. B 55 (1997) 10355–10368.

[59] R.M. Pick, M.H. Cohen, R.M. Martin, Microscopic Theory of Force Constants in the Adiabatic Approximation, Phys. Rev. B 1 (2) (1970) 910–920.

[60] W. Li, J. Carrete, N.A. Katcho, et al., ShengBTE: A solver of the Boltzmann transport equation for phonons, Comput. Phys. Commun. 185 (6) (2014) 1747–1758.

[61] L. Lindsay, D. Broido, T. Reinecke, Thermal conductivity and large isotope effect in GaN from first principles, Phys. Rev. Lett. 109 (9) (2012) 095901.

[62] J. Garg, T. Luo, G. Chen, Spectral concentration of thermal conductivity in GaN-A first-principles study, Appl. Phys. Lett. 112 (25) (2018) 252101.

[63] Q. Zheng, C. Li, A. Rai, et al., Thermal conductivity of GaN, GaN71, and SiC from 150 K to 850 K, Phys. Rev. Mater. 3 (1) (2019) 014601.

[64] D.S. Tang, Y.C. Hua, Y.G. Zhou, et al., Thermal conductivity modeling of GaN films, Acta Phys. Sin. 70 (4) (2021) 045101.

[65] S.J. Sheih, K.T. Tsen, D.K. Ferry, et al., Electron-phonon interactions in the wide band-gap semiconductor GaN, Appl. Phys. Lett. 67 (1995) 1757.

[66] H. Kawai, K. Yamashita, E. Cannuccia, et al., Electron-electron and electron-phonon correlation effects on the finite-temperature electronic and optical properties of zinc-blende GaN, Phys. Rev. B 89 (2014) 085202.

[67] J. Noffsinger, F. Giustino, B.D. Malone, et al., EPW: A program for calculating the electron–phonon coupling using maximally localized Wannier functions, Comput. Phys. Commun. 181 (12) (2010) 2140–2148.

[68] S. Poncé, E.R. Margine, C. Verdi, et al., EPW: Electron–phonon coupling, transport and superconducting properties using maximally localized Wannier functions, Comput. Phys. Commun. 209 (2016) 116–133.

[69] J. Callaway, Model for Lattice Thermal Conductivity at Low Temperatures, Phys. Rev. 113 (4) (1959) 1046–1051.

[70] P.G. Klemens, The Scattering of Low-Frequency Lattice Waves by Static Imperfections, Proc. Phys. Soc. A 68 (1955) 1113.

[71] H. Li, R. Hanus, C.A. Polanco, et al., GaN thermal transport limited by the interplay of dislocations and size effects, Phys. Rev. B 102 (1) (2020) 014313.

[72] T. Wang, J. Carrete, N. Mingo, et al., Phonon Scattering by Dislocations in GaN, ACS Appl. Mater. Interfaces 11 (8) (2019) 8175–8181.

[73] T. Wang, J. Carrete, A. van Roekeghem, et al., Ab initio phonon scattering by dislocations, Phys. Rev. B 95 (24) (2017) 245304.

[74] A. Katre, J. Carrete, T. Wang, et al., Phonon transport unveils the prevalent point defects in GaN, Phys. Rev. Mater. 2 (5) (2018) 050602 (R).

[75] J. Carrete, B. Vermeersch, A. Katre, et al., almaBTE: A solver of the space–time dependent Boltzmann transport equation for phonons in structured materials, Comput. Phys. Commun. 220 (2017) 351–362.

[76] Y. Zhou, X. Zhang, M. Hu, Quantitatively analyzing phonon spectral contribution of thermal conductivity based on nonequilibrium molecular dynamics simulations. I. From space Fourier transform, Phys. Rev. B 92 (19) (2015) 195204.

[77] T. Feng, W. Yao, Z. Wang, et al., Spectral analysis of nonequilibrium molecular dynamics: Spectral phonon temperature and local nonequilibrium in thin films and across interfaces, Phys. Rev. B 95 (19) (2017) 195202.

[78] A.J. Gabourie, Z. Fan, T. Ala-Nissila, et al., Spectral decomposition of thermal conductivity: Comparing velocity decomposition methods in homogeneous molecular dynamics simulations, Phys. Rev. B 103 (20) (2021) 205421.

[79] A. Rohskopf, R. Li, T. Luo, et al., A Computational Method for Studying Vibrational Mode Dynamics. arXiv (2021) 2108.04795.

[80] Y. Sun, Y. Zhou, J. Han, et al., Strong phonon localization in PbTe with dislocations and large deviation to Matthiessen's rule. npj, Comput. Mater. 5 (1) (2019) 97.

[81] A.P. Bartók, J. Kermode, N. Bernstein, et al., Machine Learning a General-Purpose Interatomic Potential for Silicon, Phys. Rev. X 8 (4) (2018) 041048.

[82] Y.B. Liu, J.Y. Yang, G.M. Xin, et al., Machine learning interatomic potential developed for molecular simulations on thermal properties of beta-Ga$_2$O$_3$, J. Chem. Phys. 153 (14) (2020) 144501.

[83] L.C. Erhard, J. Rohrer, K. Albe, et al., A machine-learned interatomic potential for silica and its relation to empirical models, npj Comput. Mater. 8 (1) (2022) 90.

[84] X. Gu, C.Y. Zhao, Thermal conductivity of single-layer MoS$_{2(1-x)}$Se$_2$x alloys from molecular dynamics simulations with a machine-learning-based interatomic potential, Comput. Mater. Sci. 165 (2019) 74–81.

[85] Y. Hu, T. Feng, X. Gu, et al., Unification of nonequilibrium molecular dynamics and the mode-resolved phonon Boltzmann equation for thermal transport simulations, Phys. Rev. B 101 (15) (2020) 155308.

[86] C. Dames, G. Chen, 1ω, 2ω, and 3ω methods for measurements of thermal properties, Rev. Sci. Instrum. 76 (12) (2005) 124902.

[87] L. Lu, W. Yi, D.L. Zhang, 3ω method for specific heat and thermal conductivity measurements, Rev. Sci. Instrum. 72 (7) (2001) 2996–3003.

[88] T. Yamane, N. Nagai, S.I. Katayama, et al., Measurement of thermal conductivity of silicon dioxide thin films using a 3ω method, J. Appl. Phys. 91 (12) (2002) 9772.

[89] W. Liu, A.A. Balandin, Temperature dependence of thermal conductivity of Al$_x$Ga$_{1-x}$N thin films measured by the differential 3ω technique, Appl. Phys. Lett. 85 (22) (2004) 5230–5232.

[90] D.G. Cahill, Thermal conductivity measurement from 30 to 750 K: the 3ω method, Rev. Sci. Instrum. 61 (2) (1990) 802–808.

[91] O. Churiukova, A. Jeżowski, P. Stachowiak, et al., Thermal conductivity of donor-doped GaN measured with 3ω and stationary methods, Low Temp. Phys. 41 (7) (2015) 563–566.

[92] Y.C. Hua, B.Y. Cao, A two-sensor 3ω-2ω method for thermal boundary resistance measurement, J. Appl. Phys. 129 (12) (2021) 125107.

[93] Z. Cheng, F. Mu, L. Yates, et al., Interfacial thermal conductance across room-temperature-bonded GaN/Diamond interfaces for GaN-on-diamond devices, ACS Appl. Mater. Interfaces 12 (7) (2020) 8376–8384.

[94] J.P. Feser, J. Liu, D.G. Cahill, Pump-probe measurements of the thermal conductivity tensor for materials lacking in-plane symmetry, Rev. Sci. Instrum. 85 (10) (2014) 104903.

[95] P. Jiang, X. Qian, R. Yang, Time-domain thermoreflectance (TDTR) measurements of anisotropic thermal conductivity using a variable spot size approach, Rev. Sci. Instrum. 88 (7) (2017) 074901.

[96] J. Zhu, D. Tang, W. Wang, et al., Ultrafast thermoreflectance techniques for measuring thermal conductivity and interface conductance of thin films, J. Appl. Phys. 108 (9) (2010) 094315.

[97] V. Asnin, F.H. Pollak, J. Ramer, et al., High spatial resolution thermal conductivity of lateral epitaxial overgrown GaN/sapphire (0001) using a scanning thermal microscope, Appl. Phys. Lett. 75 (9) (1999) 1240–1242.

[98] D. Florescu, V. Asnin, F.H. Pollak, et al., High spatial resolution thermal conductivity and Raman spectroscopy investigation of hydride vapor phase epitaxy grown n-GaN/sapphire (0001): Doping dependence, J. Appl. Phys. 88 (6) (2000) 3295–3300.

[99] A. Jeżowski, O. Churiukova, J. Mucha, et al., Thermal conductivity of heavily doped bulk crystals GaN: O. Free carriers contribution, Mater. Res. Express 2 (8) (2015) 085902.

[100] G.A. Slack, L.J. Schowalter, D. Morelli, et al., Some effects of oxygen impurities on AlN and GaN, J. Cryst. Growth 246 (3-4) (2002) 287–298.

[101] A. Jeżowski, B. Danilchenko, M. Boćkowski, et al., Thermal conductivity of GaN crystals in 4.2-300 K range, Solid State Commun 128 (2-3) (2003) 69–73.

[102] K. Jagannadham, E. Berkman, N. Elmasry, Thermal conductivity of semi-insulating, p-type, and n-type GaN films on sapphire, J. Vac. Sci. Technol. A 26 (3) (2008) 375–379.

[103] C.Y. Luo, H. Marchand, D.R. Clarke, et al., Thermal conductivity of lateral epitaxial overgrown GaN films, Appl. Phys. Lett. 75 (26) (1999) 4151–4153.

[104] P. Paskov, M. Slomski, J. Leach, et al., Effect of Si doping on the thermal conductivity of bulk GaN at elevated temperatures–theory and experiment, AIP Adv 7 (9) (2017) 095302.

[105] R. Rounds, B. Sarkar, T. Sochacki, et al., Thermal conductivity of GaN single crystals: Influence of impurities incorporated in different growth processes, J. Appl. Phys. 124 (10) (2018) 105106.

[106] C. Mion, J. Muth, E. Preble, et al., Accurate dependence of gallium nitride thermal conductivity on dislocation density, Appl. Phys. Lett. 89 (9) (2006) 092123.

[107] M. Kamano, M. Haraguchi, T. Niwaki, et al., Temperature dependence of the thermal conductivity and phonon scattering time of a bulk GaN crystal, Jap. J. Appl. Phys. 41 (8R) (2002) 5034.

[108] T.E. Beechem, A.E. McDonald, E.J. Fuller, et al., Size dictated thermal conductivity of GaN, J. Appl. Phys. 120 (9) (2016) 095104.

[109] H. Shibata, Y. Waseda, H. Ohta, et al., High thermal conductivity of gallium nitride (GaN) crystals grown by HVPE process, Mater. Trans. 48 (10) (2007) 2782–2786.

[110] K. Yuan, X. Zhang, D. Tang, et al., Anomalous pressure effect on the thermal conductivity of ZnO, GaN, and AlN from first-principles calculations, Phys. Rev. B 98 (14) (2018) 144303.

[111] A. Togo, L. Chaput, I. Tanaka, Distributions of phonon lifetimes in Brillouin zones, Phys. Rev. B 91 (9) (2015) 094306.

[112] G. Chen, Nanoscale Energy Transport and Conversion: A Parallel Treatment of Electrons, Molecules, Phonons, and Photons, Oxford University Press, 2014.

[113] Y.X. Xu, G. Wang, Y.G. Zhou, Broadly manipulating the interfacial thermal energy transport across the Si/4H-SiC interfaces via nanopatterns, Int. J. Heat Mass Transfer 187 (2022) 122499.

[114] J. Soltys, J. Piechota, M. Lopuszynski, et al., A comparative DFT study of electronic properties of 2H-, 4H, and 6H-SiC (0001) and SiC (000-1) clean surfaces: significance of the surface Stark effect, New J. Phys. 12 (2010) 043024.

[115] N.H. Protik, A. Katre, L. Lindsay, et al., Phonon thermal transport in 2H, 4H and 6H silicon carbide from first principles, Mater. Today Phys. 1 (2017) 31–38.

[116] X. Qian, P.Q. Jiang, R.G. Yang, Anisotropic thermal conductivity of 4H and 6H silicon carbide measured using time-domain thermoreflectance, Mater. Today Phys. 3 (2017) 70–75.

[117] J.B. Casday, R.W. Johnson, Status of silicon carbide (SiC) as a wide-bandgap semiconductor for high-temperature applications: A review, Solid State Electron 29 (1996) 1409–1422.

[118] C.H. Park, B.-H. Cheong, K.-H. Lee, et al., Structural and electronic properties of cubic, 2H, 4H, and 6H SiC, Phys. Rev. B 49 (1994) 4485 (4489).

[119] J.P. Freedman, J.H. Leach, E.A. Preble, et al., Universal phonon mean free path spectra in crystalline semiconductors at high temperature, Sci. Rep. 3 (2013) 2963.

[120] L. Lindsay, D.A. Broido, T.L. Reinecke, Ab initio thermal transport in compound semiconductors, Phys. Rev. B 87 (2013) 165201.

[121] E.T. Swartz, R.O. Pohl, Thermal boundary resistance, Rev. Mod. Phys. 61 (3) (1989) 605–668.

[122] J. Chen, X. Xu, J. Zhou, et al., Interfacial thermal resistance: Past, present, and future, Rev. Mod. Phys. 94 (2) (2022) 025002.

[123] K. Sääskilahti, J. Oksanen, J. Tulkki, et al., Role of anharmonic phonon scattering in the spectrally decomposed thermal conductance at planar interfaces, Phys. Rev. B 90 (2014) 134312.

[124] T. Feng, Y. Zhong, J. Shi, et al., Unexpected high inelastic phonon transport across solid-solid interface: Modal nonequilibrium molecular dynamics simulations and Landauer analysis, Phys. Rev. B 99 (2019) 045301.

[125] Y.H. Li, R.S. Qi, R.C. Shi, et al., Atomic-scale probing of heterointerface phonon bridges in nitride semiconductor, Proc. Natl. Acad. Sci. 119 (8) (2022) e2117027119.

[126] Y. Zhou, M. Hu, Full quantification of frequency-dependent interfacial thermal conductance contributed by two-and three-phonon scattering processes from nonequilibrium molecular dynamics simulations, Phys. Rev. B 95 (11) (2017) 115313.

[127] K. Gordiz, A. Henry, Phonon transport at interfaces: Determining the correct modes of vibration, J. Appl. Phys. 119 (1) (2016) 015101.

[128] A. Sarua, H. Ji, K.P. Hilton, et al., Thermal Boundary Resistance Between GaN and Substrate in AlGaN/GaN Electronic Devices, IEEE Trans. Electron Devices 54 (12) (2007) 3152–3158.

[129] H. Zheng, K. Jagannadham, Influence of dopants on the thermal conductance of GaN-sapphire interface, IEEE Trans. Electron Devices 60 (6) (2013) 1911–1915.

[130] J. Cho, Y. Li, W.E. Hoke, et al., Phonon scattering in strained transition layers for GaN heteroepitaxy, Phys. Rev. B 89 (11) (2014) 115301.

[131] J. Zhu, X. Wu, D.M. Lattery, et al., The ultrafast laser pump-probe technique for thermal characterization of materials with micro/nanostructures, Nanoscale Microscale Thermophys. Eng. 21 (3) (2017) 177–198.

[132] A. Manoi, J.W. Pomeroy, N. Killat, et al., Benchmarking of Thermal Boundary Resistance in AlGaN/GaN HEMTs on SiC substrates: Implications of the nucleation layer microstructure, IEEE Electron Device Lett 31 (12) (2010) 1395–1397.

[133] J. Cho, E. Bozorg-Grayeli, D.H. Altman, et al., Low Thermal Resistances at GaN-SiC Interfaces for HEMT Technology, IEEE Electron Device Lett 33 (3) (2012) 378–380.

[134] E. Ziade, J. Yang, G. Brummer, et al., Thermal transport through GaN-SiC interfaces from 300 to 600 K, Appl. Phys. Lett. 107 (9) (2015) 091605.

[135] H.C. Nochetto, N.R. Jankowski, A. Bar-Cohen, GaN HEMT junction temperature dependence on diamond substrate anisotropy and thermal boundary resistance, in: 2012 IEEE Compound Semiconductor Integrated Circuit Symposium (CSICS), IEEE, 2012.

[136] F. Mu, Z. Cheng, J. Shi, et al., High thermal boundary conductance across bonded heterogeneous GaN-SiC interfaces, ACS Appl. Mater. Interfaces 11 (36) (2019) 33428–33434.

[137] J. Kuzmik, S. Bychikhin, D. Pogany, et al., Thermal characterization of MBE–grown GaN/AlGaN/GaN device on single crystalline diamond, J. Appl. Phys. 109 (8) (2011) 086106.

[138] J. Cho, Z. Li, E. Bozorg-Grayeli, et al., Improved thermal interfaces of GaN–Diamond composite substrates for HEMT applications, IEEE Trans. Compon. Packag. Manuf. Technol. 3 (1) (2013) 79–85.

[139] J.W. Pomeroy, M. Bernardoni, D.C. Dumka, et al., Low thermal resistance GaN-on-diamond transistors characterized by three-dimensional Raman thermography mapping, Appl. Phys. Lett. 104 (8) (2014) 083513.

[140] H. Sun, R.B. Simon, J.W. Pomeroy, et al., Reducing GaN-on-diamond interfacial thermal resistance for high power transistor applications, Appl. Phys. Lett. 106 (11) (2015) 111906.

[141] J. Cho, D. Francis, D.H. Altman, et al., Phonon conduction in GaN-diamond composite substrates, J. Appl. Phys. 121 (5) (2017) 055105.

[142] L. Yates, J. Anderson, X. Gu, et al., Low thermal boundary resistance interfaces for GaN-on-diamond devices, ACS Appl. Mater. Interfaces 10 (28) (2018) 24302–24309.

[143] Y. Zhou, J. Anaya, J. Pomeroy, et al., Barrier-layer optimization for enhanced GaN-on-diamond device cooling, ACS Applied Materials & Interface 9 (39) (2017) 34416–34422.

[144] C.A. Polanco, L. Lindsay, Phonon thermal conductance across GaN-AlN interfaces from first principles, Phys. Rev. B 99 (7) (2019) 075202.

[145] A. van Roekeghem, B. Vermeersch, J. Carrete, et al., Thermal Resistance of GaN/AlN Graded Interfaces, Phys. Rev. Appl. 11 (3) (2019) 034036.

[146] J.T. Gaskins, G. Kotsonis, A. Giri, et al., Thermal boundary conductance across heteroepitaxial ZnO/GaN interfaces: Assessment of the phonon gas model, Nano Lett 18 (2018) 7469–7477.

[147] Y. Guo, Z. Zhang, M. Bescond, et al., Anharmonic phonon-phonon scattering at the interface between two solids by nonequilibrium Green's function formalism, Phys. Rev. B 103 (17) (2021) 174306.

[148] Z. Liang, M. Hu, Tutorial: Determination of thermal boundary resistance by molecular dynamics simulations, J. Appl. Phys. 123 (19) (2018) 191101.

[149] E. Lee, T. Luo, Thermal transport across solid-solid interfaces enhanced by pre-interface isotope-phonon scattering, Appl. Phys. Lett. 112 (1) (2018) 011603.

[150] R. Li, K. Gordiz, A. Henry, et al., Effect of light atoms on thermal transport across solid-solid interfaces, Phys. Chem. Chem. Phys. 21 (31) (2019) 17029–17035.

[151] D. Wu, H. Ding, Z.-Q. Fan, et al., High interfacial thermal conductance across heterogeneous GaN/graphene interface, Appl. Surf. Sci. 581 (2022) 152344.

[152] Q. Wang, X. Wang, X. Liu, et al., Interfacial engineering for the enhancement of interfacial thermal conductance in GaN/AlN heterostructure, J. Appl. Phys. 129 (23) (2021) 235102.

[153] E. Lee, T. Yoo, T. Luo, The role of intermediate layers in thermal transport across GaN/SiC interfaces, in: 2017 16th IEEE Intersociety Conference on Thermal and Thermomechanical Phenomena in Electronic Systems (ITherm), Orlando, FL, USA, 2017.

[154] Z. Liang, K. Sasikumar, P. Keblinski, Thermal transport across a substrate-thin–film interface: effects of film thickness and surface roughness, Phys. Rev. Lett. 113 (6) (2014) 065901.

[155] B. Yang, H. Yang, T. Li, et al., Thermal transport at 6H-SiC/graphene buffer layer/GaN heterogeneous interface, Appl. Surf. Sci. 536 (2021) 147828.

[156] X.W. Zhou, R.E. Jones, C.J. Kimmer, et al., Relationship of thermal boundary conductance to structure from an analytical model plus molecular dynamics simulations, Phys. Rev. B 87 (9) (2013) 094303.

[157] M. Hu, X. Zhang, D. Poulikakos, et al., Large "near junction" thermal resistance reduction in electronics by interface nanoengineering, Int. J. Heat Mass Transfer 54 (2011) 5183–5191.

[158] R. Suresh, K. P. Bloschock and A. Bar-Cohen, Advanced thermal management technologies for defense electronics. Defense Transformation and Net-Centric Systems, 2012.

[159] S.V. Garimella, Advances in mesoscale thermal management technologies for microelectronics, Microelectron. J. 37 (11) (2006) 1165–1185.

[160] D.E. Field, J.A. Cuenca, M. Smith, et al., Crystalline Interlayers for Reducing the Effective Thermal Boundary Resistance in GaN-on-Diamond, ACS Appl. Mater. Interfaces (2020) 54138–54145.

[161] B. Chatterjee, K. Zeng, C.D. Nordquist, et al., Device-Level Thermal Management of Gallium Oxide Field-Effect Transistors, IEEE Trans. Compon. Packag. Manuf. Technol. 9 (12) (2019) 2352–2365.

[162] A.L. Moore, L. Shi, Emerging challenges and materials for thermal management of electronics, Mater. Today 17 (4) (2014) 163–174.

[163] M. Faqir, T. Batten, T. Mrotzek, et al., Improved thermal management for GaN power electronics: Silver diamond composite packages, Microelectron. Reliab. 52 (12) (2012) 3022–3025.

[164] S. Anandan, V. Ramalingam, Thermal management of electronics: A review of literature, Therm. Sci. 12 (2) (2008) 5–26.

[165] S. Yang, J. Wang, G. Dai, et al., Controlling macroscopic heat transfer with thermal metamaterials: Theory, experiment and application, Phys. Rep. 908 (2021) 1–65.

[166] L.F. Zhang, J. Ren, J.S. Wang, et al., Topological nature of the phonon Hall effect, Phys. Rev. Lett. 105 (22) (2010) 225901.

[167] Y. Liu, C.S. Lian, Y. Li, et al., Pseudospins and topological effects of phonons in a kekule lattice, Phys. Rev. Lett. 119 (25) (2017) 255901.

[168] Y.C. Hua, B.Y. Cao, Anisotropic Heat Conduction in Two-Dimensional Periodic Silicon Nanoporous Films, J. Phys. Chem. C 121 (9) (2017) 5293–5301.

[169] Y. Hua, B. Cao, Interface-based two-way tuning of the in-plane thermal transport in nanofilms, J. Appl. Phys. 123 (11) (2018) 114304.

[170] Z. Zhang, Y. Ouyang, Y. Guo, et al., Hydrodynamic phonon transport in bulk crystalline polymers, Phys. Rev. B 102 (19) (2020) 195302.

[171] S. Lee, D. Broido, K. Esfarjani, et al., Hydrodynamic phonon transport in suspended graphene, Nat. Commun. 6 (2015) 6290.

[172] Y. Hu, D. Li, Y. Yin, et al., The important role of strain on phonon hydrodynamics in diamond-like bi-layer graphene, Nanotechnology 31 (33) (2020) 335711.

[173] Z. Ding, J. Zhou, B. Song, et al., Phonon Hydrodynamic Heat Conduction and Knudsen Minimum in Graphite, Nano Lett 18 (1) (2018) 638–649.

[174] Y.Y. Guo, M.R. Wang, Phonon hydrodynamics and its applications in nanoscale heat transport, Phys. Rep. 595 (2015) 1–44.

[175] Yo Machida, Nayuta Matsumoto, Takayuki Isono, et al., Phonon hydrodynamics and ultrahigh–roomtemperature thermal conductivity in thin graphite, Science 367 (2020) 309–312.

[176] V. Martelli, J.L. Jimenez, M. Continentino, et al., Thermal Transport and Phonon Hydrodynamics in Strontium Titanate, Phys. Rev. Lett. 120 (12) (2018) 125901.

[177] H. Shao, M. Jin, B. Peng, et al., First-Principles Study of Manipulating the Phonon Transport of Molybdenum Disulfide by Sodium Intercalating, J. Phys. Chem. C 122 (5) (2018) 2632–2640.

[178] C. Liu, P. Lu, Z. Gu, et al., Bidirectional Tuning of Thermal Conductivity in Ferroelectric Materials Using E-Controlled Hysteresis Characteristic Property, J. Phys. Chem. C 124 (48) (2020) 26144–26152.

[179] B.Y. Cao, W.J. Yao, Z.Q. Ye, Networked nanoconstrictions: An effective route to tuning the thermal transport properties of graphene, Carbon 96 (2016) 711–719.

[180] C. Yu, Y. Ouyang, J. Chen, A perspective on the hydrodynamic phonon transport in two-dimensional materials, J. Appl. Phys. 130 (1) (2021) 010902.

[181] Z. Yang, K. Yuan, N. Li, et al., Giant manipulation of phonon hydrodynamics in ferroelectric bilayer boron nitride at room temperature and beyond, ACS Appl. Energy Mater. 5 (2022) 8781–8790.

[182] Z. Ding, K. Chen, B. Song, et al., Observation of second sound in graphite over 200 K, Nat. Commun. 13 (2022) 285.

[183] Y. Zhou, X. Zhang, M. Hu, Nonmonotonic diameter dependence of thermal conductivity of extremely thin Si nanowires: Competition between hydrodynamic phonon flow and boundary scattering, Nano Lett 17 (2017) 1269–1276.

[184] L. Yang, Y. Tao, Y. Zhu, et al., Observation of superdiffusive phonon transport in aligned atomic chains, Nat. Nanotechnol. 16 (2021) 764–768.

[185] P. Torres, S. Wu, S. Ju, et al., Descriptors of intrinsic hydrodynamic thermal transport: screening a phonon database in a machine learning approach, J. Phys.: Condens. Matter 34 (2022) 135702.

[186] D.S. Tang, B.Y. Cao, Phonon thermal transport properties of GaN with symmetry-breaking and lattice deformation induced by the electric field, Int. J. Heat Mass Transfer 179 (2021) 121659.

[187] I. Souza, J. Iniguez, D. Vanderbilt, First-principles approach to insulators in finite electric fields, Phys. Rev. Lett. 89 (11) (2002) 117602.

[188] Y. Quan, S.Y. Yue, B. Liao, Electric field effect on the thermal conductivity of wurtzite GaN, Appl. Phys. Lett. 118 (16) (2021) 162110.

[189] R. Rastgarkafshgarkolaei, J. Zhang, C.A. Polanco, et al., Maximization of thermal conductance at interfaces via exponentially mass-graded interlayers, Nanoscale 11 (13) (2019) 6254–6262.

[190] B.Y. Cao, J.H. Zou, G.J. Hu, et al., Enhanced thermal transport across multilayer graphene and water by interlayer functionalization, Appl. Phys. Lett. 112 (4) (2018) 041603.

[191] Y.C. Hua, B.Y. Cao, Study of phononic thermal transport across nanostructured interfaces using phonon Monte Carlo method, Int. J. Heat Mass Transfer 154 (2020) 119762.

[192] Z. Zhang, Y. Guo, M. Bescond, et al., Heat Conduction Theory Including Phonon Coherence, Phys. Rev. Lett. 128 (1) (2022) 015901.

[193] L. Isaeva, G. Barbalinardo, D. Donadio, et al., Modeling heat transport in crystals and glasses from a unified lattice-dynamical approach, Nat. Commun. 10 (1) (2019) 3853.

[194] M. Simoncelli, N. Marzari, F. Mauri, Unified theory of thermal transport in crystals and glasses, Nat. Phys. 15 (8) (2019) 809–813.

[195] Z. Zhang, Y. Guo, M. Bescond, et al., Generalized decay law for particlelike and wavelike thermal phonons, Phys. Rev. B 103 (18) (2021) 184307.

[196] J. Gleize, J. Frandon, F. Demangeot, et al., Angular dispersion of polar phonons in a hexagonal GaN-AlN superlattice, Mater. Sci. Eng., R B82 (2001) 27–29.

[197] J. Gleize, M.A. Renucci, J. Frandon, et al., Anisotropy effects on polar optical phonons in wurtzite GaN/AlN superlattices, Phys. Rev. B 60 (1999) 15985–15992.

[198] C.J. Stanton, G.D. Sanders, R. Liu, et al., Coherent phonons, nanoseismology and THz radiation in InGaN/GaN heterostructures, Superlattices Microstruct 34 (3-6) (2003) 525–529.

[199] T.R. Paudel, W.R.L. Lambrecht, Computational study of phonon modes in short-period AlN/GaN superlattices, Phys. Rev. B 80 (10) (2009) 104202.

[200] A. Spindlberger, D. Kysylychyn, L. Thumfart, et al., Cross-plane thermal conductivity of GaN/AlN superlattices, Appl. Phys. Lett. 118 (6) (2021) 062105.

[201] L. Zhang, Full optical phonon states and their dispersive spectra of a wurtzite GaN/AlGaN superlattice: Quantum size effect, Phys. Status Solidi B 248 (9) (2011) 2120–2127.

[202] A.D. Rodrigues, M.P.F. de Godoy, C. Mietze, et al., Phonon localization in cubic GaN/AlN superlattices, Solid State Commun 186 (2014) 18–22.

[203] V. Darakchieva, E. Valcheva, P.P. Paskov, et al., Phonon mode behavior in strained wurtziteAlN/GaNsuperlattices, Phys. Rev. B 71 (11) (2005) 115329.

[204] E.P. Pokatilov, D.L. Nika, A.A. Balandin, Phonon spectrum and group velocities in AlN/GaN/AlN and related heterostructures, Superlattices Microstruct 33 (3) (2003) 155–171.

[205] V. Davydov, E. Roginskii, Y. Kitaev, et al., Phonons in Short-Period GaN/AlN Superlattices: Group-Theoretical Analysis, Ab initio Calculations, and Raman Spectra, Nanomaterials 11 (2) (2021) 286.

[206] G.F. Xie, D. Ding, G. Zhang, Phonon coherence and its effect on thermal conductivity of nanostructures, Adv. Phys.: X 3 (1) (2018) 719–754.

[207] M. Maldovan, Phonon wave interference and thermal bandgap materials, Nat. Mater. 14 (7) (2015) 667–674.

[208] V.E.L. Gasparetto, M.S.A. ElSayed, Shape transformers for phononic band gaps tuning in two-dimensional Bloch-periodic lattice structures, Eur. J. Mech. A. Solids 89 (2021) 104278.

[209] S. Xiong, K. Saaskilahti, Y.A. Kosevich, et al., Blocking phonon ptransport by structural resonances in alloy-based nanophononic metamaterials leads to ultralow thermal conductivity, Phys. Rev. Lett. 117 (2) (2016) 025503.

[210] B.L. Davis, M.I. Hussein, Nanophononic metamaterial: thermal conductivity reduction by local resonance, Phys. Rev. Lett. 112 (5) (2014) 055505.

[211] H. Xue, D. Jia, Y. Ge, et al., Observation of dislocation-induced topological modes in a three-dimensional acoustic topological insulator, Phys. Rev. Lett. 127 (21) (2021) 214301.

[212] H. Wang, Y. Cheng, M. Nomura, et al., Synergistic impeding of phonon transport through resonances and screw dislocations, Phys. Rev. B 103 (8) (2021) 085414.

[213] J. Ordonez-Miranda, L. Tranchant, Y. Chalopin, et al., Thermal conductivity of nano-layered systems due to surface phonon-polaritons, J. Appl. Phys. 115 (5) (2014) 054311.

[214] S.S. Ng, Z. Hassan, H. Abu Hassan, Surface phonon polariton of wurtzite GaN thin film grown on -plane sapphire substrate, Solid State Commun 145 (11-12) (2008) 535–538.

[215] K. Torii, T. Koga, T. Sota, et al., An attenuated-total-reflection study on the surface phonon-polariton in GaN, J. Phys.: Condens. Matter 12 (2000) 7041–7044.

[216] Y. Wu, J. Ordonez-Miranda, S. Gluchko, et al., Enhanced thermal conduction by surface phonon-polaritons, Sci. Adv. 6 (2020) eabb4461.

[217] S.S. Ng, Z. Hassan, H. Abu Hassan, Experimental and theoretical studies of surface phonon polariton of AlN thin film, Appl. Phys. Lett. 90 (8) (2007) 081902.

[218] A.J. Huber, B. Deutsch, L. Novotny, et al., Focusing of surface phonon polaritons, Appl. Phys. Lett. 92 (20) (2008) 203104.

[219] D.Z.A. Chen, G. Chen, Heat Flow in Thin Films Via Surface Phonon-Polaritons. Front, Heat Mass Transfer 1 (2) (2010) 023005.

[220] K. Feng, W. Streyer, S.M. Islam, et al., Localized surface phonon polariton resonances in polar gallium nitride, Appl. Phys. Lett. 107 (8) (2015) 081108.

[221] Y. Guo, S. Tachikawa, S. Volz, et al., Quantum of thermal conductance of nanofilms due to surface-phonon polaritons, Phys. Rev. B 104 (20) (2021) L201407.

[222] S.C. Lee, S.S. Ng, P.K. Ooi, et al., Surface and interface phonon polariton characteristics of wurtzite ZnO/GaN heterostructure, Appl. Phys. Lett. 98 (24) (2011) 241909.

[223] S.S. Ng, T.L. Yoon, Z. Hassan, et al., Surface and interface phonon polaritons of wurtzite GaN thin film grown on 6H-SiC substrate, Appl. Phys. Lett. 94 (24) (2009) 241912.

[224] L. Zhang, Surface phonon and confined phonon polaritons in wurtzite nitride thin-film structures, Surf. Rev. Lett. 15 (2008) 493–501.

[225] J. Ordonez-Miranda, S. Volz, M. Nomura, Surface Phonon-Polariton Heat Capacity of Polar Nanofilms, Phys. Rev. Appl. 15 (5) (2021) 054068.

[226] D.L. Mills, Attenuation of surface polaritons by surface roughness, Phys. Rev. B 12 (10) (1975) 4036–4046.

[227] D.-Z.A. Chen, A. Narayanaswamy, G. Chen, Surface phonon-polariton mediated thermal conductivity enhancement of amorphous thin films, Phys. Rev. B 72 (15) (2005) 155435.

[228] S.S. Ng, Z. Hassan, H.A. Hassan, Composition Dependence of Surface Phonon Polariton Mode in Wurtzite InxGa$_{1-}$$x$N $(0{\leqslant}x{\leqslant}1)$ Ternary Alloy, Chin. Phys. Lett. 25 (2008) 4378–4380.

[229] S.S. Ng, Z. Hassan, H. Abu Hassan, Surface phonon polariton mode of wurtzite structure AlxGa$_{1-}$$x$N $(0{\leqslant}x{\leqslant}1)$ thin films, Appl. Phys. Lett. 91 (8) (2007) 081909.

[230] L. Zhang, J.J. Shi, Surface phonon polariton modes of wurtzite structure AlxGa1-xN thin film, Phys. Status Solidi B 246 (1) (2009) 164–169.

[231] P.K. Ooi, S.C. Lee, S.S. Ng, et al., Theoretical studies of surface phonon polariton in wurtzite AlInN ternary alloy, Thin Solid Films 519 (16) (2011) 5481–5485.

[232] Y. Liu, Y. Xu, S.C. Zhang, et al., Model for topological phononics and phonon diode, Phys. Rev. B 96 (6) (2017) 064106.

[233] Y. Liu, Y. Xu, W. Duan, Three-dimensional topological states of phonons with tunable Pseudospin physics, Research (Wash D C) 2019 (2019) 5173580.

[234] T. Zhang, Z. Song, A. Alexandradinata, et al., Double-Weyl phonons in transition-metal monosilicides, Phys. Rev. Lett. 120 (1) (2018) 016401.

[235] P.F. Liu, J. Li, X.H. Tu, et al., First-principles prediction of ideal type-II Weyl phonons in wurtzite ZnSe, Phys. Rev. B 103 (9) (2021) 094306.

[236] J. Liu, W. Hou, E. Wang, et al., Ideal type-II Weyl phonons in wurtzite CuI, Phys. Rev. B 100 (8) (2019) 081204 (R).

[237] Q. Xie, J. Li, S. Ullah, et al., Phononic Weyl points and one-way topologically protected nontrivial phononic surface arc states in noncentrosymmetric WC–type materials, Phys. Rev. B 99 (17) (2019) 174306.

[238] Q.B. Liu, Y.T. Qian, H.H. Fu, et al., Symmetry-enforced Weyl phonons, npj Comput. Mater. 6 (1) (2020) 95.

[239] R. Wang, B.W. Xia, Z.J. Chen, et al., Symmetry-protected topological triangular Weyl complex, Phys. Rev. Lett. 124 (10) (2020) 105303.

[240] F. Li, X.Q. Huang, J.Y. Lu, et al., Weyl points and Fermi arcs in a chiral phononic crystal, Nat. Phys. 14 (1) (2017) 30–34.

[241] D.S. Tang, B.Y. Cao, Topological effects of phonons in GaN and AlGaN: A potential perspective for tuning phonon transport, J. Appl. Phys. 129 (8) (2021) 085102.

[242] J.X. Li, L. Wang, J.X. Liu, et al., Topological phonons in graphene, Phys. Rev. B 101 (8) (2020) 081403 (R).

[243] L. Zhang, Q. Niu, Chiral phonons at high-symmetry points in monolayer hexagonal lattices, Phys. Rev. Lett. 115 (11) (2015) 115502.

[244] H. Chen, W. Wu, J. Zhu, et al., Propagating Chiral Phonons in Three-Dimensional Materials, Nano Lett 21 (7) (2021) 3060–3065.

[245] X. Xu, W. Zhang, J. Wang, et al., Topological chiral phonons in center-stacked bilayer triangle lattices, J. Phys.: Condens. Matter 30 (22) (2018) 225401.

[246] J.W. Jiang, B.S. Wang, H.S. Park, Topologically protected interface phonons in two-dimensional nanomaterials: hexagonal boron nitride and silicon carbide, Nanoscale 10 (29) (2018) 13913–13923.

[247] Y. Yang, J. Lu, M. Yan, et al., Hybrid-order topological insulators in a phononic crystal, Phys. Rev. Lett. 126 (15) (2021) 156801.

[248] C. Xu, Z.-G. Chen, G. Zhang, et al., Multi-dimensional wave steering with higher-order topological phononic crystal, Sci. Bull. 66 (17) (2021) 1740–1745.

[249] L. Luo, H.X. Wang, Z.K. Lin, et al., Observation of a phononic higher-order Weyl semimetal, Nat. Mater. 20 (6) (2021) 794–799.

[250] X. Ni, M. Weiner, A. Alu, et al., Observation of higher-order topological acoustic states protected by generalized chiral symmetry, Nat. Mater. 18 (2) (2019) 113–120.

[251] Y. Long, J. Ren, H. Chen, Unsupervised manifold clustering of topological phononics, Phys. Rev. Lett. 124 (18) (2020) 185501.

[252] L. Ye, C. Qiu, M. Xiao, et al., Topological dislocation modes in three-dimensional acoustic topological insulators, Nat. Commun. 13 (2022) 508.

[253] J.R.M. Silva, M.S. Vasconcelos, D. Anselmo, et al., Phononic topological states in 1D quasicrystals, J. Phys.: Condens. Matter 31 (50) (2019) 505405.

[254] L. Zhang, J. Ren, J.S. Wang, et al., The phonon Hall effect: theory and application, J Phys.: Condens. Matter 23 (30) (2011) 305402.

[255] Z.J. Chen, R. Wang, B.W. Xia, et al., Three-Dimensional Dirac Phonons with Inversion Symmetry, Phys. Rev. Lett. 126 (18) (2021) 185301.

[256] J. Li, J. Liu, S.A. Baronett, et al., Computation and data driven discovery of topological phononic materials, Nat. Commun. 12 (1) (2021) 1204.

[257] Y. Liu, N. Zou, S. Zhao, et al., Ubiquitous Topological States of Phonons in Solids: Silicon as a Model Material, Nano Lett 22 (5) (2022) 2120–2126.

[258] Y.Z. Liu, X.B. Chen, Y. Xu, Topological phononics: from fundamental models to real materials, Adv. Funct. Mater. 30 (8) (2019) 1904784.

[259] L. Zhang, Q. Niu, Angular momentum of phonons and the Einstein–de Haas effect, Phys. Rev. Lett. 112 (8) (2014) 085503.

[260] Y. Chen, X. Liu, G. Hu, Topological phase transition in mechanical honeycomb lattice, J. Mech. Phys. Solids 122 (2019) 54–68.

[261] X. Li, C. Xia, Y. Pan, et al., Topological chiral phonons along the line defect of intralayer heterojunctions, Phys. Rev. B 104 (5) (2021) 054103.

[262] H. A. Yang, H. Y. Wei and B. Y. Cao, Symmetry-enforced planar nodal chain phonons in nonsymmorphic materials. arXiv 2209 (2022) 02363.

[263] C. He, X. Ni, H. Ge, et al., Acoustic topological insulator and robust one-way sound transport, Nat. Phys. 12 (12) (2016) 1124–1129.

[264] X.L. Qi, S.C. Zhang, Topological insulators and superconductors, Rev. Mod. Phys. 83 (4) (2011) 1057–1110.

[265] M.Z. Hasan, C.L. Kane, Colloquium: Topological insulators, Rev. Mod. Phys. 82 (4) (2010) 3045–3067.

[266] X.L. Qi, S.C. Zhang, The quantum spin Hall effect and topological insulators, Phys. Today 63 (1) (2010) 33–38.

[267] P. Wang, L. Lu, K. Bertoldi, Topological phononic crystals with one-way elastic edge waves, Phys. Rev. Lett. 115 (10) (2015) 104302.

[268] Z. Wang, Y.D. Chong, J.D. Joannopoulos, et al., Reflection-free one-way edge modes in a gyromagnetic photonic crystal, Phys. Rev. Lett. 100 (1) (2008) 013905.

[269] Y. Ran, Y. Zhang, A. Vishwanath, One-dimensional topologically protected modes in topological insulators with lattice dislocations, Nat. Phys. 5 (4) (2009) 298–303.

[270] S. S. Yamada, T. Li, M. Lin, et al., Bound states at partial dislocation defects in multipole higher-order topological insulators. arXiv (2021) 2105.01050.

[271] Y. Liu, S. Leung, F.F. Li, et al., Bulk-disclination correspondence in topological crystalline insulators, Nature 589 (7842) (2021) 381–385.

[272] Q. Wang, Y. Ge, H.X. Sun, et al., Vortex states in an acoustic Weyl crystal with a topological lattice defect, Nat. Commun. 12 (1) (2021) 3654.

[273] Q. Wang, H. Xue, B. Zhang, et al., Observation of Protected Photonic Edge States Induced by Real-Space Topological Lattice Defects, Phys. Rev. Lett. 124 (24) (2020) 243602.

[274] C.W. Peterson, T. Li, W. Jiang, et al., Trapped fractional charges at bulk defects in topological insulators, Nature 589 (7842) (2021) 376–380.

[275] N.P. Mitchell, L.M. Nash, D. Hexner, et al., Amorphous topological insulators constructed from random point sets, Nat. Phys. 14 (4) (2018) 380–385.

[276] A. Agarwala, V. Juričić, B. Roy, Higher-order topological insulators in amorphous solids, Phys. Rev. Res. 2 (1) (2020) 012067 (R).

[277] Y.B. Yang, T. Qin, D.L. Deng, et al., Topological Amorphous Metals, Phys. Rev. Lett. 123 (7) (2019) 076401.

[278] A. Agarwala, V.B. Shenoy, Topological insulators in amorphous systems, Phys. Rev. Lett. 118 (23) (2017) 236402.